

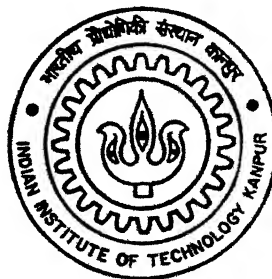
412060

MICROSTRUCTURAL EVOLUTION OF FERRITIC (434L) AND AUSTENITIC (316L) STAINLESS STEEL WITH BORIDE AND COPPER ADDITIVES

By

Anirban Chakraborty

H
E/2003/M
348 m.



DEPARTMENT OF MATERIALS AND METALLURGICAL ENGINEERING

Indian Institute of Technology Kanpur

JUNE, 2003

MICROSTRUCTURAL EVOLUTION OF FERRITIC (434L) AND AUSTENITIC (316L) STAINLESS STEEL WITH BORIDE AND COPPER ADDITIVES

A Thesis Submitted

In Partial Fulfillment of the Requirements

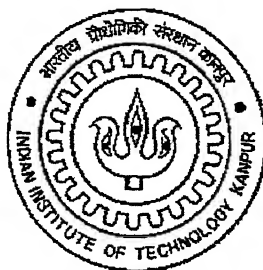
For the degree of

Master of Technology

by

ANIRBAN CHAKRABORTY

(Roll No. Y120603)



to the

**DEPARTMENT OF MATERIALS AND METALLURGICAL ENGINEERING
INDIAN INSTITUTE OF TECHNOLOGY KANPUR**

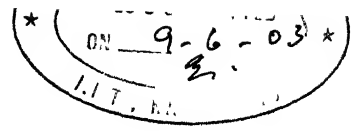
JUNE, 2003

22 SEP 2003 / mme

सुखोत्तम काशीनाथ केलकर पुस्तकालय
भारतीय प्रौद्योगिकी संस्थान काठमाण्डू
अवधि क्र० A.....145000



A145000



CERTIFICATE

This is to certify that the work contained in the thesis entitled **“Microstructural Evolution of Ferritic (434L) and Austenitic (316L) Stainless Steels with Boride and Copper Additives”** by Anirban Chakraborty (Roll No. Y120603) has been carried out under our supervision and to the best of our knowledge this work has not been submitted elsewhere for a degree.

Dr. R. K. Ray

Professor

Department of Materials and

Metallurgical Engineering

Indian Institute of Technology,

Kanpur

Dr. Anish Upadhyaya

Assistant Professor

Department of Materials and

Metallurgical Engineering

Indian Institute of Technology,

Kanpur

***Dedicated to my
Parents, Brother, and Sister-in-law***

Acknowledgements

I would like to express my sincere gratitude to my teachers and thesis supervisors Dr A. Upadhyaya and Dr R K. Ray for their able guidance and support throughout my post graduate study at Indian Institute of Technology, Kanpur. Their leaderships immeasurably helped me to early identification of an industrially significant area of research.

I want to specially thank Dr. Mungole, Mr. V. Kumar, Mr S.C. Soni, and Mr. U. S. Singh for their technical assistance and guidance during the present reasearch work.

My time in this institute was enriched by my lab mates Chiradeep, Pampa, Kausik, Rout, Pinakida, and Rajibda. I would also like to thank my other friends who made my stay at IIT Kanpur a pleasant one.

At this time I would like to express my deepest sense of gratitude to my beloved parents, brother and sister-in-law for their immense patience, moral support, encouragement, and inspiration during this research programme.

Last but not the least; I would like to thank MME department staffs and ACMS staffs, who helped me in many occasions.

Anirban Chakraborty

CONTENTS

Abstract	v
List of Figures	vi
List of Tables	xi
Chapter 1 Introduction	1
 Chapter 2 Background	
2.1 Stainless Steel	4
2.1.1 Types of Stainless Steel	5
2.1.2 Selection of Stainless Steel	10
2.2 P/M Stainless Steel	12
2.3 Application of P/M Stainless Steel	13
2.4 P/M Processing	14
2.5 Sintering	23
2.5.1 Solid State Sintering	25
2.5.1.1 Limitations of Solid State Sintering	26
2.5.2 Liquid Phase Sintering	30
2.5.2.1 Transient Liquid Phase Sintering	31
2.5.2.2 Supersolidus Liquid Phase Sintering (SLPS)	35
2.5.2.2.1 Previous Research on SLPS	38
2.5.2.2.2 Parameters Affecting SLPS	39
2.5.2.2.3 Limitations of SLPS	39
2.6 P/M Processing of Stainless Steel using Boride and Copper Addition	40
2.6.1 Densification Mechanisms	40
2.6.2 Effect of Sintering Atmosphere	45
2.6.3 Effect of Additives on Mechanical Properties	47
2.7 A Review of P/M Stainless Steel	47
 Chapter 3 Scope of the Present Work	52

Chapter 4 Experimental Procedure

4.1 Raw Materials	54
4.1.1 Stainless Steel Powders	54
4.1.1.1 Ferritic Stainless Steel Powder (434L)	54
4.1.1.2 Austenitic Stainless Steel Powder (316L)	55
4.1.2 Copper Powder (Cu)	56
4.1.3 Iron Boride Powder (FeB)	56
4.1.4 Nickel Boride Powder (NiB)	56
4.1.5 Yttria Alumina Garnet Powder (YAG)	57
4.2 Powder Characterization	57
4.2.1 Particle Size and Size Distribution	57
4.2.2 Particle Shape	61
4.3 Premix Preparation	63
4.4 Compaction	63
4.5 Sintering	67
4.6 Densification Behaviour	72
4.6.1 Density and Densification Parameter	72
4.6.2 Axial and Radial Shrinkage	73
4.7 X-Ray Diffraction Analysis	73
4.8 Microstructural Studies	74
4.8.1 Optical Microscopy	74
4.8.2 Scanning Electron Microscopy	75
4.9 Study of Mechanical Properties	75
4.9.1 Hardness	75
4.9.1.1 Vickers Bulk hardness	75
4.9.1.2 Vickers Microhardness	75
4.9.2 Study of Tensile Properties	76

Chapter 5 Experimental Results

5.1 Densification Behaviour	79
5.1.1 Density and Densification Parameter	79
5.1.2 Axial and Radial Shrinkage	81
5.2 Optical Microscopy	86
5.3 Scanning Electron Microscopy	102

5.4 Study of Mechanical Properties	103
5.4.1 Hardness	103
5.4.1.1 Bulk hardness	103
5.4.1.2 Microhardness	104
5.4.2 Tensile Properties	105
5.5 Phase Identification by X-ray Diffraction	108
Chapter 6 Discussion	
6.1 Effect of Sintering Temperature and Additives on Densification Behaviour	115
6.1.1 Effect of Sintering Temperature	115
6.1.2 Effect of Additives	116
6.1.3 Synergistic Effects of Sintering Temperature and Additives	118
6.2 Evolution of Microstructure	120
6.3 Evolution of Mechanical Properties	125
6.3.1 Bulk hardness	125
6.3.2 Microhardness	125
6.3.3 Tensile Properties	126
Chapter 7 Conclusions	128
References	129
Appendix I Experimental Data for the 434L Samples with Additives Sintered at 1250°C	138
Appendix II Experimental Data for the 434L Samples with Additives Sintered at 1400°C	140
Appendix III Experimental Data for the 316L Samples with Additives Sintered at 1250°C	142
Appendix IV Experimental Data for the 316L Samples with Additives Sintered at 1400°C	144
Appendix V Axial and radial dimensions of the 434L samples with additives sintered at 1250°C	146

Appendix VI Axial and radial dimensions of the 434L samples with additives sintered at 1400°C	147
Appendix VII Axial and radial dimensions of the 316L samples with additives sintered at 1250°C	148
Appendix VIII Axial and radial dimensions of the 316L samples with additives sintered at 1400°C	149
Appendix IX Bulk hardness (HV_2) values of the 434L samples with additives	150
Appendix X Bulk hardness (HV_2) values of the 316L samples with additives	151
Appendix XI Microhardness ($HV_{0.005}$) values of the 434L and 316L samples with additives	152

ABSTRACT

Ferrous based materials provide the largest class of P/M alloys and are of great industrial importance. Most P/M ferrous alloys are solid-state sintered and the final part contains up to 15% porosity. This restricts the use of such alloys in as-sintered condition and necessitates costly secondary operations. The present study investigates the use of novel supersolidus liquid phase sintering (SLPS) technique to achieve near full density in ferritic (434L) and austenitic (316L) stainless steel. As compared to solid-state sintering, SLPS results in higher density and thereby enhances mechanical properties as well. This study investigates the use of up to 2 wt. % of alloying additives, such as Cu and B (added as NiB and FeB) for enhancing densification during sintering. Addition of Ytria Alumina Garnet has been found to be beneficial in restricting grain growth and enhancing the mechanical properties.

LIST OF FIGURES

Chapter 2

2.1 Fe-Cr binary phase diagram [5].	6
2.2 Fe-Ni binary phase diagram [5]	6
2.3 Fe-Mo binary phase diagram [5].	7
2.4 Ternary phase diagram of stainless steel [7]	7
2.5 Compositional and property linkage in the stainless steel family [2].	11
2.6 Some typical P/M stainless steel products [12]	17
2.7 P/M parts market [12]	19
2.8 Densification during compaction by changes in particle arrangement and shape [13].	22
2.9 Map of sintering process and the subdivisions in terms of the key processing parameters [16].	27
2.10 Two sphere sintering model [17].	28
2.11 Possible sintering mechanisms at the neck area [13].	29
2.12 Schematic phase diagram showing different temperature of sintering.	29
2.13 Ideal phase diagram for liquid phase sintering [16].	32
2.14 A map of density versus liquid content with indications of the dominant regions [16]	32
2.15 The classic stages of liquid phase sintering involving mixed powders which form a liquid on heating [16].	33
2.16 Two binary phase diagrams showing possible conditions where transient liquid phase sintering can occur [16].	33
2.17 Schematic diagram of densification process during supersolidus liquid phase sintering [30].	37
2.18 Binary phase diagram of Fe-B [7].	42
2.19 Binary phase diagram of Ni-B [7].	46

Chapter 4

4.1 Chemical composition of the 434L powder.	54
4.2 Chemical composition of the 316L powder.	55
4.3 Histogram plot of the particle size analysis of 434L powder.	58

4.4 Histogram plot of the particle size analysis of 316L powder.	58
4.5 Histogram plot of the particle size analysis of Cu powder.	59
4.6 Histogram plot of the particle size analysis of FeB powder.	59
4.7 Histogram plot of the particle size analysis of NiB powder	60
4.8 Histogram plot of the particle size analysis of YAG powder.	60
4.9 SEM micrograph of 434L powder.	64
4.10 SEM micrograph of 316L powder.	64
4.11 SEM micrograph of Copper powder.	65
4.12 SEM micrograph of FeB powder.	65
4.13 SEM micrograph of NiB powder.	66
4.14 SEM micrograph of YAG powder.	66
4.15 Composition of investigated materials (434L with additives).	68
4.16 Composition of investigated materials (316L with additives).	70
4.17 Schematic diagram of sintering furnace.	78
4.18 A Standard powder metallurgical tensile sample.	78

Chapter 5

5.1 Variation of sintered density with sintering temperature for 434L samples with additives.	82
5.2 Variation of densification parameter with sintering temperature for 434L samples with additives	82
5.3 Variation of sintered density with sintering temperature for 316L samples with additives.	83
5.4 Variation of densification parameter with sintering temperature for 316L samples with additives.	83
5.5 Variation of axial vs. radial shrinkage of 434L samples with additives sintered at 1250°C temperature.	84
5.6 Variation of axial vs. radial shrinkage of 434L samples with additives sintered at 1400°C temperature.	84
5.7 Variation of axial vs. radial shrinkage of 316L samples with additives sintered at 1250°C temperature.	85
5.8 Variation of axial vs. radial shrinkage of 316L samples with additives sintered at 1400°C temperature.	85
5.9 Optical micrographs of pure 434L samples sintered at (a) 1250°C and (b)	

1400°C.	
5.10 Optical micrographs of 434L-2Cu sample sintered at 1250°C (a) lower and (b) higher magnification.	87
5.11 Optical micrographs of 434L-2Cu sample sintered at 1400°C (a) lower and (b) higher magnification.	87
5.12 Optical micrographs of 434L-0.9FeB sample sintered at 1250°C (a) lower and (b) higher magnification.	88
5.13 Optical micrographs of 434L-0.9FeB sample sintered at 1400°C (a) lower and (b) higher magnification.	88
5.14 Optical micrographs of 434L-2Cu-0.3NiB sample sintered at 1250°C (a) lower and (b) higher magnification.	89
5.15 Optical micrographs of 434L-2Cu-0.3NiB sample sintered at 1400°C (a) lower and (b) higher magnification.	89
5.16 Optical micrographs of 434L-2Cu-0.3FeB sample sintered at 1250°C (a) lower and (b) higher magnification.	90
5.17 Optical micrographs of 434L-2Cu-0.3FeB sample sintered at 1400°C (a) lower and (b) higher magnification.	90
5.18 Optical micrographs of 434L-2Cu-0.3FeB-1YAG sample sintered at 1400°C (a) lower and (b) higher magnification.	91
5.19 Optical micrographs of 434L-2Cu-0.3NiB-1YAG sample sintered at 1400°C (a) lower and (b) higher magnification.	91
5.20 Optical micrographs of pure 316L sample sintered at 1250°C (a) lower and (b) higher magnification.	92
5.21 Optical micrographs of pure 316L sample sintered at 1400°C (a) lower and (b) higher magnification.	92
5.22 Optical micrographs of 316L-2Cu sample sintered at 1250°C (a) lower and (b) higher magnification.	93
5.23 Optical micrographs of pure 316L-2Cu sample sintered at 1400°C (a) lower and (b) higher magnification.	93
5.24 Optical micrographs of 316L-0.3FeB sample sintered at 1250°C (a) lower and (b) higher magnification.	94
5.25 Optical micrographs of 316L-0.3NiB sample sintered at 1250°C (a) lower and (b) higher magnification.	94
5.26 Optical micrographs of 316L-0.3FeB sample sintered at 1400°C (a)	95

lower and (b) higher magnification.	95
5.27 Optical micrographs of 316L-0.3NiB sample sintered at 1400°C (a)	
lower and (b) higher magnification.	96
5.28 Optical micrographs of 316L-2Cu-0.3FeB samples sintered at (a) 1250°C	
and (b) 1400°C	96
5.29 Optical micrographs of 316L-2Cu-0.3NiB samples sintered at (a) 1250°C	
and (b) 1400°C.	97
5.30 Optical micrographs of 316L-0.3FeB-1YAG sample sintered at 1400°C	
(a) lower and (b) higher magnification.	97
5.31 Optical micrographs of 316L-0.3NiB-1YAG sample sintered at 1400°C	
(a) lower and (b) higher magnification.	98
5.32 SEM micrographs of pure 434L samples sintered at (a) 1250°C and (b)	
1400°C.	98
5.33 SEM micrographs of 434L-2Cu sample sintered at 1250°C (a) lower and	
(b) higher magnification.	99
5.34 SEM micrographs of 434L-2Cu sample sintered at 1400°C (a) lower and	
(b) higher magnification.	99
5.35 SEM micrographs of 434L-2Cu-0.3FeB sample sintered at 1250°C (a)	
lower and (b) higher magnification.	100
5.36 SEM micrographs of 434L-2Cu-0.3FeB sample sintered at 1400°C (a)	
lower and (b) higher magnification.	100
5.37 Variation of bulk hardness values as a function of sintering temperature	
for 434L samples with additives.	106
5.38 Variation of bulk hardness values as a function of sintering temperature	
for 316L samples with additives.	106
5.39 Variation of microhardness values as a function of sintering temperature	
for 434L samples with additives.	107
5.40 Variation of microhardness values as a function of sintering temperature	
for 316L samples with additives.	107
5.41 Stress-strain curve of 434L samples with additives.	110
5.42 SEM micrograph of fracture surface of 434L sample sintered at 1400°C.	110
5.43 SEM micrograph of fracture surface of 434L-2Cu-0.3FeB-1YAG sample	
sintered at 1400°C.	111

5.44 SEM micrograph of fracture surface of 434L-2Cu-0.3NiB-1YAG sample sintered at 1400°C.	111
5.45 Stress-strain curve of 316L samples with additives.	112
5.46 SEM micrograph of fracture surface of pure 316L sample sintered at 1400°C.	112
5.47 SEM micrograph of fracture surface of 316L-0.3FeB-1YAG sample sintered at 1400°C.	113
5.48 SEM micrograph of fracture surface of 316L-0.3NiB-1YAG sample sintered at 1400°C.	113
5.49 XRD plots of 434L samples with additives sintered at 1400°C	114
5.50 XRD plots of 316L samples with additives sintered at 1400°C.	114

Chapter 6

6.1 Optical micrographs of 434L-10Cu-0.3FeB sample sintered at 1400°C.	123
6.2 Optical micrograph showing the transformation of intergranular pores to intragranular type.	123

LIST OF TABLES

Chapter 2

2.1 Compositions of standard powder metallurgy stainless steels [1]	15
2.2 Characteristics of various grades of P/M stainless steel [1]	16
2.3 Application of sintered stainless steel [1]	20
2.4 Production of ferrous metal powders [14]	22

Chapter 4

4.1 Chemical composition of YAG powder.	62
4.2 Characteristics of the as received powders	62
4.3 Theoretical densities of investigated materials (434L and with additives).	69
4.4 Theoretical densities of investigated materials (316L and with additives).	71
4.5 Etchants for Ferritic Stainless Steel.	77
4.6 Etchants for Austenitic Stainless Steel.	77

Chapter 5

5.1 Tensile properties of selected samples	109
--	-----

Chapter 1

INTRODUCTION

Of all engineered materials, steel is the most widely used, every year more than 750 million tons of steels are consumed worldwide on wrought basis [1]. Among the all steels, stainless steels are most important due to its excellent corrosion resistance along with other mechanical properties. Stainless steels contain 11 to 30 % Chromium. They achieve their stainless characteristics through the formation of an invisible but adherent and continuous chromium oxide surface layer. In addition, to chromium some other alloying elements such as nickel, molybdenum, nitrogen, and sulfur are also added to improve specific characteristics such as re-passivation, pitting resistance and mechanical properties [2]. Depending upon the percentage and type of alloying addition, stainless steel is classified into five major categories namely, ferritic, austenitic, martensitic, duplex (ferrite and austenite) and precipitation-hardening stainless steels. Stainless steels find a number of applications such as automotive, chemical processing, medical instruments, aerospace, recreational fields, etc.

Despite its applications in various fields, processing of wrought stainless steel suffers from several limitations. Wrought stainless steel is normally processed by casting and requires machining to achieve the desired dimensional precision in the final products. Hence, there is a continued thrust for finding a newer method for processing stainless steel to obtain near net shaped products. The powder metallurgy (P/M) route is one of the better processing techniques to obtain near net shaped products for the applications. Powder metallurgical stainless steels are a relatively small, but rapidly growing, segment of P/M market. The P/M stainless steel, like its

wrought counterpart derives its corrosion resistance from the protective chromium oxide layer. However, the P/M stainless steel microstructure usually contains inherent pores. Depending on their dimensions, these pores/crevices act as initiation sites for breakdown of the passive layer due to accumulation of corrosion products within. Passivity enhancing elements like nickel, molybdenum or more of chromium is added in order to increase the corrosion resistance of P/M stainless steel. Nowadays, P/M Stainless steels with improved corrosion properties are gaining wide popularity. However, compared to the wrought stainless steel their applications are limited due to their poor density, corrosion resistance and mechanical properties.

Most P/M stainless steels are solid-state sintered and the final part contains up to 15% porosity. This is detrimental to both the mechanical properties and corrosion resistance. The as sintered compacts therefore require post sintering costly secondary operation, such as hot pressing, repress and re-sintering, and forging which further increases cost. Significant cost savings, both in processing and equipment, are possible by increasing the sintering temperature to supersolidus region. In this case sintering is carried out between solidus and liquidus temperature. Another approach is use of additives which act as sintering aids to increase the density of final sintered products. In addition, some of the sintering additives play a significant role in determining final mechanical and corrosion properties [3].

The present work has been undertaken to improve the properties of P/M 316L (austenite) and 434L (ferrite) stainless steel by sintering at solid state and at supersolidus region along with additives such as copper, boron (added in the form of FeB and NiB) and yttria alumina garnet.

In this thesis, Chapter 2 provides a brief introduction about the different types of stainless steel, their application, different types of sintering that are adopted in the

present work and also includes the effect of different sintering additives on mechanical properties. Chapter 3 represents the scope of the present on the basis of recent work done in P/M stainless steel. Chapter 4 describes the experimental procedures that are used in the present work. It also includes characterization of powder, premix preparation, compaction, sintering, metallographic and procedure of determination of mechanical properties. The experimental results are described in the Chapter 5. Chapter 6 and 7 consist of discussion and conclusion parts respectively.

Chapter 2

BACKGROUND

2.1 Stainless Steel

Stainless steels are as iron based alloys containing approximately 11% to 30% chromium. Steel becomes stainless due to the formation of a thin, adherent and invisible layer of chromium oxide (Cr_2O_3), which is formed on the surface of the steel in the presence of oxygen. This oxide layer is permanent as it heals itself in the presence of oxygen. The carbon content in stainless steel is usually less than 0.03% to over 1.0% in certain grades. Other elements that are added to improve the characteristics include nickel, molybdenum, copper, titanium, aluminum, silicon, niobium, nitrogen, sulfur, and selenium. Nickel and nitrogen are used as austenite stabilizers, to achieve a balance of ferrite plus austenite [4]. Molybdenum strengthens the passive film and improves pitting resistance. Copper and aluminum are added to lower the rate of corrosion. Titanium and niobium are added to reduce the susceptibility of the alloy to intergranular corrosion.

The phase diagrams of Fe-Cr, Fe-Ni and Fe-Mo are shown in Figures 2.1 to 2.3 [5]. In Figure 2.1, the Fe-Cr phase diagram shows the formation of two loops, namely the γ -loop and α -loop. Since Cr has a bcc structure it acts as a ferrite stabilizer and extends the α -phase, while suppressing the γ -phase, resulting in γ -loop. This divides the Fe-Cr phase diagram into fcc and bcc regions. When Cr is less than 12-13%, an austenite to ferrite transformation occurs on cooling within the loop. But when the Cr content is greater than 13% no transformation occurs [6]. The Fe-Cr phase diagram at low temperatures is not a complete range of solid solution. There is

an intermediate phase formed at 821°C called σ -phase. This phase has a tetragonal structure and is hard and brittle. Presence of this phase will lead to embrittlement of the alloy [6]. Nickel is added to iron to stabilize the austenitic phase, since it has the same fcc structure. The phase diagram of Fe-Ni in Figure 2.2 shows that the γ -loop is formed at less than 5% nickel. Molybdenum is added to increase the pitting resistance of stainless steel. Since it is added in very less amount it does not significantly affect the formation of γ -loop. The Fe-Mo phase diagram is shown in Figure 2.3. The ternary phase diagram of stainless steel is shown in Figure 2.4, which shows the critical composition for stainless steel.

2.1.1 Types of Stainless Steel

According to alloying elements the various types of stainless steels grades are shown in Figure 2.5 [8]. Though there are many grades of stainless steel available in the market, stainless steel is commonly divided into five groups: ferritic, austenitic, martensitic, duplex and precipitation-hardened stainless steel.

Ferritic stainless steels

Ferritic stainless steels possess body centered cubic (bcc) structure. It has chromium content varying between 11 to 30% and ferromagnetic in nature. They have good ductility and formability, but high-temperature mechanical properties are relatively inferior to the austenitic stainless steels. Toughness is limited at low temperatures and in heavy sections. Their high temperature strength is poor when compared to austenitic grades. Their main advantages are their resistance to chloride, stress corrosion-cracking, atmospheric corrosion and oxidation at a relatively low cost. Sulfur or selenium may be added to some grades to improve machinability. This alloy can only be hardened by cold working. Categories of ferritic stainless steels are

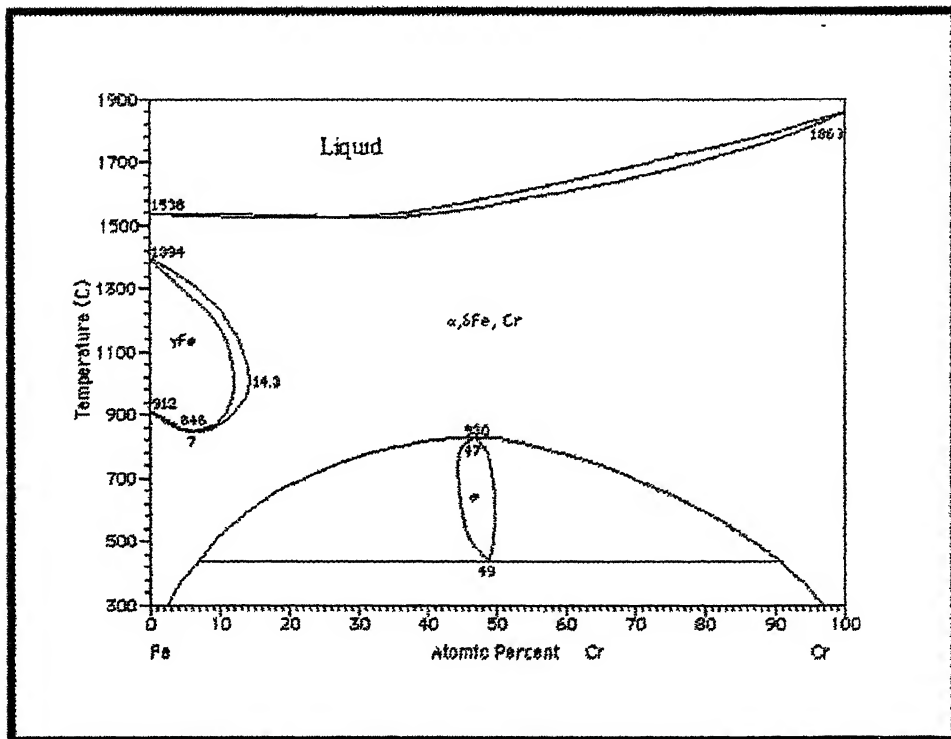


Figure 2.1 Fe-Cr binary phase diagram [5].

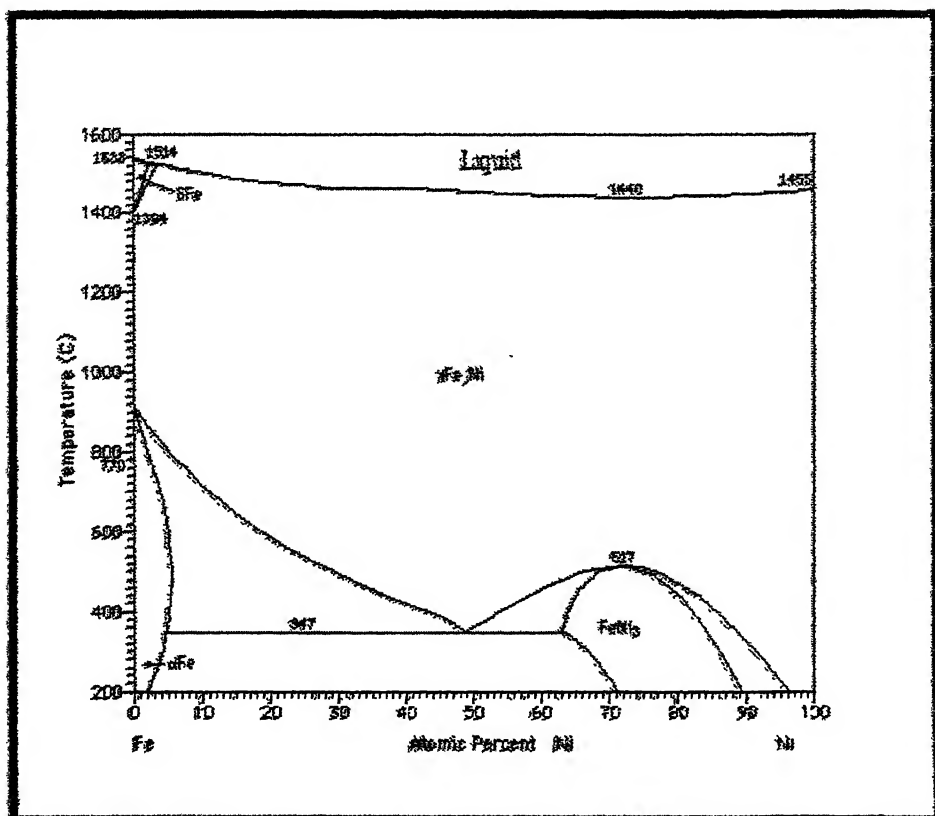


Figure 2.2 Fe-Ni binary phase diagram [5].

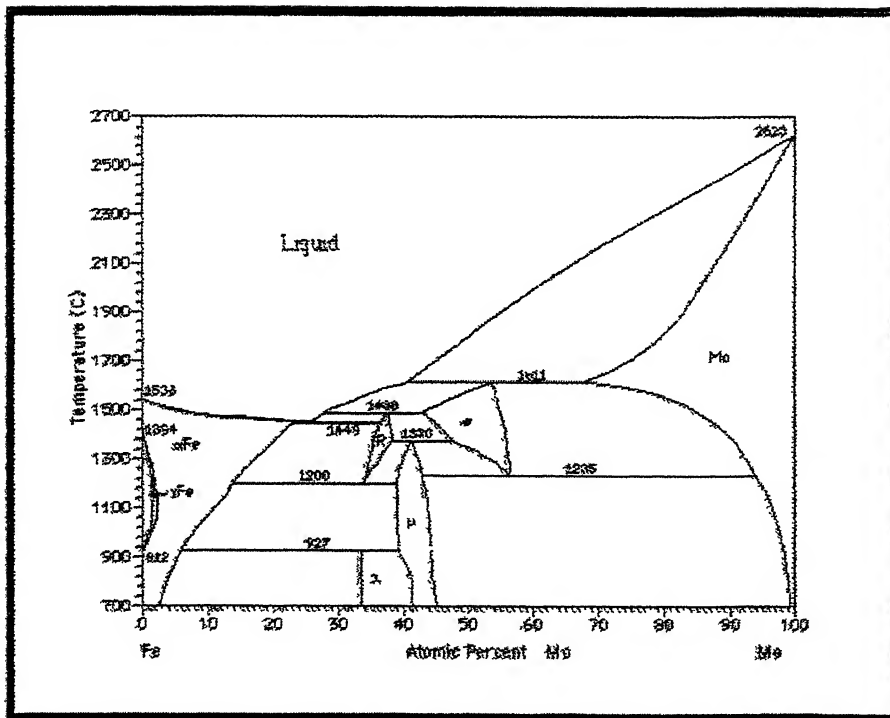


Figure 2.3 Fe-Mo binary phase diagram [5].

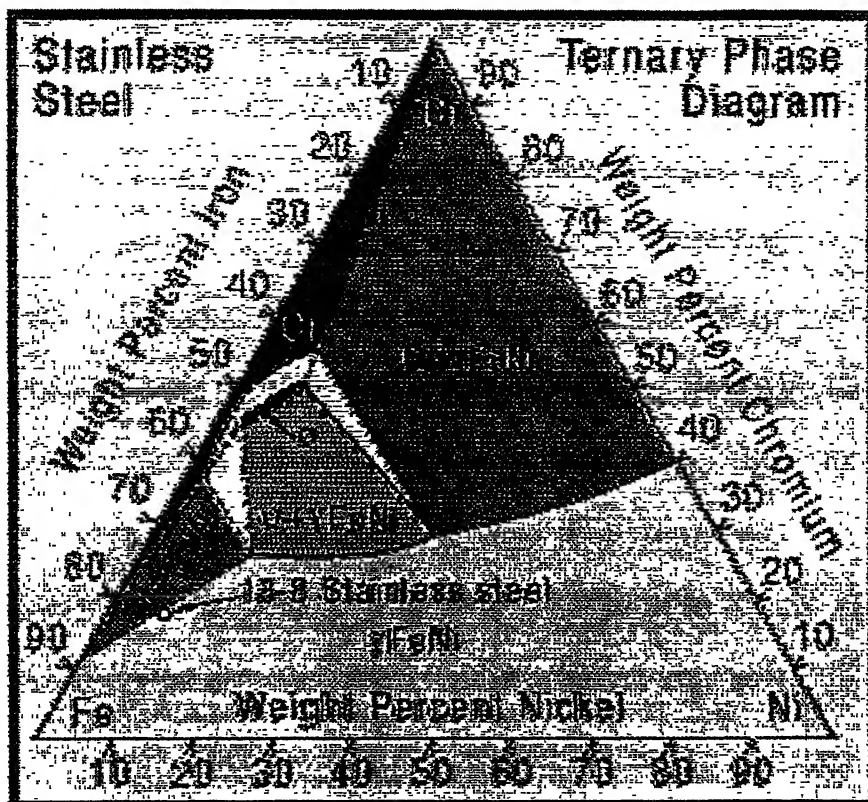


Figure 2.4 Ternary phase diagram of stainless steel [7].

405 (low Cr, added Al), 409 (lowest Cr), 434 (contains Mo), 436 (contains Nb), 442, and 446. They are used for decorative trim, sinks, and automotive applications, particularly exhaust systems, household utensils [9]

Austenitic stainless steels

Austenitic stainless steels are noted for high toughness, strength, ductility and formability. This constitutes the largest stainless steel family in terms of number of alloys and usage. Austenitic stainless steels have an austenitic; face centered cubic (fcc) crystal structure. Austenite is formed through the generous use of austenitizing elements such as nickel, manganese, and nitrogen. Austenitic stainless steels are effectively nonmagnetic in the annealed condition. They cannot be hardened by heat treatment, but can be hardened significantly by cold-working. Some ferromagnetism may be noticed due to cold working or welding. They typically have reasonable cryogenic and high temperature strength properties. Chromium content typically is in the range of 16 to 26%; nickel content is commonly less than 35%, and manganese up to 15%. There are two basic categories of austenitic stainless steels, the 3xx series having chromium-nickel alloys such as 304 (18% Cr-8% Ni), 316 (16-18% Cr, 11-14% Ni, min. 2% Mo), 317 (min. 3% Mo), 317L (max. 0.030% C, max. 0.75% Si), 317LM (min. 4% Mo), 317LMN (min. 0.15% N), 321 (contains Ti), 347 (contains Ta/Columbium) and the 2xx alloys containing manganese-nitrogen alloys such as 201, 202, and 241. The alloys having nitrogen will have higher strength when compared to the other alloys. Molybdenum, copper, silicon, aluminum, titanium and niobium may be added to improve specific properties like pitting resistance or oxidation resistance. They are used for chemical processing equipment, for food, dairy, and beverage industries, for heat exchangers, automobile industries, etc [10].

Martensitic stainless steels

Martensitic stainless steels are essentially alloys of chromium and carbon that possess a martensitic crystal structure (body centered tetragonal) in the hardened condition. They are ferromagnetic, hardened by heat treatments, and are usually less resistant to corrosion than some other grades of stainless steel. Apparently this type of stainless steel is corrosion resistant only in relatively mild environments i.e., around 4-6 pH [6]. Chromium content usually does not exceed 18%, while carbon content may exceed 1.0 %. The chromium and carbon contents are adjusted to ensure a martensitic structure after hardening. Excess carbides may be present to enhance wear resistance or as in the case of knife blades, to maintain cutting edges. Usually molybdenum and nickel are added to improve the corrosion resistance and toughness. Sulfur or selenium is added in some cases to improve machinability of martensitic stainless steels. Categories of martensitic stainless steels are 410, 410S (lower C %), 414 (2% Ni), 416(containing P, S), 420(higher C %), 431(higher Cr %), 440(higher C and Cr %). They are used for highly stressed parts needing the combination of strength and corrosion resistance such as fasteners, springs, cutlery, screw machine parts, valves and pumps, surgical instruments etc [10].

Duplex stainless steels

Duplex stainless steels are a mixture of bcc ferrite and fcc austenite crystal structures. It contains chromium-nickel-molybdenum alloys that are balanced to contain a mixture of austenitic and ferritic. The amounts of alloying elements are chromium 18 to 26%, nickel 4 to 7% and molybdenum 2 to 3% [11]. Most duplex stainless steels are intended to contain around equal amounts of ferrite and austenite phases in the annealed condition. The principal alloying elements in duplex stainless steels are chromium and nickel, but nitrogen, molybdenum, copper, silicon and

tungsten are added to control structural balance and thereby impart corrosion resistance characteristics. Duplex stainless steels generally have similar corrosion resistance to austenitic alloys except they typically have better stress corrosion cracking resistance. Duplex stainless steels also generally have greater tensile and yield strengths, but poorer toughness than austenitic stainless steels. Duplex stainless steels have better stress-corrosion cracking resistance than austenitic and improved toughness and ductility compared to ferritic stainless steels. The common grade of duplex stainless steel is 2205 [10]. Some of the applications of this kind of steels are Sea water applications heat exchangers, desalination plants, food pickling plants etc.

Precipitation hardened stainless steels

Precipitation hardened stainless steels are chromium-nickel alloys containing precipitation-hardening elements like copper, aluminum or titanium. The precipitation-hardened stainless steels are either martensitic or austenitic in annealed condition. The precipitation-hardened stainless steels have good ductility and toughness with moderate to good corrosion resistance. The well-known precipitation hardened stainless steel is S17400 grade, which is a chromium-nickel alloy containing copper as the aging element [2].

2.1.2 Selection of Stainless Steel

The selection of the type of stainless steel used depends upon various factors and the environment and type of application for which it is to be used. Martensitic stainless steels are used only in mild environments when compared to the other stainless steels, but it has higher strength and wear resistance. Austenitic stainless steels have good ductility, formability and corrosion resistance. Ferritic stainless

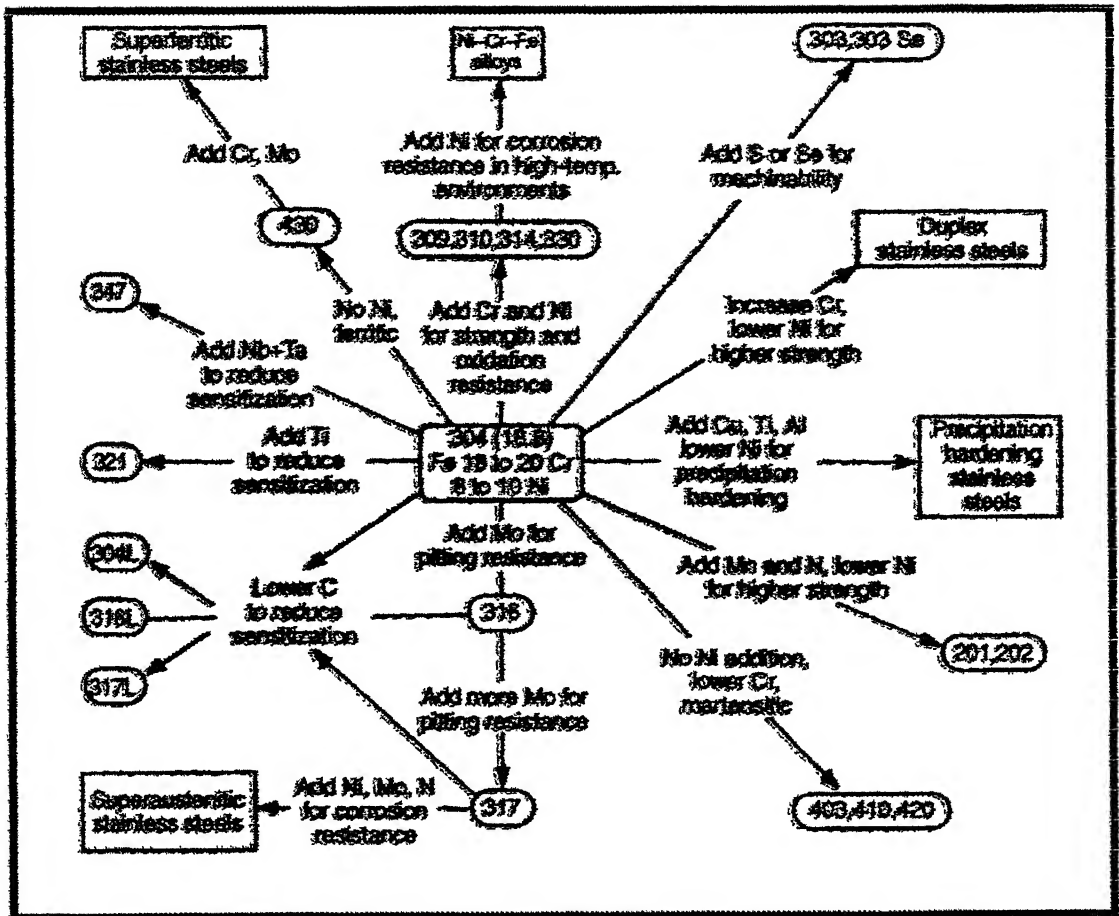


Figure 2.5 Compositional and property linkage in the stainless steel family [2].

steels have lesser corrosion resistance than austenitic stainless steels, but are preferred relatively because of their low cost and magnetic property. Precipitation hardened stainless steels have better mechanical properties than other types of stainless steels but their corrosion resistance is moderate. Duplex stainless steels have improved corrosion resistance than austenitic stainless steels and exhibit higher toughness and ductility than ferritic alloys. The general characteristics that are to be considered while selecting a type of stainless steel for an application are follows:

- Corrosion resistance
- Resistance to oxidation
- Strength and ductility at service temperatures
- Stability of the properties at various service conditions
- Physical property characteristics such as magnetic properties, thermal conductivity, electrical resistance
- Toughness, ductility and rigidity
- Resistance to abrasion
- Cryogenic strength
- Retention of cutting edge
- Ambient strength
- Elevated temperature strength

2.2 P/M Stainless Steel

There has been an enormous increase in the requirement of P/M stainless steel as it finds various applications. The growth rate of P/M stainless steel has increased from 4500 short tons (4100 metric ton) in 1996 to 8157 short tons (7432 metric ton) in 2000 [12]. Still this is only a small fraction when compared with the use of wrought

stainless steel and hence the powder producers are still working on the further development of P/M stainless steel. Optimum sintering parameters are also being developed, as stainless steel part producers continue to improve the control of their sintering operations. The various grades of stainless steel powders and their compositions are shown in the Table 2.1. Among the various grades most widely used P/M stainless steel parts are made up of 300 (austenitic) series and 400 (ferritic and martensitic) series. The 300 series are typically used in applications that require good corrosion resistance, while the ferritic grades are used in applications that require good magnetic properties and thermal conductivity. The characteristics of various grades of P/M stainless steel, their description and designation are shown in the Table 2.2. The selection of various grades for the applications is based on a number of considerations. Cost and corrosion resistance is the key property for majority of applications as in the case of wrought stainless steel. The other additional properties that are considered include magnetic characteristics, mechanical properties (both room temperature and elevated temperatures), machinability and hardenability.

2.3 Application of P/M Stainless Steel

Figure 2.6 shows some of the sintered stainless steel parts. Figure 2.7 shows the P/M parts market of stainless steel products in worldwide. From the figure it is clearly evident that automotive parts are the most significant application sector for P/M stainless steel. A substantial quantity is used for making the parts possessing control interconnected porosity for filtration, flanges, and sound attenuation. Also sintered stainless steel parts are used in hardware electrical system, household utensils, etc. sector. The various areas where the stainless steels are used are shown in Table 2.3.

2.4 P/M Processing

The P/M process has several success in ancient times (probably as early as 3000 BC) with application of coins and implements in ancient Egypt, gold-platinum powder compacts by the Incas, copper coins in Germany and platinum crucibles in the 1800s in England and Russia. The modern era is traced to Coolidge's experiments in the early 1900s and production of tungsten lamp filaments for the light bulbs, a process that still used today. By the 1930s several products emerged, including porous bronze bearings, tungsten radiation container, copper-graphite electrical contacts, cemented carbides for metal cutting, and the first steel mechanical components. Early P/M products were applied to mostly low stress, moderate complex components as an alternative to machining. By the 1960s interest in the net shaping attribute of P/M emerged. Aerospace uses grew with the development of full density fabrication techniques such as hot isostatic pressing. In the 1970s there emerged recognition of the rapid solidification rates possible in powder atomization, alloying the production of new compositions with noble properties [13].

Today, the largest activity is in associated with ferrous alloys, some iron, and many steels. Ferrous alloys constitute the dominant powders, and structural automotive components constitute the dominant applications. Attainment of the desire mechanical properties requires alloying to form high strength steels during sintering. The combination of low production cost and high sintered strength dominates the P/M selection criteria. Production technologies that allow high final densities include high temperature sintering, powder forging, powder rolling, injection molding, infiltration, hot isostatic compaction, pneumatic forging, and worm compaction [13].

Table 2.1 Compositions of standard powder metallurgy stainless steels [1].

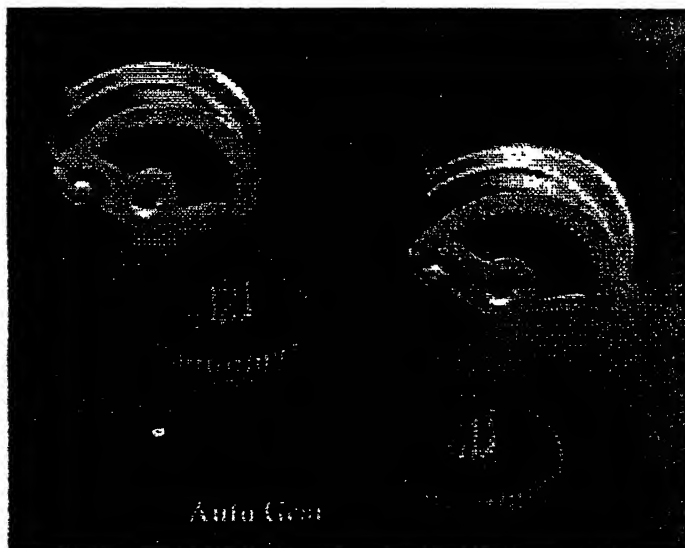
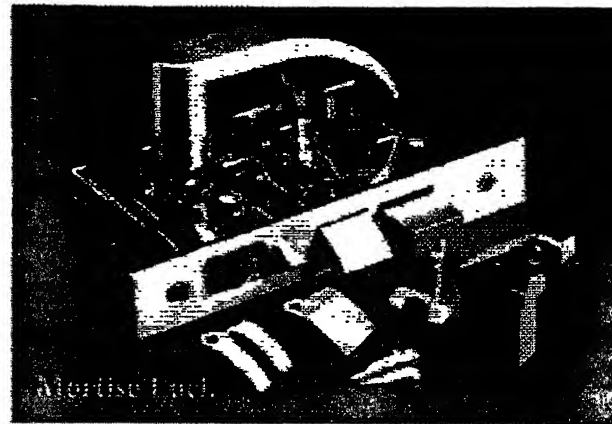
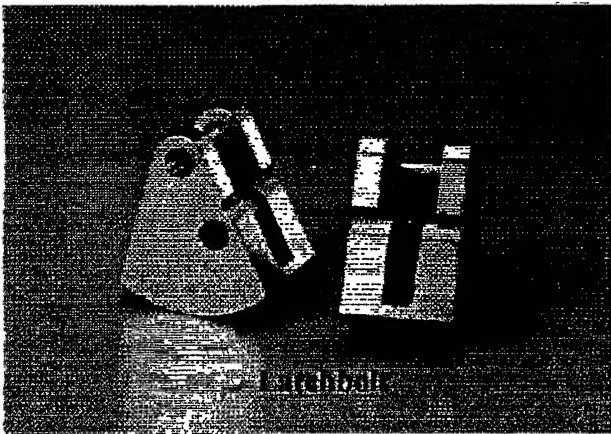
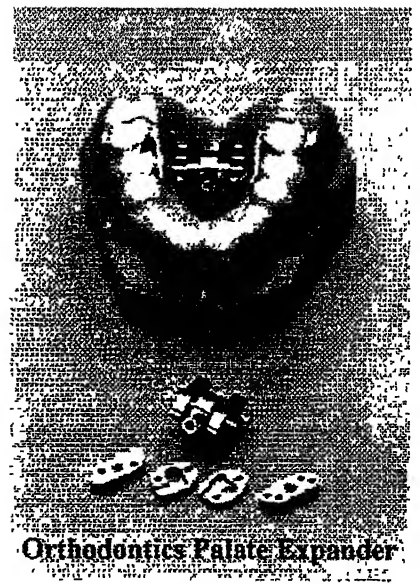
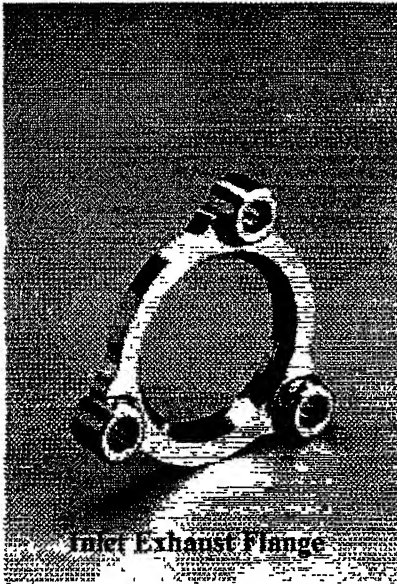
Material Designation	Chemical Composition (wt. %)										
	Cr	Ni	Mn	Si	S	C	P	Mo	N	Nb	Fe
<i>Austenitic Grades</i>											
303	17-19	8-13	0-2	0-1	0.15-0.3	0-0.15	0-0.2	-	0.2-0.6	-	Bal.
303L	17-19	8-13	0-2	0-1	0.15-0.3	0-0.03	0-0.2	-	0-0.03	-	Bal.
304	18-20	8-12	0-2	0-1	0-0.03	0-0.08	0-0.045	-	0.2-0.6	-	Bal.
304L	18-20	8-12	0-2	0-1	0-0.03	0-0.03	0-0.045	-	0-0.03	-	Bal.
316	16-18	10-14	0-2	0-1	0-0.03	0-0.08	0-0.045	2-3	0.2-0.6	-	Bal.
316L	16-18	10-14	0-2	0-1	0-0.03	0-0.03	0-0.045	2-3	0-0.03	-	Bal.
<i>Ferritic or Martensitic Grades</i>											
409L	10.5-11.75	-	0-1	0-1	0-0.03	0-0.03	0-0.04	-	0-0.03	8XC-0.8	Bal.
410	11.5-13.5	-	0-1	0-1	0-0.03	0-0.25	0-0.04	-	0.2-0.6	-	Bal.
410L	11.5-13.5	-	0-1	0-1	0-0.03	0-0.03	0-0.04	-	0-0.03	-	Bal.
430	16-18	-	0-1	0-1	0-0.03	0-0.08	0-0.04	-	0.2-0.6	-	Bal.
430L	16-18	-	0-1	0-1	0-0.03	0-0.03	0-0.04	-	0-0.03	-	Bal.
434	16-18	-	0-1	0-1	0-0.03	0-0.08	0-0.04	0.75-1.25	0.2-0.6	-	Bal.
434L	16-18	-	0-1	0-1	0-0.03	0-0.03	0-0.04	0.75-1.25	0-0.03	-	Bal.

Table 2.2 Characteristics of various grades of P/M stainless steel [1].

Designation	Description	Characteristics
303L	Free machining austenitic grade	Design for parts that require extensive secondary machining operations. It has high strength and hardness. These alloys have marginally corrosion resistance. Sulfur added for machinability.
304L	Basic austenitic grade	Most economical of austenitic grades. Used where material cost is large percentage of the total manufacturing cost. It has better corrosion resistance than 303L. Machinability is good.
316L	Standard austenitic grade	This alloy offers better corrosion resistance and machinability than 304L. With careful processing it can meet the corrosion resistance requirements of the more demanding applications.
321L	Premium austenitic grade	It is a higher Mo content austenitic grade processing excellent resistance to corrosion, especially to crevice corrosion.
439L	Weldable ferritic grade	A weldable grade of stainless steel containing Nb, which prevents sensitization. It is a magnetic alloy with good ductility and fair corrosion resistance.
410L	Standard ferritic/martensitic grade	This ferritic grade can be readily converted to a martensitic alloy by addition of small amount of carbon prior to processing, which will also make it responsive to heat treatment. In the ferritic form the alloy is ductile and machinable, whereas in the martensitic form it is hard with reduced ductility. In the martensitic form it is used in wear resistance applications. Both forms of alloys are magnetic. The martensitic form has the lowest corrosion resistance of all P/M stainless steel grades.
434L	Premium ferritic grade	Used for applications requiring some corrosion resistance but where economics is the main concern. These grades can not usually be converted in a martensitic alloy. Corrosion resistance and machinability are slightly better than 410L.

Table 2.2 Characteristics of various grades of P/M stainless steel [1]

Designation	Description	Characteristics
303L	Free machining austenitic grade	Design for parts that require extensive secondary machining operations. It has high strength and hardness. These alloys have marginally corrosion resistance. Sulfur added for machinability.
304L	Basic austenitic grade	Most economical of austenitic grades. Used where material cost is large percentage of the total manufacturing cost. It has better corrosion resistance than 303L. Machinability is good.
316L	Standard austenitic grade	<i>This alloy offers better corrosion resistance and machinability than 304L. With careful processing it can meet the corrosion resistance requirements of the more demanding applications.</i>
317L	Premium austenitic grade	It is a higher Mo content austenitic grade processing excellent resistance to corrosion, especially to crevice corrosion.
409L	Weldable ferritic grade	A weldable grade of stainless steel containing Nb, which prevents sensitization. It is a magnetic alloy with good ductility and fair corrosion resistance.
410L	Standard ferritic/martensitic grade	This ferritic grade can be readily converted to a martensitic alloy by addition of small amount of carbon prior to processing, which will also make it responsive to heat treatment. In the ferritic form the alloy is ductile and machinable, whereas in the martensitic form it is hard with reduced ductility. In the martensitic form it is used in wear resistance applications. Both forms of alloys are magnetic. The martensitic form has the lowest corrosion resistance of all P/M stainless steel grades.
430L/434L	Premium ferritic grade	Used for applications requiring some corrosion resistance but where economics is the main concern. These grades can not usually be converted in a martensitic alloy. Corrosion resistance and machinability are slightly better than 410L.



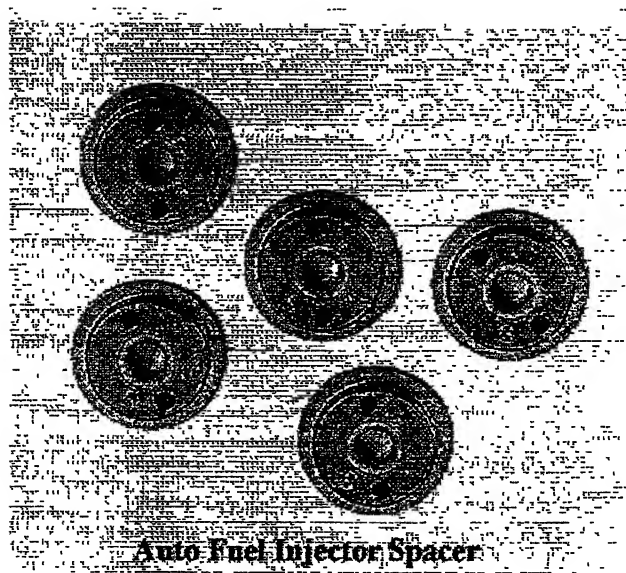
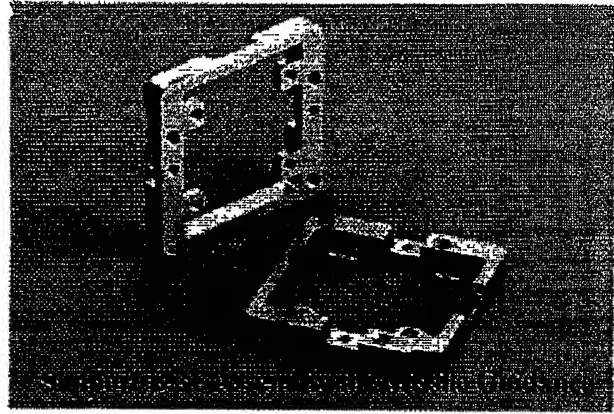
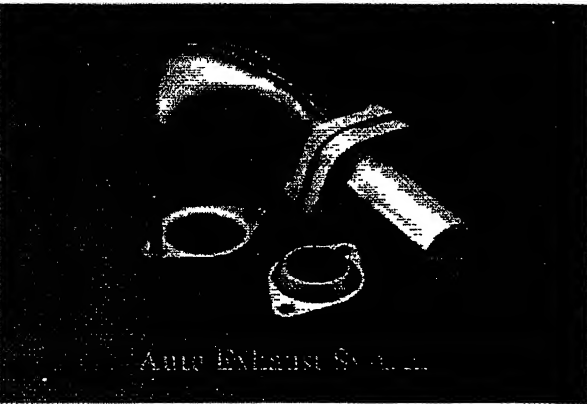


Figure 2.6 Some typical P/M stainless steel products [12].

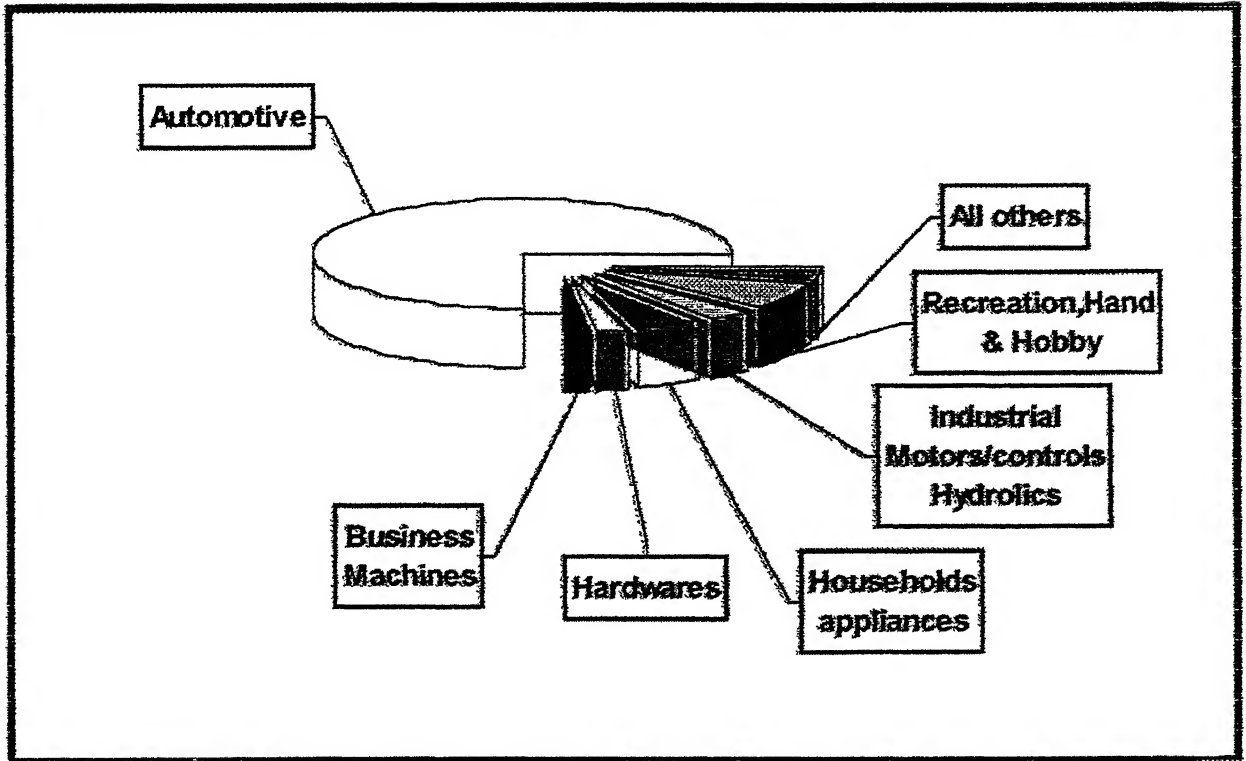


Figure 2.7 P/M parts market [12].

Table 2.3 Application of sintered stainless steel [1]

Application area	Alloy
<i>Automotive</i>	
Exhaust system flanges	409L, 434L
Sensor bosses	409L, 434L
Antilock Breaking System sensor ring	410L, 434L
Rearview mirror mounts	434L, 430L, 316L
Brake components	434L
Seat belt locks	304L
Windshield wiper pinion	410L
Windshield wiper arms	316L
Manifold heat control valves	304L
<i>Hardware</i>	
Lock components	304L, 316L
Threaded fasteners	303L
Fasteners	303L, 304L, 316L
Quick-disconnect levers	303L, 316L
Spacers and washers	316L
<i>Electrical and Electronic</i>	
Limit switches	410L
G-frame motor sleeves	303L
Rotatory switches	316L
Magnetic clutches	410L
Electrical testing probe jaws	316L
<i>Industrial</i>	
Water and gas meter parts	316L
Filters- liquid and gas	316L
Recording fuel meters	303L
Fuel flow meter devices	410L
Pipe flange clamps	316L
Plumbing fixtures	303L
Sprinkler system nozzles	316L
Shower heads	316L
Window hardware	304L, 316L
<i>Office equipments</i>	
Non-magnetic cards stops	316L
Dictating machine switches	316L
Computers knobs	316L
<i>Miscellaneous</i>	
Coins, medallions	316L
Dental equipments	304L
Watch cases	316L
Fishing rod guides	304L, 316L
Photographic equipments	316L
Cam cleats	304L
Dishwashers components	304L
Can opener gears	410L

Powder metallurgy by definition, is a process whereby a solid metal, alloy or an ceramic in the form of a mass of dry particles, normally less than 150 μm in diameter, is converted into an engineering component of pre-determined shape and processing properties which allows it to be used in most of the cases without further processing [13]. There are three important steps while processing a powder metallurgical product. They are follows -

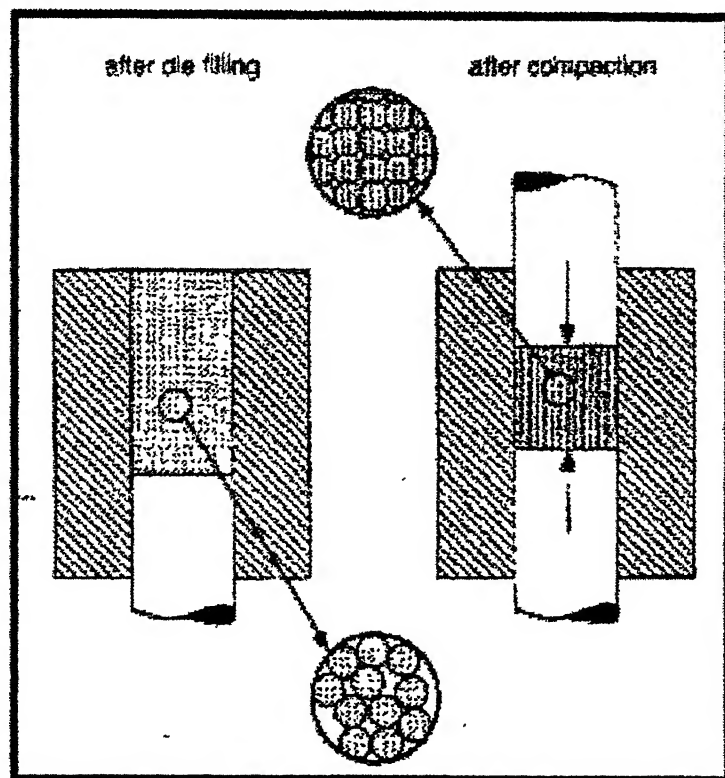
- (i) Powder production
- (ii) Powder compaction
- (iii) Sintering

Ferrous metal powders can be produced by several physical, chemical and mechanical methods listed in Table 2.4. Atomization is the important process by which metal powders are prepared. The dispersion of a molten metal into particles by a high pressure gas or water stream is called atomization [13]. Powders of high purity are produced electrolytically. The behavior of powder during the subsequent consolidation process is determined by both particle and bulk properties. A powder is characterized, therefore, not only by chemical composition but also through particle shape, size and surface chemistry and in bulk by compressibility. Stainless steel powders are produced normally in the prealloyed form since it has heavy alloying additions. Producing stainless steel by premixed powders will result in a non-homogenous mixture. Stainless steel powders are produced by water atomization and gas atomization techniques.

The metal powders are compacted into required shape and size in a die. The powders are transferred into a die and uniaxial pressure is applied on the die to produce a green compact. During compaction the powders get compressed and attain a certain density called the green density. A lubricant is used in order to reduce the

Table 2.4 Production of ferrous metal powders [14].

Powder Production Techniques	Powder Shape
Mechanical technique	Irregular
Electrolytic technique	Dendritic or sponge like
Oxide reduction and reaction	Sponge
Carbonyl decomposition	Nearly spherical
Atomization	
a) gas atomization	a) Spherical
b) water atomization	b) Nearly rounded
c) centrifugal atomization	c) Spherical
Vaporization technique	Faceted or cubic

**Figure 2.8** Densification during compaction by changes in particle arrangement and shape [13]

friction by the die walls and for easy removal of the compressed sample [13] The densification of the powders during the compaction is shown in the Figure 2 8.

The compacted green sample is then subjected to a thermal treatment called 'sintering' in air or in reducing atmosphere or in vacuum. Atmospheric sintering is used only in case of ceramics as most of the metals get oxidized if sintered in atmosphere. For metals a reducing atmosphere or vacuum or an inert atmosphere is used. A reducing atmosphere is usually preferred as the oxides that are present on the surface of the atomized powders get reduced during sintering. Depending upon the sample composition the sintering temperature, time and atmosphere are selected. During sintering lubricant is evaporated and porosity is reduced by metal transport involving surface and volume diffusion. This leads to chemical bonding of the particulate. As sintering proceeds, the original inter-connected porosity is reduced, closed pores are formed, and the overall shrinkage is controlled to ensure the final dimensions of the compact come within the required engineering tolerances [14]

2.5 Sintering

Sintering is binding the particles together at high temperatures. Sintering may be considered the process by which an assembly of particles, compacted under pressure or simply confined in a container, chemically bond themselves into a coherent body under the influence of an elevated temperature. The temperature is usually below the melting point of the major constituent [15]. Sintering can also be defined as a thermal treatment for bonding of particles into a coherent predominately solid structure by mass transfer events that usually occur on the atomic levels [16]. The driving force for any solid state sintering is the decrease in the total surface energy, which occurs by reduction in surface area with formation of inter-particle

bonds. Accompanying the inter-particle bonding are significant changes in the pore structure and compact properties such as strength, ductility, conductivity, magnetic permeability, and corrosion resistance. There are several variants that affect a sintering process such as the presence of multiple phases, application of pressure, sintering time, sintering temperature, particle size, presence of activators etc. Based on the application of pressure sintering is divided into two major classes as pressure assisted and pressure-less sintering. Most of the sintering operations are performed in the absence of external pressure called pressure-less sintering. But for many high performance applications, high densities are attained by means of an external pressure during sintering. The Figure 2.9 shows the various types of sintering operations that are used [16].

For understanding the basic concepts of sintering, considering the simplest approach of two spherical particles that are in contact with each other as shown in Figure 2.10 In the powder compact, there will be many such contacts as shown in the figure. As the sintering process progresses the bonds at the contacts enlarge and at each contact a grain boundary grows to replace the solid-vapor interface. If the process prolongs for a longer time then these two particles will coalesce to form as a single particle of 1.26 times the original diameter [17].

There are various mechanisms proposed for the particle diffusion at the neck area. The various processes that can occur at the neck area during sintering are shown in the Figure 2.11 [13]. There are three main stages that take place during a normal sintering operation. During the initial stage point contacts in the particles are transformed into sintered bridges called as necks. After sometime the neck growth takes place and the grain boundaries are formed between two adjacent particles in the plane of contact. In the second stage the pore structure becomes smoother and has an

interconnected, cylindrical nature as the properties of the compacts develop. A coherent network of pores is formed at the grain boundaries and a new microstructure develops. In the final stage of sintering, the isolated pores become spheroids. The places where the gases cannot be diffused out are enclosed and further densification becomes impossible as soon as the gas pressure reaches equilibrium with the surface tension.

2.5.1 Solid-State Sintering

Solid state sintering is carried out at temperature (T_s at composition X_s) below the solidus line/ melting point of the constituent powders as shown in Figure 2.12. The driving force for solid state sintering is excess surface free energy. Sintering is a complex process and for any given metal and set of sintering conditions there are likely to be different stages, driving forces and material transport mechanisms associated with the process.

Different Stages of Solid-State Sintering

One of the basic aspects of sintering is that it usually takes place at a constant temperature and the time is varied to achieve certain result. Consequently, it becomes useful to attempt to describe the stages of sintering in terms of their relative order with respect to time. According to R.M German and Hirschhorn [15,16] solids state sintering is divided into six stages:

- (i) Interparticle bonding among particles
- (ii) Neck growth
- (iii) Closure of pore channels
- (iv) Rounding of pores
- (v) Pore shrinkage (densification)

- (vi) Pore coarsening

2.5.1.1 Limitations of Solid-State Sintering

Solid state sintering process has some limitations These are follows:

- (a) As the whole solid-state sintering process occurs in solid-state, the diffusion rate is slow compared to the other sintering process. So, this process takes more time than others.
- (b) Generally the sintering concept deals with the powders of spherical shapes that sinter under isothermal conditions But in reality, most of the powders are non-spherical in nature with wide particle size distributions.
- (c) Compaction repacking the particles, collapses large pores, and enlarges the particle contact but may introduce new defects.
- (d) It should be noted that, though we are providing the holding time at maximum temperature, most of the bonding between particles occurs prior to that.
- (e) Again the assumption of isothermal conditions may not be valid for most of the models. Actually, the compact faces a very dynamic situation, with gradients introduced by thermal stresses and atmospheric interaction. In many cases the gradients have a significant effect on the sintering process [16].

Because of these problems, the available diffusion data does not always reflect the actual sintering processes. In industry the heating rate is not very slow and sintering time is short also. This will lead to the errors in actual calculation. However, these problems have been reconciled by the use of new computer simulation techniques that attempt to embrace all of the complexities of real sintering situations [19].

SINTERING PATHWAYS

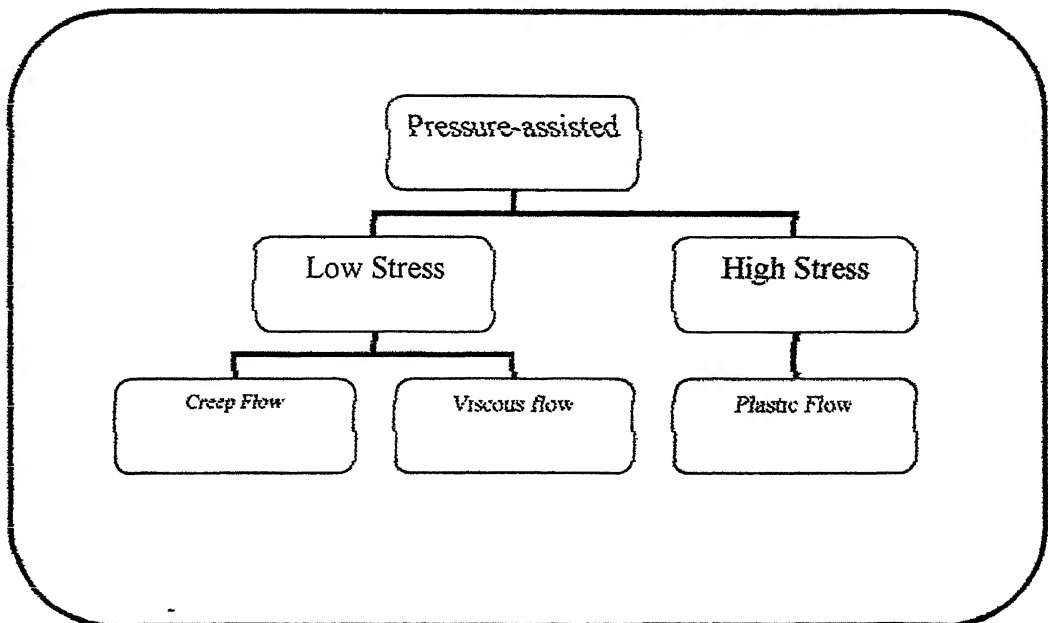
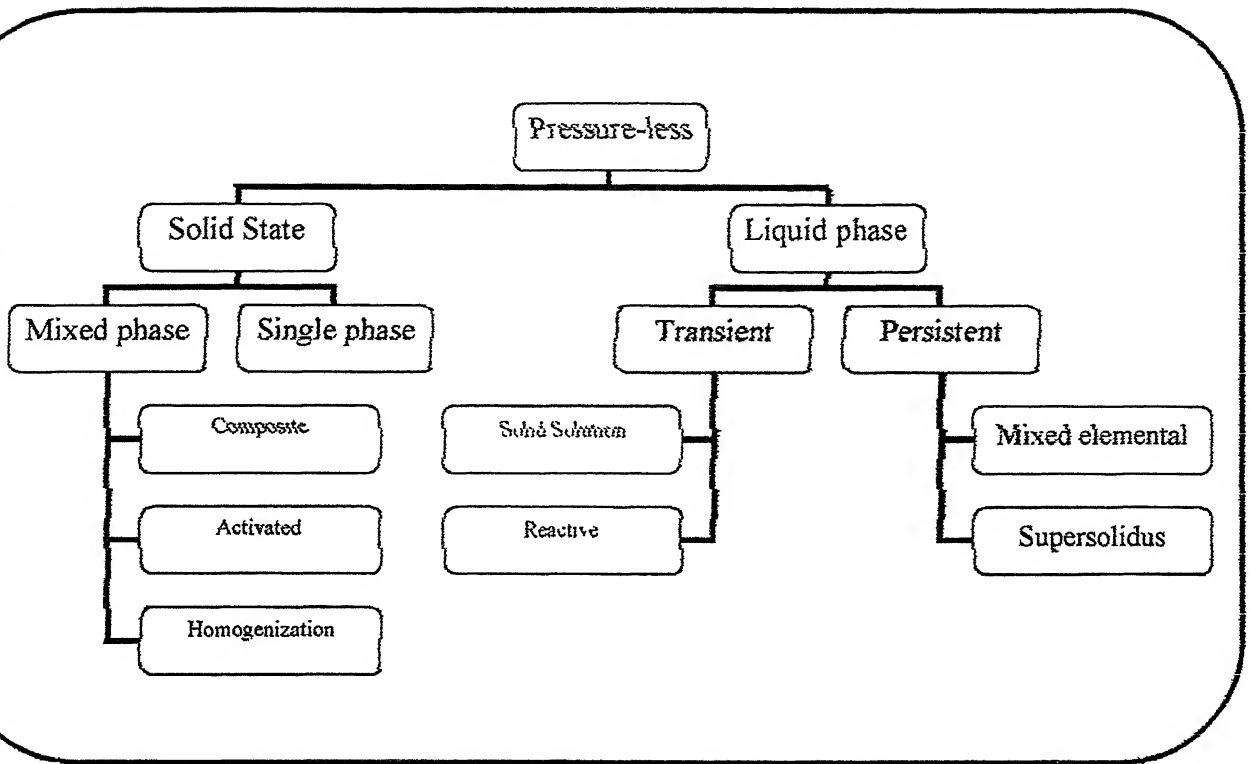


Figure 2.9 Map of sintering process and the subdivisions in terms of the key processing parameters [16].

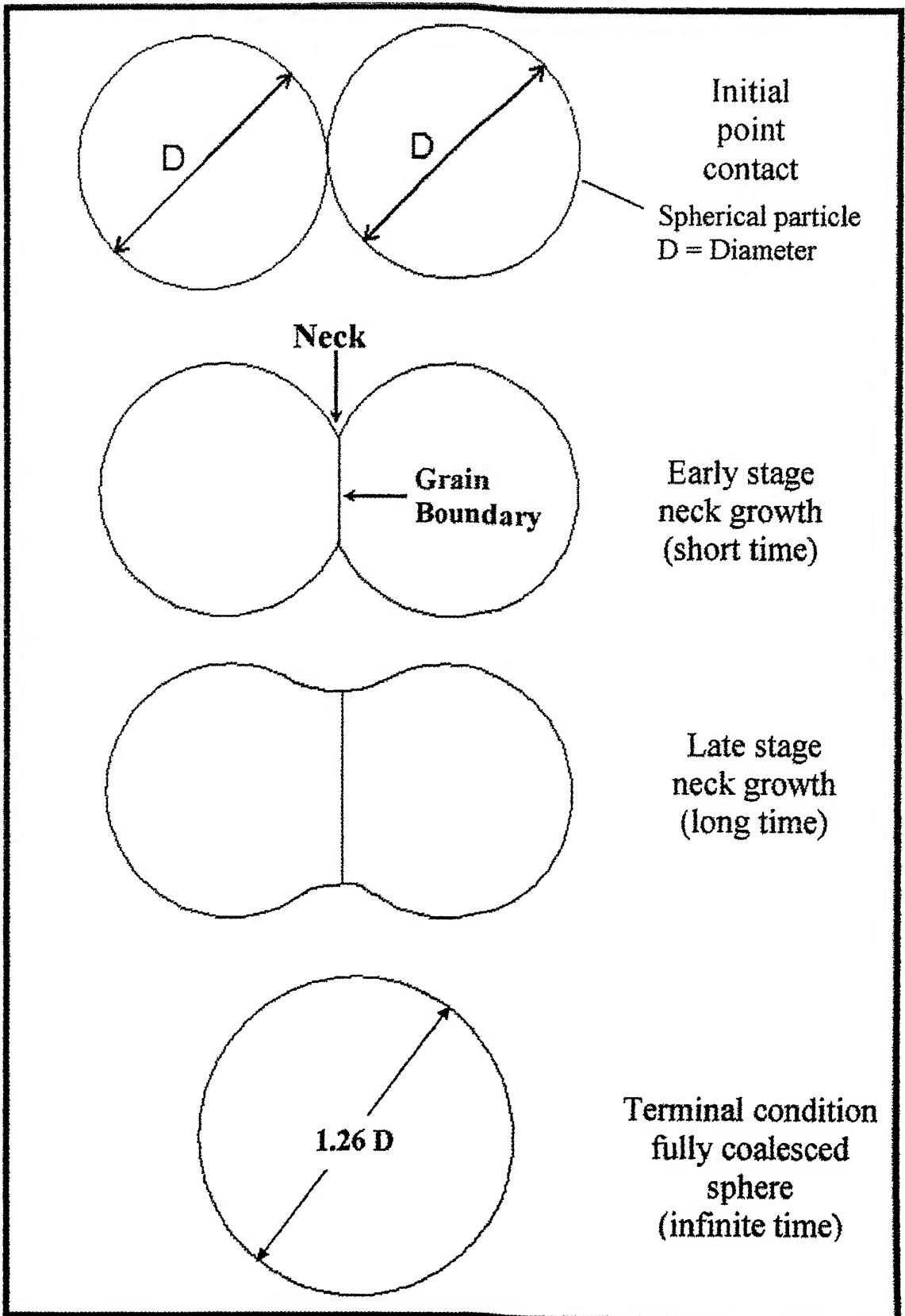


Figure 2.10 Two sphere sintering model [17].

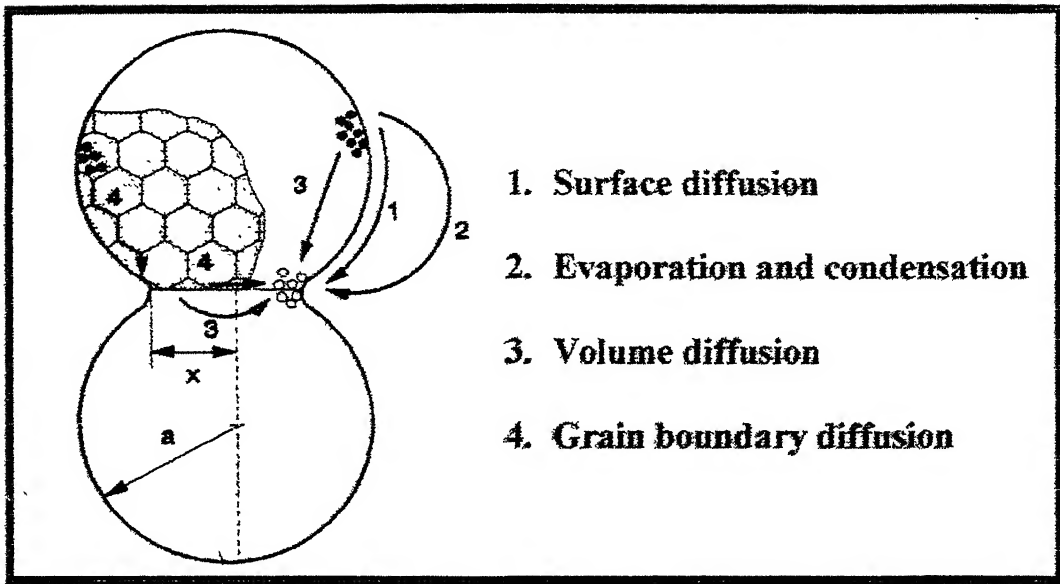


Figure 2.11 Possible sintering mechanisms at the neck area [13].

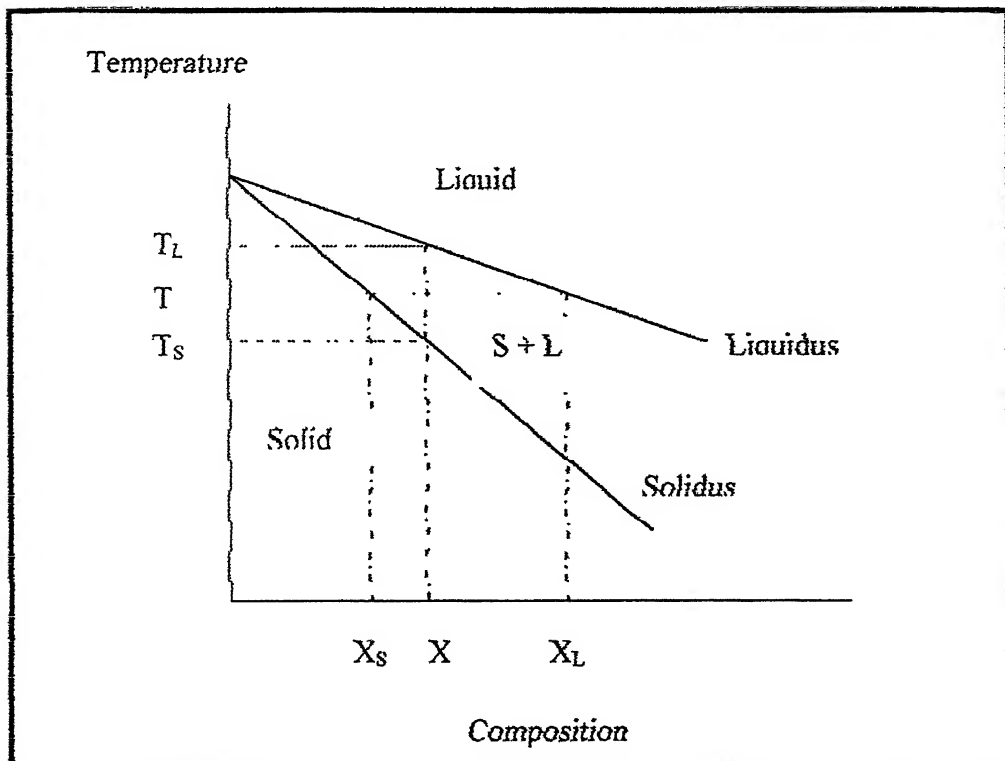


Figure 2.12 Schematic phase diagram showing different temperature of sintering.

2.5.2 Liquid Phase Sintering

Liquid phase sintering is a widely used fabrication process in powder metallurgy for both metallic and ceramic products. Pressure-less sintering often requires the presence of liquid to eliminate all porosity or to achieve a desired amount of chemical homogenization. The liquid phase sintering is carried out at temperature (T_L at composition X_S) above the melting point of one of the constituent powders as shown in Figure 2.12. In such a system the liquid formed will enhance mass transport and therefore rapid sintering. Liquid phase sintering may be defined as sintering involving a coexisting liquid and particulate solid during some part of the thermal cycle [19]. The liquid phase during sintering can be obtained by two different ways, one by melting one of the components during sintering or by formation of a eutectic melt. Also the liquid phase formed may be transient or persistent during sintering depending upon the solubility relationship. Beyond this a prealloyed powder can be sintered by having the sintering temperature between the solidus and liquidus temperatures. This is called as supersolidus liquid phase sintering [21]. The ideal phase diagram for liquid phase sintering is shown in the Figure 2.13. The main requirements for liquid phase sintering are high melting point difference between the solid phase and the forming liquid phase and there should not be any high temperature intermediate phase formation. In order to avoid swelling, the solubility of the solid phase in the liquid phase should be higher than the solubility of liquid phase in solid. The driving force for liquid phase sintering is the reduction in interface energy [16]. The effect of liquid phase on the densification in liquid phase sintering is shown in the Figure 2.14. The figure shows the stages of liquid phase sintering and the effect of liquid volume on the sintered density. Huppmann *et.al.* [21] studied the elementary stages of liquid phase sintering and reported in detail. In the absence of any liquid,

sintering takes place by solid state sintering. On the other hand if there is excess of liquid phase then the compact may not hold its shape and slumping of the sample may occur. When the liquid content is intermittent, then the compact holds the shape but the liquid is not enough to fill the void spaces. In this case densification is increased by rearrangement of particles due to capillary force and then by solution reprecipitation.

The various stages of the evolution of a classical liquid phase sintering microstructure are shown in the Figure 2.15. The three main stages of liquid phase sintering are: particle rearrangement, solution-reprecipitation, and final-stage sintering through particle coarsening. During the initial stages the densification takes place by solid state sintering of the solid particles. As the temperature further increases, the low melting phase forms liquid. The solid particles will dissolve within the liquid and rearrangement process occurs. The liquid phase formed acts as a carrier for the solid particles in solution reprecipitation stage, wherein the smaller grains get preferentially dissolved in the liquid and after crossing the solubility limit reprecipitated on the larger grains. The last stage will be densification of the solid skeleton formed and pore rounding takes place resulting in the final product.

2.5.2.1 Transient Liquid Phase Sintering

An interesting variant to traditional liquid phase sintering involves a transient liquid which solidifies by diffusional homogenization during sintering [20]. In this processes liquid exists for a certain length of time during the sintering cycle. In many material systems, starting a sintering cycle with a mixture of powders will allow a transient liquid phase to form during sintering. Common examples are Fe-Cu, Fe-Ti etc. systems. In Fe-Cu system, the molten copper dissolves into iron to leave behind a

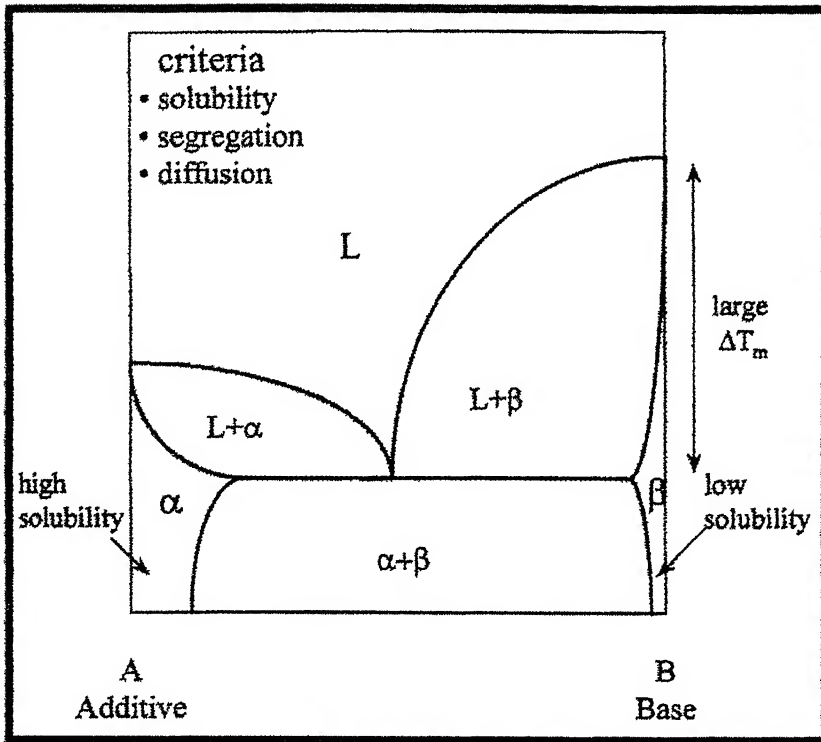


Figure 2.13 Ideal phase diagram for liquid phase sintering [16].

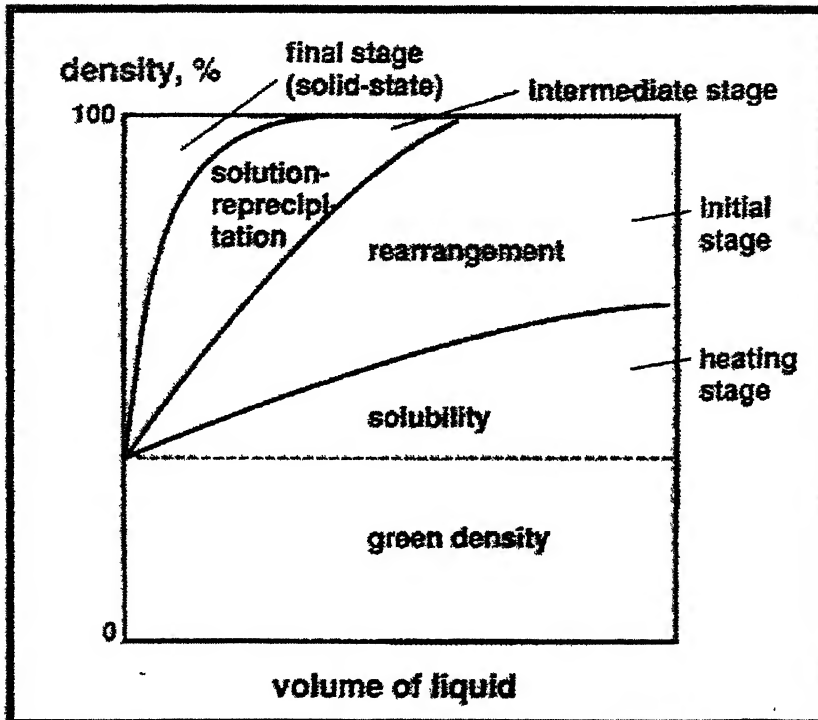


Figure 2.14 A map of density versus liquid content with indications of the dominant regions [16]

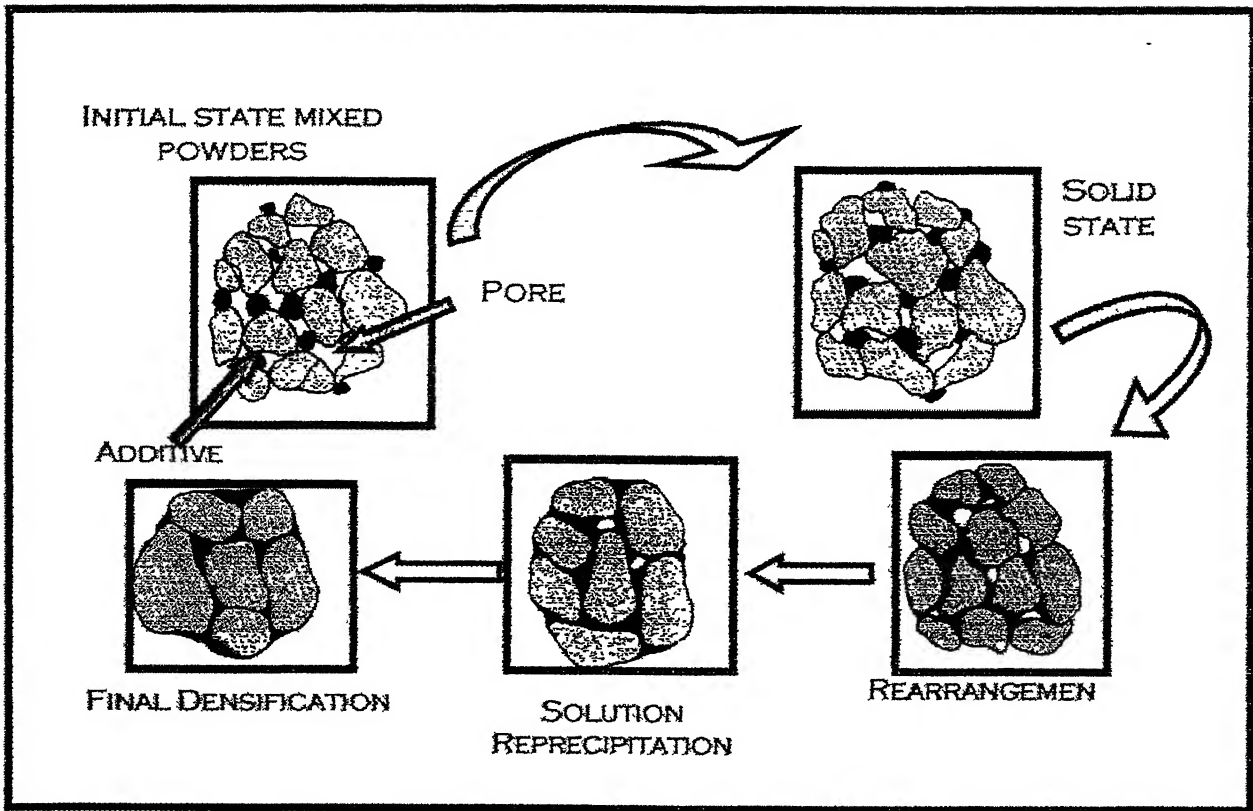


Figure 2.15 The classic stages of liquid phase sintering involving mixed powders which form a liquid on heating [16].

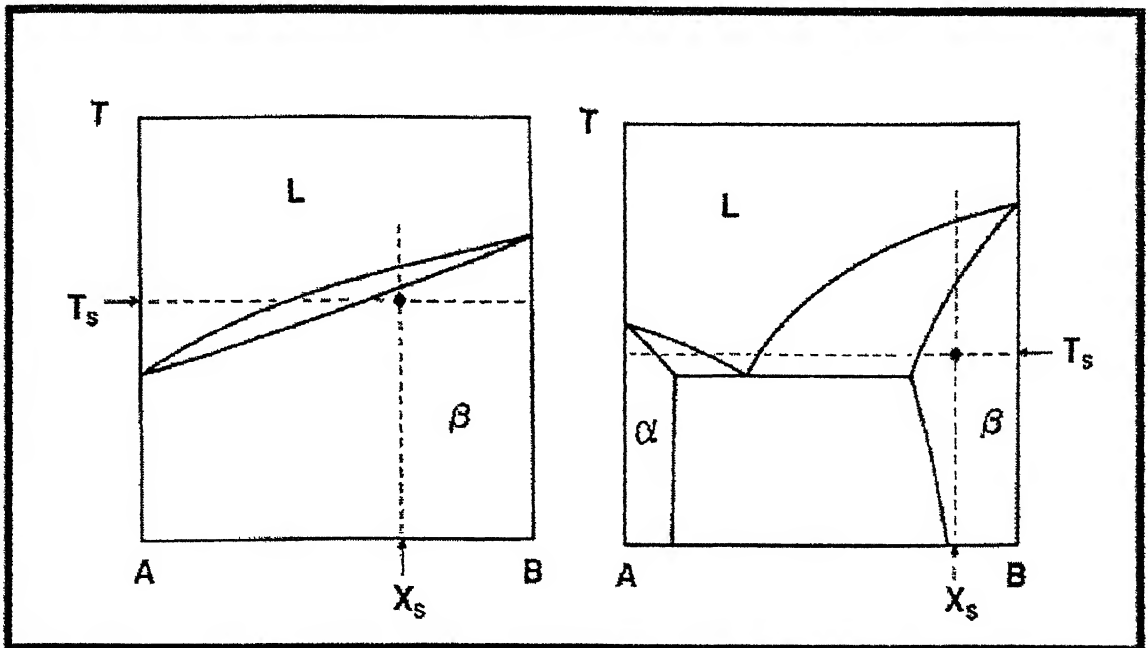


Figure 2.16 Two binary phase diagrams showing possible conditions where transient liquid phase sintering can occur [16].

pore which is called a secondary pore. Figure 2 16 gives the example phase diagrams of systems that could be processed using a transient liquid from mixed A and B powders. In first case, a low melting temperature additive, A is used to generate the liquid, yet the overall composition is in a single-phase region at the sintering temperature. The sintering temperature is between the melting temperatures of the two components. Most importantly the solid does not change the crystal structure due to alloying with the liquid. Liquid can form during this process by eutectic formation. This eutectic reaction provides the liquid from inter-diffusion of the components during sintering. The sintering temperature is greater than the eutectic temperature and the final composition is in the single phase field. As the amount of liquid varies continuously, the process becomes very temperature sensitive.

The requirements for transient liquid phase sintering include solubility between the components, with the final composition existing within a single phase region at the peak sintering temperature. Finally we can summarize the sequences of steps as follows [22,23]:

1. Swelling by inter-diffusion prior to melt formation
2. Melt formation
3. Spreading of the melt and generation of pores at prior additive particle sites
4. Melt penetration along solid-solid contacts
5. Rearrangement of the solid grains
6. Solution reprecipitation induced densification
7. Diffusional homogenization
8. Loss of melt
9. Formation of a rigid solid structure
10. Densification by solid state sintering

It is to be remembered that the actual steps depend on several process variables, including particle sizes, amount of additive, heating rate, and maximum temperature.

A detailed investigation of the dependence of transient liquid phase sintering on phase diagram is discussed by German [24]. The benefits of transient liquid phase sintering are easy compaction of elemental powders (as opposed to prealloyed powders) and excellent sintering without coarsening difficulties associated with a persistent liquid. Transient liquid phase sintering can be applied in processing of dental amalgams based on silver and mercury, porous bronze bearings, structural ferrous alloys, copper alloys, magnetic materials and alumina-based ceramics. Problems can arise in TLPS if an intermediate compound forms between the additive and the base. A system with an intermediate compound would be expected to give swelling. However, for applications such as porous bronze bearings this swelling is beneficial. Modeling of transient liquid phase bonding in the real system has been tried by researchers [25].

The possible advantages of this are clear. Primarily TLPS offers increased flexibilities in design and processing [26]. The other advantages of TLPS include a reduction in the processing temperature, enhanced densification, reduced microstructural coarsening and reduced cost by avoiding the use of expensive prealloyed powders [27].

2.5.2.2 Supersolidus Liquid Phase Sintering

There is always a continual move to improve the processing and properties of sintered products. The main driving force for this is to attain lower processing cost and improved products. In case of liquid phase sintering the final properties of the

product rely upon the liquid phase and lots of research has been made to improve the properties by altering the properties of liquid phase. The use of prealloyed powders led to the new process in liquid phase sintering called as supersolidus liquid phase sintering (SLPS). SLPS involves heating a prealloyed powder at temperature T at the composition X as shown in the Figure 2 12; between the solidus and liquidus temperature to form liquid phase [30,31]. SLPS is similar to that of transient liquid phase sintering, but the major difference is the use of prealloyed powders. During SLPS the liquid phase forms within the particles, causing each particle to split into individual grains [16]. The fragmented particles undergo repacking, giving a homogenous distribution of liquid. The resulting sintering rate is rapid once the liquid is formed due to capillary action.

The various stages of densification during SLPS of a prealloyed polycrystalline powder are shown in Figure 2 17. The steps of SLPS are liquid formation, particle fragmentation, fragment rearrangement, grain packing and sliding, coarsening, and eventual pore elimination by solution-reprecipitation. In the first stage, the melt formation occurs as the prealloyed powder is heated above the solidus temperature. The liquid is formed commonly at the grain boundaries within the particles, in the inter-particle neck region and the grain interior. The liquid volume increases with temperature and at a critical temperature above solidus, the threshold amount of liquid exists along the grain boundaries of a polycrystalline particle [30]. Above the threshold the grain possess enough mobility to rearrange. The rearrangement of solid grains occurs under the influence of the capillary force by the wetting liquid. The second stage of SLPS involves solution-reprecipitation, wherein the small grains dissolve and re-precipitate on larger grains. In the final stage the solid skeleton forms and densification is slow as it is controlled by solid-state diffusion.

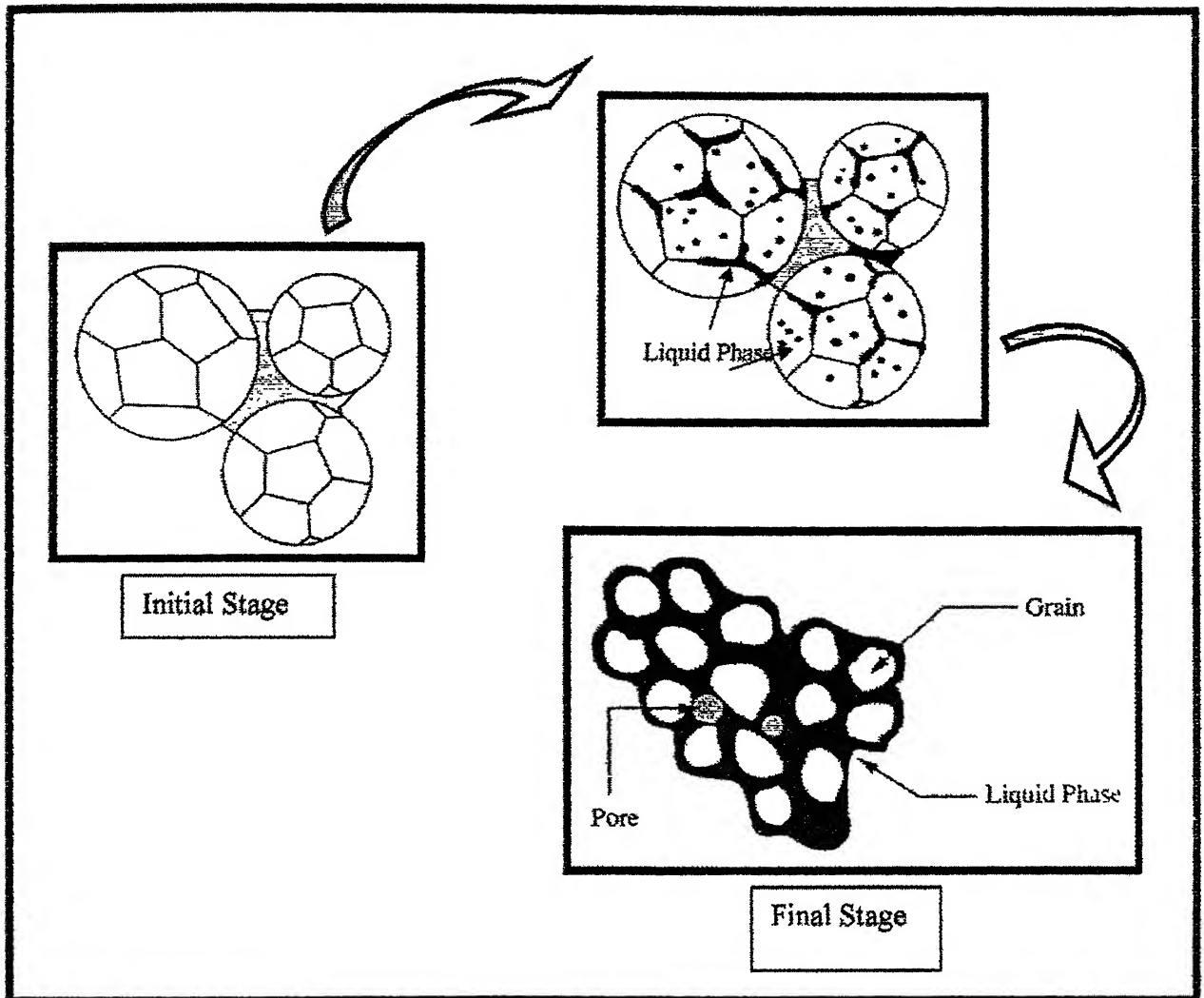


Figure 2.17. Schematic diagram of densification process during supersolidus liquid phase sintering [30].

2.5.2.2.1 Previous Research on SLPS

The first work on SLPS was reported by Westerman [31] on prealloyed nickel-base superalloy. From this study it was noticed that near theoretical densities was obtained by incipient melting of grain boundaries. The mechanism of SLPS was explained by Lund and Bala [32]. They suggested that mechanisms responsible for densification included,

- (i) Redistribution of liquid formed due to melting at particle contacts
- (ii) Fattening of the wetted particle contacts by a solution-precipitation mechanism
- (iii) Grain growth due to solution-precipitation leading to release of intergranular liquid
- (iv) Pore elimination due to the escape of the entrapped gas by diffusion.

Extensive work on densification mechanisms and microstructural evolution during SLPS of prealloyed powders was carried out by Tandon [30]. He worked on sintering mechanisms used for a wide range of alloys like Ni-based super alloys, austenitic stainless steel and bronze powders. The same author interfaced the effect of boron additions in austenitic stainless steel and obtained sintered densities up to 96% theoretical [33]. Lal worked on mechanisms and mechanics of shape loss during SLPS on various prealloyed powders, including bronze, 316L stainless steel and T15 tool steel. He investigated the shape loss during SLPS and rationalized the processing and material factors with regard to distortion [34].

Lal *et al.* [35] examined densification during SLPS of a mixture of two Ni-base superalloys. To one of the mixtures boron is added and it was observed that it had a lower melting temperature. This enhanced the densification of the sintered component. German examined the interplay of processing variables to obtain full-

density, distortion-free shapes from prealloyed powders [36]. Extensive research has been carried out in order to understand the densification during SLPS by modeling. Liu *et al.* [39,40] modeled for capillary action and densification for supersolidus liquid phase sintering

2.5.2.2.2 Parameters affecting SLPS

Both material and processing parameters affects SLPS [14,16,30,41,42].

Material Parameter: These are follows:

- (i) Phase Diagram
- (ii) Chemical constituent of the alloy

Processing Parameter: These are follows:

- (i) Liquid volume fraction
- (ii) Sintering temperature
- (iii) Sintering time
- (iv) Sintering atmosphere
- (v) Powder characteristics
- (vi) Heating rate

2.5.2.2.3 Limitations of SLPS

In spite of all the advantages, supersolidus liquid phase sintering suffers from certain disadvantages. These are as follows.

- (a) The major problem is the compact distortion. It is occurred due to too much liquid during sintering.
- (b) The alloying level should be reasonably high on a volume basis which helps to the

2.6 P/M Processing of Stainless Steel using Boride and Copper

Addition

2.6.1 Densification Mechanisms

Solid state sintered P/M stainless steels contain up to 15 volume percent porosity. It is because diffusion in solid state takes place which is a very slow process. This is detrimental to both mechanical properties and corrosion resistance. The as-sintered compacts therefore require post sintering secondary operations, such as hot pressing, re-pressing and re-sintering, and forging which further increases cost. Significant cost savings, both in processing and equipments, are possible by increasing the sintering temperature to the supersolidus region. Another approach to enhance the density of the final products is the use of additives which act as a sintering aid. In addition, to activating densification during sintering some of the sintering additives play a significant role in final mechanical and corrosion properties [41].

Of the several sintering aids that have been used for ferrous materials, boron is the most useful one which can be added in its elemental form or as a compound. Another effective sintering aid is copper which forms liquid at sintering temperature [41].

The densification mechanisms of borides and copper are different though both form liquid at the sintering temperature. Borides suppress the solidus line of austenitic stainless steel while it forms persistent liquid phase at sintering temperature for ferritic stainless steel [28]. On the other hand, copper forms transient liquid phase at sintering temperature for both grades (434L and 316L) of stainless steel.

Addition of Borides

Investigation in the sintering of iron-boron alloys has its genesis in the early 1970s [42] with the research on developing superior wear resistance materials. The use of boron in steels, at concentration level of less than 50 ppm, was investigated extensively prior to this period, but boron was not used on sintering of material processing.

Mashkov *et al.* [43] were among the first to infiltrate the green and pre-sintered porous compacts of reduced iron powders with amorphous boron and low melting iron boride alloys. All the specimens were found to execute shrinkage after infiltration. Klien [44] reported that rapid heating of carbonyl iron powder mixed with elemental boron powder (up to 0.97 wt. %) to a temperature of 1175°C resulted in sintered densities close to the theoretical density.

Madan and German [45] systematically investigated the densification mechanisms of water atomized iron powders and carbonyl iron powders at sintered at 1200°C. They observed that rapid densification occurred at 1174°C, the eutectic temperature of iron-iron boride. Above the eutectic temperature, liquid phase nucleates at the particle contacts. A combination of solubility between the liquid and the solid phases and a chemical reaction between the phases promotes favorable wetting and spreading characteristics [16]. Iron boride has negligible solubility in iron as seen from the Fe-B phase diagram in Figure 2.18. Hence, it segregates at the grain boundary. The eutectic liquid penetrates the grain boundary to reduce the interfacial energy and forms a segregated layer responsible for rapid sintering. Subsequent densification is achieved by grain shape accommodation into solution reprecipitation [45,46]. Penetration of the iron grain boundary by eutectic liquid results in a coarse microstructure with a continuous borides phase along the boundaries.

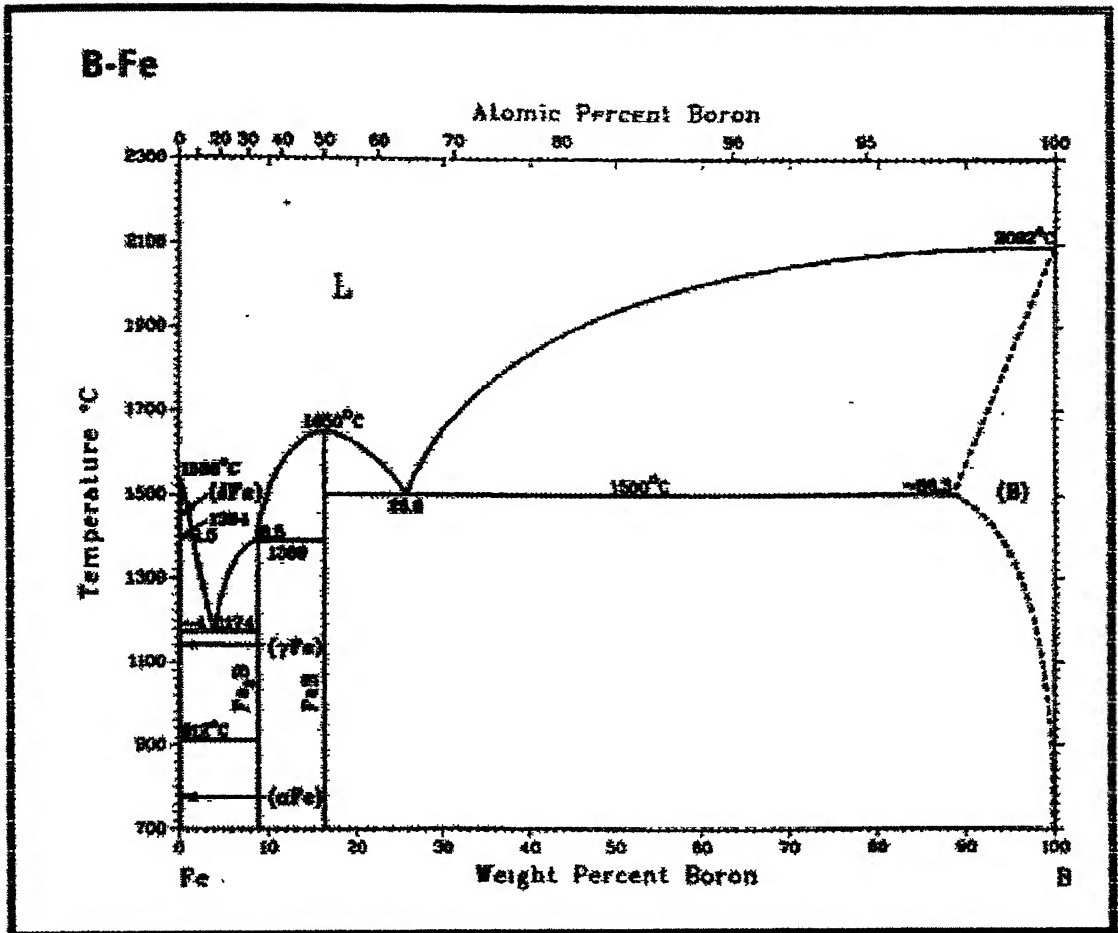


Figure 2.18 Binary phase diagram of Fe-B [7].

Dudrova *et al.* [47] conducted a similar study on coarse steel powders, iron prealloyed with Mo. In their study, they observed that the presence of Mo reduces the amount of eutectic liquid. Boron diffuses rapidly in iron and interacts with Mo. Molybdenum is a strong boride former, reacting with boron to give MoB, Mo₂B, and MoB₂. Due to this boride formation amount of liquid phase decreases.

Coubiere *et al.* [48] investigated the microstructure evolution of iron-boron alloy. The focus in their study was to evaluate the use of iron-iron boride cermets as wear resistance materials. Consequently, a large amount of boron in the range of 3.8 to 8.8 wt. % was used in their experiments. Sintering above 1174°C, the microstructure revealed continuous layer of iron boride along iron particle boundaries. These experimental results indicate the propensity of boride to precipitate and form a continuous layer along the particle boundaries. The continuous layer of boride is detrimental to the ductility of the sintered alloy.

Xiu *et al.* [49] used Fe-B and Fe-C master alloys in sintering of Fe-Mo steel. With the Fe-C master alloy as the source of carbon in the Fe-1.2Mo-0.4B-0.5C alloy, sintered at 1120°C for 1 hour in hydrogen, they observed a sintered density of around 99% theoretical. A rapid sintering rates and high densification were attributed to interaction of boron and carbon. The local composition at the Fe-B and Fe-C particles result in the formation of ternary eutectic liquid of Fe-B-C at 1097°C. Molybdenum and boron segregated at the grain boundaries in the sintered microstructures. Such a densification behavior was not observed while using graphite as the source of carbon. In such case, the difference in local carbon composition results in the formation of boroncarbides instead of ternary liquid [50].

German *et al.* [70] used boron in the form of NiB. According to them by

resulted dual phase microstructure in 316L, consisting of precipitate-free and precipitate-rich grains. The sintering was aided by the formation of a transient liquid via a peritectic reaction at 1035°C as shown Ni-B phase diagram in Figure 2 19. The dual phase structure resulted from the localized increase in nickel concentration associated with the NiB additions. Nickel stabilizes the austenite and forms precipitated-free grains. This indicates that a minimum Cr concentration is necessary for precipitate formation.

Addition of copper

Copper infiltration did not enjoy immediate commercial success when it was first introduced to industry in 1920s due to the fact that the process was characterized by excessive growth, erosion, and unstable growth pattern. The problem of erosion was solved in 1943 by the addition of iron to the infiltrant, at the sintering equilibrium concentration, of 4 wt. % [51,52].

Copper contributes significantly to improve the corrosion resistance of stainless steels. Porosity is affected by both the compaction pressure and the copper content. In the later case, and increase in the volume fraction of pores is induced by swelling during sintering of iron copper which is responsible for the distribution of pore area over a wide range. Sintering of iron-copper is in fact liquid phase sintering, as the sintering treatment is carried out above the melting point of copper. Depending of the copper content the liquid phase may be stable or transient at the usual sintering temperatures approximately 9 wt. % copper being soluble in gamma iron. Improved corrosion resistance after copper addition has been attributed to the enhancement of the passivation process of sintered austenitic stainless steel due to the cathodic depolarization effect of hydrogen evolution and oxygen reduction. Copper inhibits the

attack of 316L in H_2SO_4 by shifting the corrosion potential from an active to passive state [2]

2.6.2 Effect of sintering atmosphere

Boron reacts readily with oxygen and nitrogen in the temperature range of 300 to 1000°C to form oxides and nitrides, respectively [53]. Boron also reduces metallic oxides especially in the presence of hydrogen or carbon at elevated temperature with the formation of B_2O_3 , a highly volatile compound [54]. Loss of boron due to its reaction with the sintering atmosphere or oxide impurities adversely affects densification.

Canon *et al.* [55] in their experiments with the sintering of 316L stainless steel powder with boron addition observed that full density could not be attained at a temperature as high as 1260°C when sintered in a 50% N_2 –50% H_2 atmosphere due to a loss of boron. Similarly, Rosso *et al.* [56] did not observe any significant densification of high Mo-Fe prealloyed powder with boron additions when sintered in a 76% N_2 –19% H_2 –5% CH_4 atmosphere. Densification is hindered by the loss of boron and the formation of boron nitride (BN), which has a low solubility in steel.

Sintering of ferrous alloys with the boron dictates the necessity of sintering atmosphere by avoiding N_2 or O_2 . To overcome this problem is added in the form of borides such as FeB or NiB.

On the other hand when the sintering of stainless steels is done in the atmosphere of H_2/N_2 , copper reduces N_2 absorption from the atmosphere, and therefore it reduces the extent of chromium nitride precipitation.

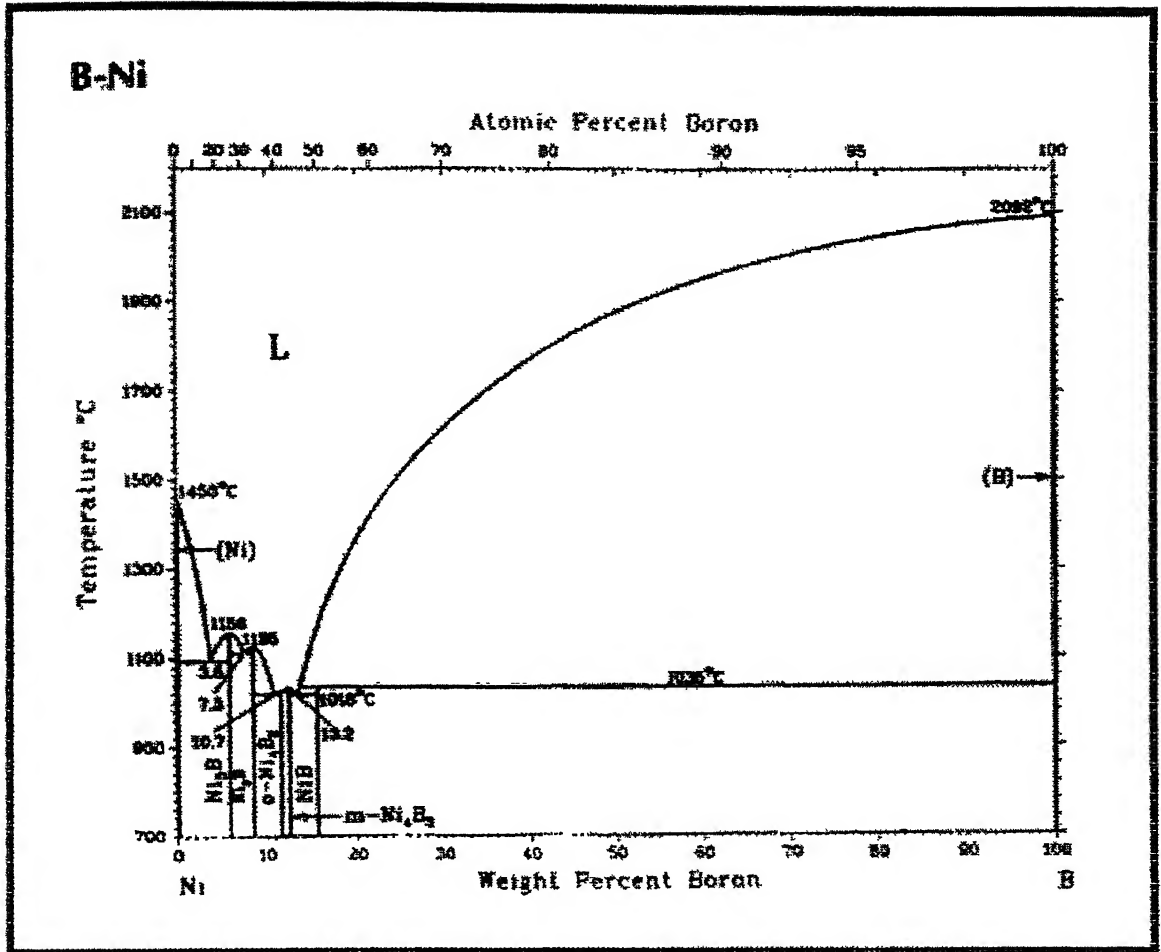


Figure 2.19 Binary phase diagram of Ni-B [7].

2.6.3 Effect of Additives on Mechanical Properties

Borides are preferentially segregated along grain boundaries and increasing the strength and hardenability of steel [43]. Transition metal borides exhibit high hardness, high melting point and extreme brittleness. Hence, it is expected the presence of borides either as dispersed or continuous phase would significantly affect the mechanical properties of the sintered materials.

Increase in boron content contributes to an increase in strength. This is because of combination of reduced porosity and borides phase reinforcement. Madan and German [57] in their experiments with coarse iron powders ($D_{50} = 80\mu\text{m}$) reported an increase in strength and a decrease in elongation with increasing boron content when sintered at 1200°C for an hour.

Molinari *et al.* [58] observed that the increase in mechanical properties of 316L stainless steel sintered with boron is a combination of density and boride content. German and Tandon [40] showed the effect of boron and FeB addition on tensile strength and elongation of 316L stainless steel. On addition of 0.5 wt. % elemental boron the tensile strength increased 15% but ductility decreased 50% compared to pure 316L. Similar trend was also observed in NiB addition.

Copper has only a small influence on mechanical properties. It enhances the mechanical properties by decreasing porosity. Percentage elongation and UTS both decrease with an increase in copper content. Thus, it is possible to optimize the processing of copper alloyed sintered stainless steel [2].

2.7 A Review of P/M Stainless Steels

Extensive research has been carried out on P/M stainless steel regarding their sintered density, mechanical properties and corrosion resistance properties [59-77].

Tiziani *et al.* [59] studied liquid phase sintering of 316L stainless steel with 20% copper using N_2-H_2 atmosphere. Copper additions improved the sinterability. They reported that the corrosion properties of the sintered component also enhanced due to the addition of copper.

Wang and Su [60] added silicon powder to 304L stainless steel and studied the liquid phase sintering behavior of the component. Silicon additions profoundly activated the sintering process by the formation of a eutectic ferrite. They reported that the final product was a duplex stainless steel product with austenite-ferrite structure.

P/M Stainless steel components from prealloyed water atomized powders produced by injection molding were investigated by German [61]. The main drawback of this method was that it required rounded particles, for improved packing and sintered density.

Sharon *et al.* [62] investigated the corrosion behavior of austenitic stainless steel by adding nickel-based additives. The corrosion resistance of the sintered stainless steel increased substantially by adding 1-5% of nickel based brazing powder. This was attributed to the reduction of open interconnected porosity due to the formation of transient liquid phase.

German *et al.* [63,64] studied the effect of boron addition on austenitic stainless steel. By addition of 0.3wt% boron near theoretical density obtained in austenitic stainless steel when sintering was carried at SLPS region.

Danninger *et al.* [52] showed the effect of secondary pore on mechanical properties in Fe-Cu system. The larger pores lower the tensile strength, elongation and especially impact strength.

Christian *et al.* [65] studied the fatigue endurance strength with porosity, average pore curvature and separation distance between pores in Fe-Cu-C system. Baken *et al.* [66] showed the effect of NiB and boron on sintering characteristic of injection moulded 316L powder using water soluble binder system. This binder system provided mixture stability, excellent mouldability, and reasonably faster water leaching and thermal de-binding rate.

Velasco *et al.* [67] studied the effect of copper and bronze infiltration on mechanical and corrosion resistance properties of austenitic stainless steel. Infiltration improved the sintered density and mechanical properties. Bronze enhanced the corrosion resistance in HCl and H₂SO₄. But copper or bronze infiltration reduced the corrosion resistance in HNO₃.

Puscas *et al.* [68] studied the sintering transformation in mixture of austenitic and ferritic stainless steel powders. The linear shrinkage was influenced by the amount of ferritic powder. Moreover, during sintering nickel diffused into the ferrite grain causing austenite destabilization and the formation of a mixed constituent

Liu *et al.* [69] measured the capillary pressure in liquid phase sintering. During liquid phase sintering the capillary force arises from the curvature of the liquid meniscus between neighboring particles. The capillary force is oriented isotropically and provides a compressive strength normal to the neck section between neighboring solid particles.

Anklekar *et al.* [70] studied the microwave sintering and mechanical properties of P/M copper steel. Microwave resulted in higher sintered density, higher Rockwell hardness and higher strength compare to the conventional sintering. It is because of small rounded uniform distribution of pores compare to the conventional sintering.

Rosso *et al.* [71] showed the effect of boron on microstructure and mechanical properties of P/M sintered and nitrited steel. Molinari and Rosso [72,73] studied the density and microstructure of duplex stainless steel produced by mixture of austenitic and ferritic stainless steel powders. Sintering of mixture of austenitic and ferritic stainless steel powders give higher sintered density than the pure austenitic or ferritic powders. But microstructure contaminated by the sigma phase. Boron addition enhances the densification and influences the sigma phase.

Liu *et al.* [74] studied the boron enhanced sintering of Mo-steel. This study examined boron mainly distributed as liquid network constituents surrounded the steel grains during sintering. If Mo is distributed homogeneously inside the grain then boron remains as a solid solution and did not form a brittle boride phase.

German *et al.* [75] showed the liquid phase sintering of Fe-C alloys with boron addition. The carbide forming element Mo was added to protect boron from reaction with carbon ($>0.4\%$). Boron activates the sintering process of Fe-C powder mixture by forming a eutectic liquid phase which promotes densification. Near full density was achieved with the boron addition of 0.3 wt. %.

Kuroki *et al.* [76] studied solution reprecipitation mechanism in Fe-Cu-C system during liquid phase sintering. The driving force for sintering in this system was induced by the gap in carbon concentration between Fe-particles, and fromed differences in surface curvature. A semi-permeable layer of liquid Cu forms which prevents carbon diffusion but allows Fe to be transported between particles, there by enhancing sintering.

Marchetti *et al.* [77] studied the sintering mechanism of boron alloyed AISI 316L stainless steel. Boron strongly enhanced sintering by liquid phase formation only when the process was carried out in pure hydrogen at a temperature higher than

1200°C In this condition a eutectic reaction between austenite and a complex boride of the type $(\text{Fe,Cr,Mo})_2\text{B}$ occurred favoring densification through liquid phase sintering

The particulate particles such as Al_2O_3 , Y_2O_3 , ZrO_2 , ThO_2 etc. added to the stainless steel in order to improve the strength which is called Oxide Dispersed Strengthening (ODS). Extensive research was carried out on the effect of Y_2O_3 on the sintering behavior and corrosion resistance of 316L stainless steel by Upadhyaya *et al.* [78-80] Solid state sintering was carried out on 316L austenitic powders and the effect of Y_2O_3 was studied by varying the composition from 0-8%. Maximum Tensile strength was obtained for samples containing 4 volume % Y_2O_3 . But the oxidation resistance degraded

The effect of Al_2O_3 oxide dispersoid on the sintering behavior and properties of 434L ferritic stainless steel was investigated in detail by Mukherjee and Upadhyaya [81-84]. Al_2O_3 was added from 0-8 volume % in 434L stainless steel samples and subjected to solid state sintering. It was reported that the composites having 4-6 volume % of Al_2O_3 had higher mechanical properties.

Chapter 3

SCOPE OF THE PRESENT WORK

The two main types of P/M stainless steel that are used for their wide range of applications are the austenitic stainless steel and ferritic stainless steel. Hence these two types of stainless steel were selected as the materials for the present work. Austenitic stainless steel is chosen mainly for their better corrosion resistance and mechanical properties. The ferritic stainless steel is selected in area where magnetic properties and economy comes as the basic need of the product.

From effective and economic point of view, it is worthwhile to select, before starting experiments, alloy composition, sintering parameters such as sintering temperature, sintering time, sintering atmosphere, etc. Extensive research has been carried out on P/M stainless steel regarding their sintered density, mechanical properties and corrosion resistance properties [60-85]. Solid state sintering was the method that was commonly reported as the sintering technique in most of the previous research work on P/M stainless steel. In the present work, a novel method for sintering of prealloyed powders called supersolidus liquid phase sintering (SLPS) has been used. In this technique the prealloyed powders of stainless steel are sintered between the solidus and liquidus temperature, so that the homogeneous liquid phase is formed within the particles thereby producing higher densification.

Regarding additives in most of the cases boron, copper, alumina, yttria etc. was added. Boron was mostly added in austenitic or duplex types of stainless steel. No work has been done on the effect boron on ferritic stainless steel. Copper was mostly used in pure iron or in Fe-C system. Very little work has been done in stainless steel with copper addition.

In the present work boron and copper was chosen as sintering additives which formed liquid at sintering temperature. Here boron was added in the form of boride because boron readily forms volatile oxide which causes porosity. Yttria alumina Garnet (YAG) was also chosen as sintering aid. It helps to increase strength by restrict grain growth at higher sintering temperature and enhanced the mechanical properties. Actually in this study it is aimed to observe the synergistic effect of these additives in densification and mechanical properties of the stainless steel. Microstructural evolution has been studied as a function of sintering temperature and with additives. Optical and SEM micrographs have been taken to observe the phase present in the microstructure and the distribution of pores in the matrix. Studies of mechanical properties have been done by measuring hardness and tensile properties.

Chapter 4

EXPERIMENTAL PROCEDURE

4.1 Raw Materials

4.1.1 Stainless Steel Powders

Stainless steel powders that were used in the present work were 434L Ferritic grade and 316L Austenitic grade. The gas atomized stainless steel powders were supplied by AMETEK Specialty Metal Products Divisions, USA. The chemical compositions and characteristics of the as received powder are given below

4.1.1.1 Ferritic Stainless Steel Powder (434L)

Chemical Composition

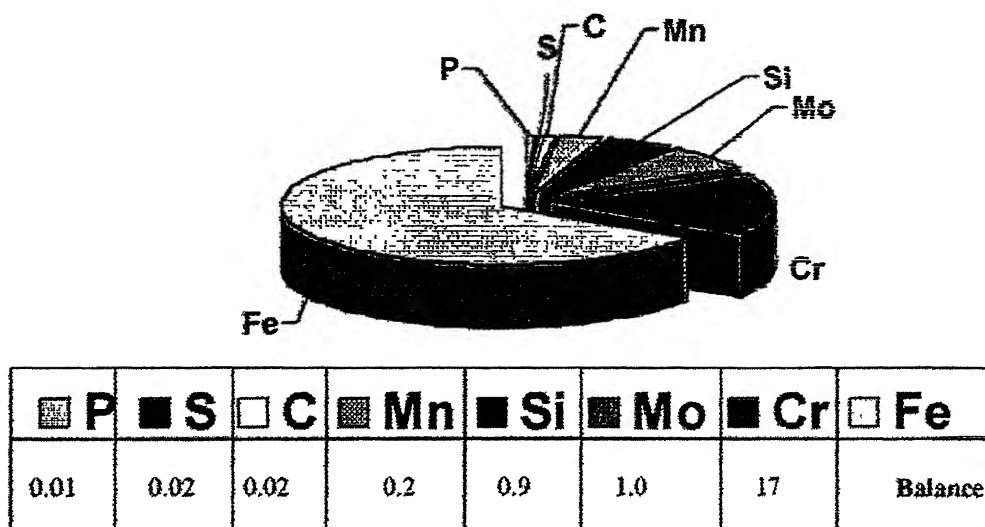


Figure 4.1 Chemical composition of the 434L powder.

Physical Properties

Theoretical density. 7.86 g/cm^3

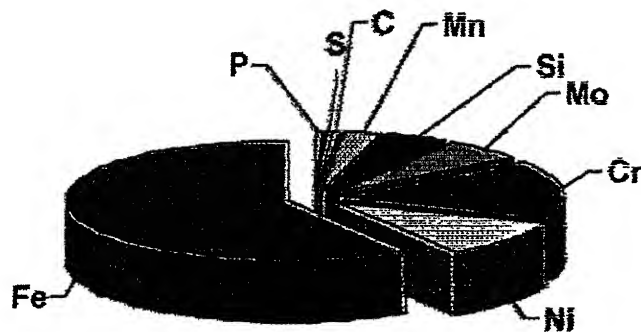
Apparent density . 2.6 g/cm^3

Flow rate . 28 s/50g

Powder compressibility (at 50 ton/in^2):

Green density : 6.36 g/cm^3

Green strength : 1170 psi

4.1.1.2 Austenitic Stainless Steel Powder (316L)**Chemical composition**










 P	 S	 C	 Mn	 Si	 Mo	 Cr	 Ni	 Fe
0.01	0.02	0.02	0.2	0.9	1.0	17	12	Balance

Figure 4.2 Chemical composition of the 316L powder.

Physical Properties

Theoretical density. 8.06 g/cm³

Apparent density . 2.72 g/cm³

Flow rate . 28 s/50g

Powder compressibility (at 50 ton/in²):

Green density 6.7 g/cm³

Green strength : 1500 psi

4.1.2 Copper Powder

The copper powder (Grade: 635) was supplied by ACuPowder International (Union, NJ, USA). The Cu powder was prepared by chemical reduction process with the average size of 13 μm in as received condition.

4.1.3 Iron Boride Powder (FeB)

This powder was supplied by F.W. Winter Inc., Camden, NJ, USA. The prismatic shape powder was produced by chemical synthesis process.

4.1.4 Nickel Boride Powder (NiB)

This powder was supplied by F.W. Winter Inc., Camden, NJ, USA. The prismatic shape powder was also produced by chemical synthesis process.

4.1.5 Yttria Alumina Garnet (YAG) Powder

This powder was supplied by Treibacher Auernmet Produktionsges, Austria. It contains two types of aluminium yttrium oxides, $\text{Al}_5\text{Y}_3\text{O}_{12}$ and AlYO_3 . Table 4.1 shows the chemical composition of YAG powder.

4.2 Powder Characterization

The as received powders were characterized for their size distribution and morphology. For the characterization techniques only a small part of the samples were utilized and assumed as representatives of the bulk samples.

4.2.1 Particle Size and Size Distribution

Particle size determination was carried out using a laser-scattering size analyzer (model: Economy, Laser Klasse 1; supplier: Fritsch, Germany). Low angle Fraunhofer light scattering by monochromatic laser and dispersed particles were used in this case. Particles were suspended in a moving fluid. The suspension was made using 1 to 3 g of powder in approximately 60 ml of distilled water with 10% sodium metaphosphate. The particles are passed through a laser beam in a circulating water stream. The light is scattered after the interaction with the particles, and the intensity is measured by strategically placed detectors. Particle size affects both the intensity and angular extent of scattering. With coherent light the angle of scattering varies inversely with the particle diameter. The scattering depends on the refractive index of the particle in the suspending medium, the wave length of light, and the particle size

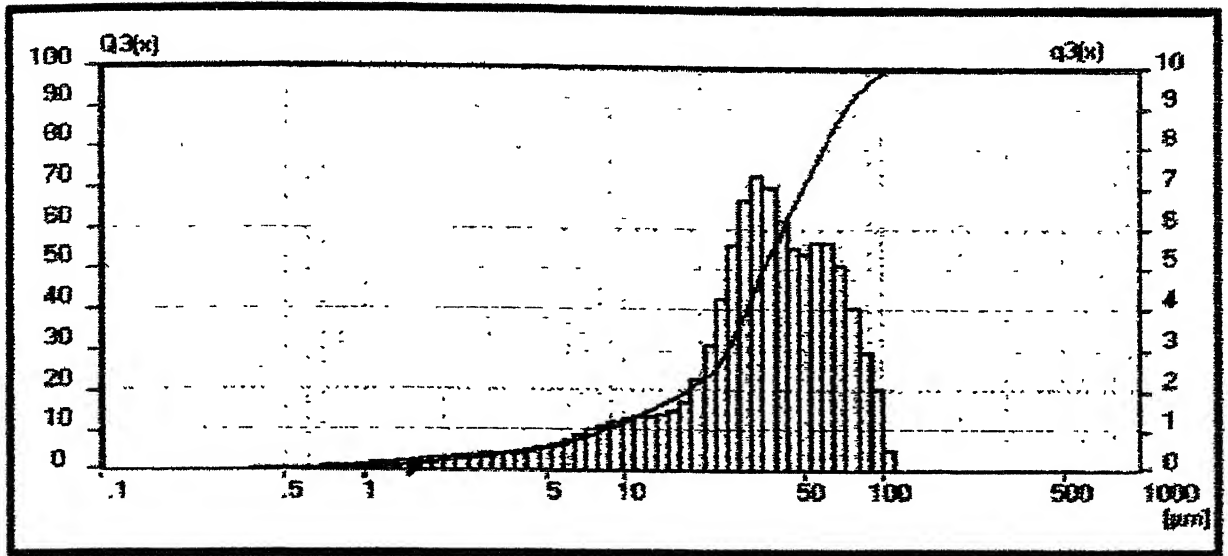


Figure 4.3 Histogram plot of the particle size analysis of 434L powder

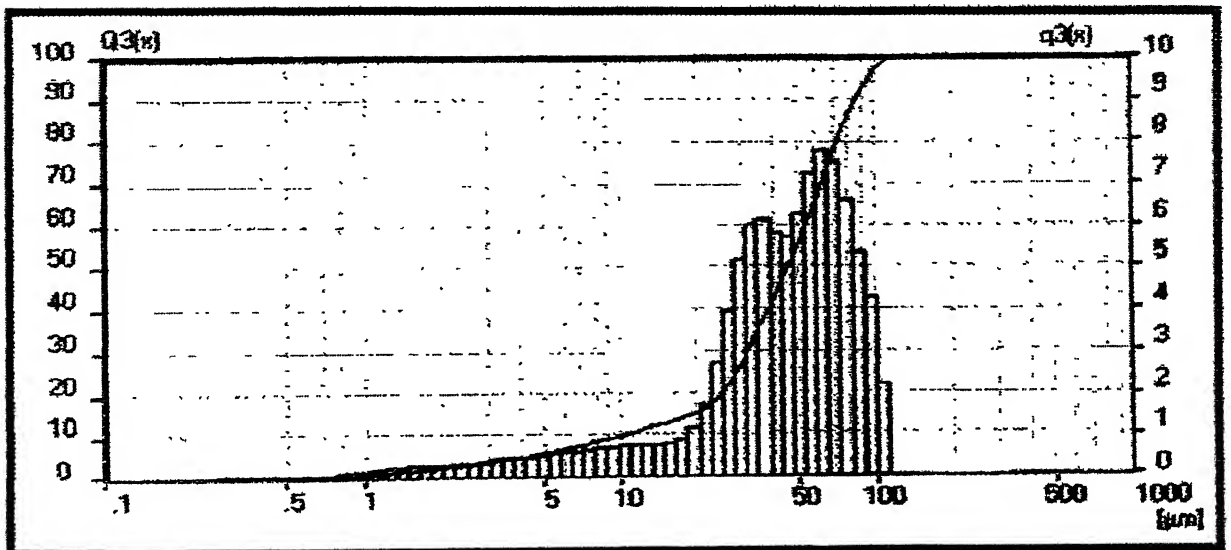


Figure 4.4 Histogram plot of the particle size analysis of 316L powder.

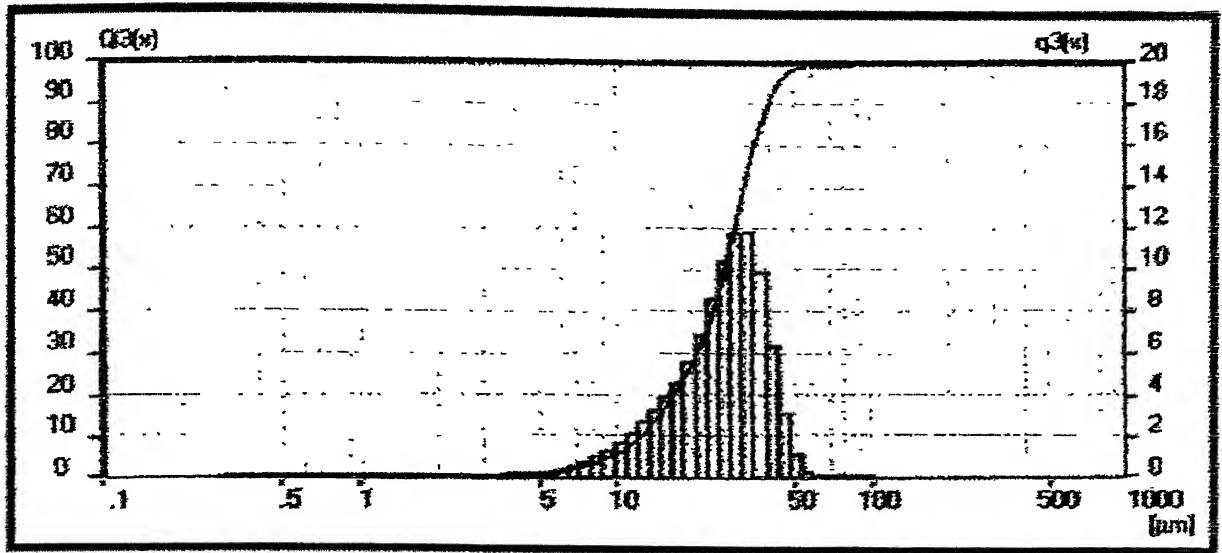


Figure 4.5 Histogram plot of the particle size analysis of Cu powder.

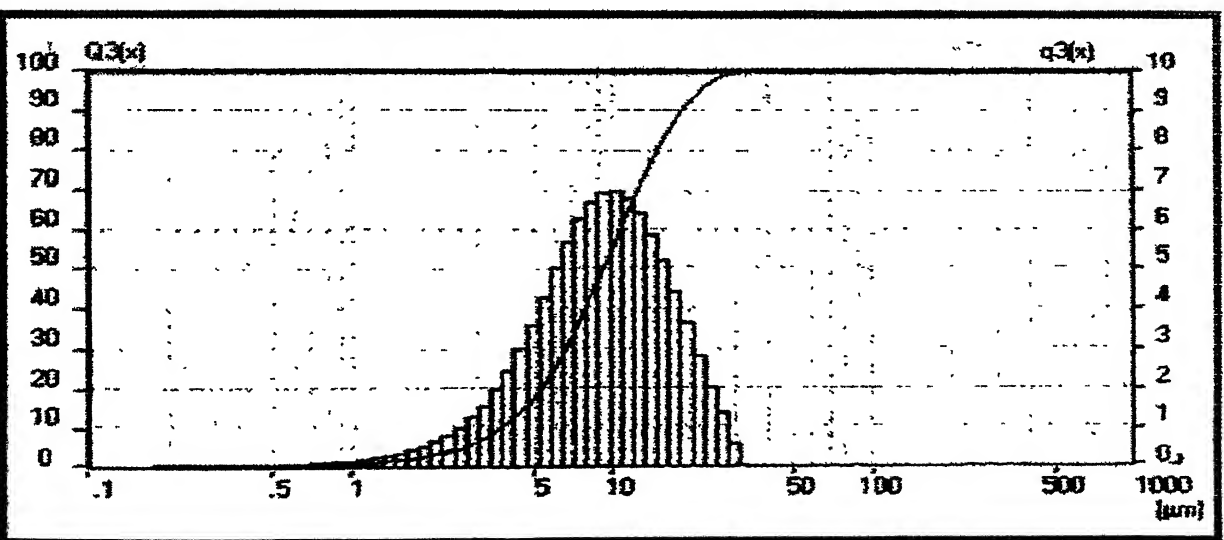


Figure 4.6 Histogram plot of the particle size analysis of FeB powder.

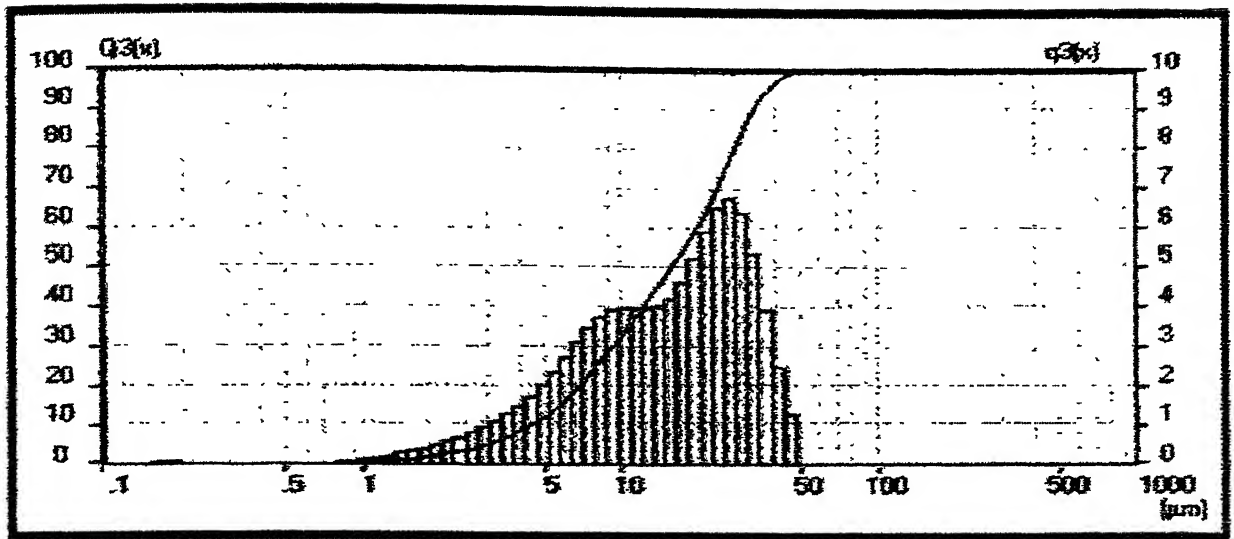


Figure 4.7 Histogram plot of the particle size analysis of NiB powder.

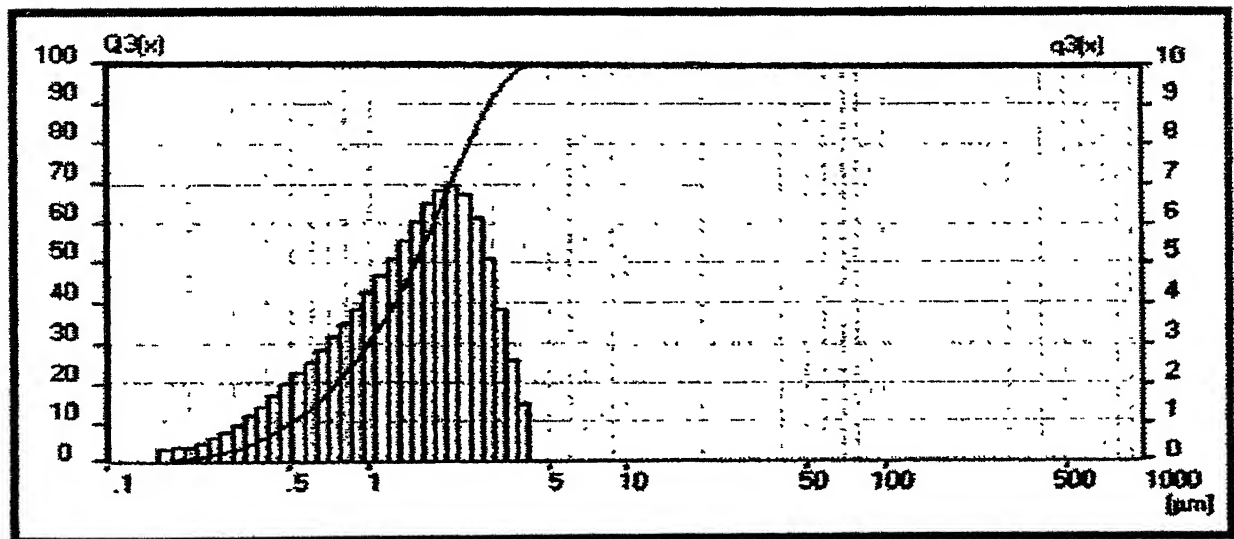


Figure 4.8 Histogram plot of the particle size analysis of YAG powder.

Figure 4.3 and 4.4 show the monomodal particle distribution of 434L and 316L stainless steel powder, respectively. Maximum number of particles was in the range of 35-50 μm size in both the cases. But the company specification is 16-20 μm . Discrepancy occurred because of the particles were agglomerated in the suspension medium. The particle size distribution plot for copper is plotted in Figure 4.5. It clearly shows a monomodal distribution of particles lies in the range of 22-30 μm . The size distribution plot of FeB and NiB powders are shown in Figure 4.6 and 4.7, respectively. The plots show monomodal size distribution of particles having size ranges are 7-11 μm for FeB and 12-20 μm for NiB. Yttria alumina garnet shows a monomodal size distribution of particles which has been shown in Figure 4.8. The particles size range is from 1-2 μm . Table 4.2 summarizes the particle size distribution of the as-received powders.

4.2.2 Particle Shape

The particle shape of the powders was obtained using JEOL, JSM – 840 A, Scanning Electron Microscope, in the secondary electron (SE) mode. The SEM permitted far greater viewing magnification than optical equipment. The Figures 4.9 and 4.10 show the SEM micrographs of 434L and 316L stainless steel powders, respectively. From the figures it is pretty clear that particle shape is spherical for both the cases. The chemically reduced copper powder has irregular morphology and highly agglomerated. This feature is captured in Figure 4.11. Figures 4.12 and 4.13 show the SEM micrographs of prismatic shaped FeB and NiB powders, respectively. Yttria alumina garnet particles are shown in Figure 4.14. It shows irregular morphology of the YAG particles.

Table 4.1 Chemical composition of YAG powder.

Element	Amount (%)
Y	45.05
Al	22.5
Fe	0.014
Si	0.014
Ti	< 0.01
C	0.08

Table 4.2 Characteristics of the as received powders

Powder	D ₁₀ (μm)	D ₅₀ (μm)	D ₉₀ (μm)
434L	8.46	35.25	73.13
316L	10.25	45.96	85.16
Cu	12.51	26.92	39.87
FeB	3.77	9.25	18.75
NiB	4.51	16.00	33.52
YAG	0.50	1.51	2.93

4.3 Premix Preparation

The stainless steel powders (434L and 316L), yttria alumina garnet (YAG) and elemental powder such as copper (Cu), iron boride (FeB), and nickel boride (NiB) were weighted in electronic balance (supplier: Mettler, AE200, USA) having 0.0001 accuracy. The balance was calibrated using a series of standard weights. After weighing the individual powders were taken into one litre capacity glass jar and mixed in a Tubula mixer (type: - T2C Nr.921266, supplier: Bachofen, AG, Germany) for half an hour. Mixing ensures complete homogenization in the powder mixture. To prevent segregation proper care was taken by avoiding the shaking of the mixed powder containers.

After mixing of the powders of desired compositions, the density of the mixed powder were determined by the inverse rule of mixture. The inverse rule of mixing can be written as:

$$\frac{w}{\rho_{th}} = \frac{w_1}{\rho_1} + \frac{w_2}{\rho_2} \quad (4.1)$$

where,

w_1 and w_2 are the weight fraction of the powders

ρ_1 and ρ_2 are the densities of the powders

ρ_{th} is the theoretical density of the powder mixture.

As an example, for 434L-2 Cu composition,

$$\frac{1}{\rho_{th}} = \frac{0.02}{8.96} + \frac{0.98}{7.88} \quad (4.2)$$

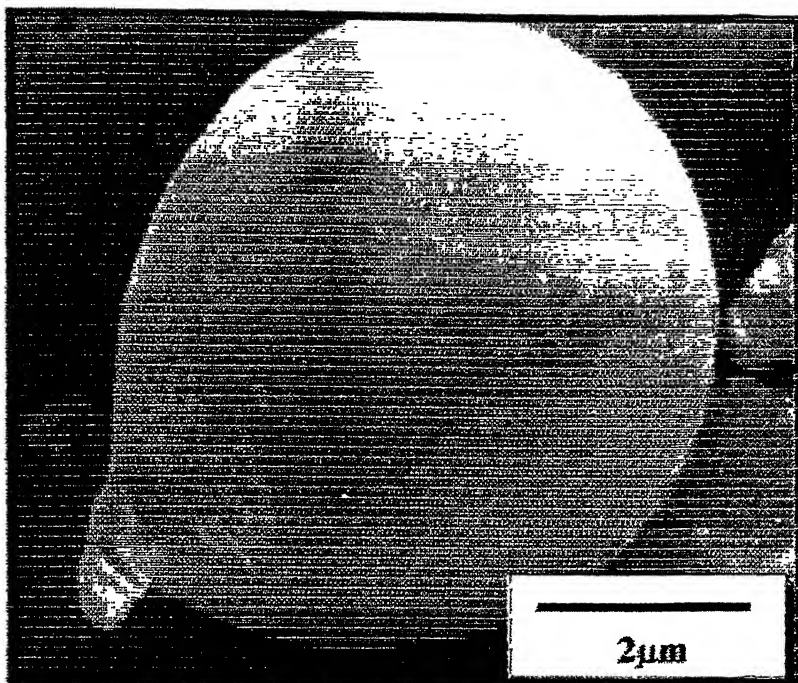


Figure 4.9 SEM micrograph of 434L powder.

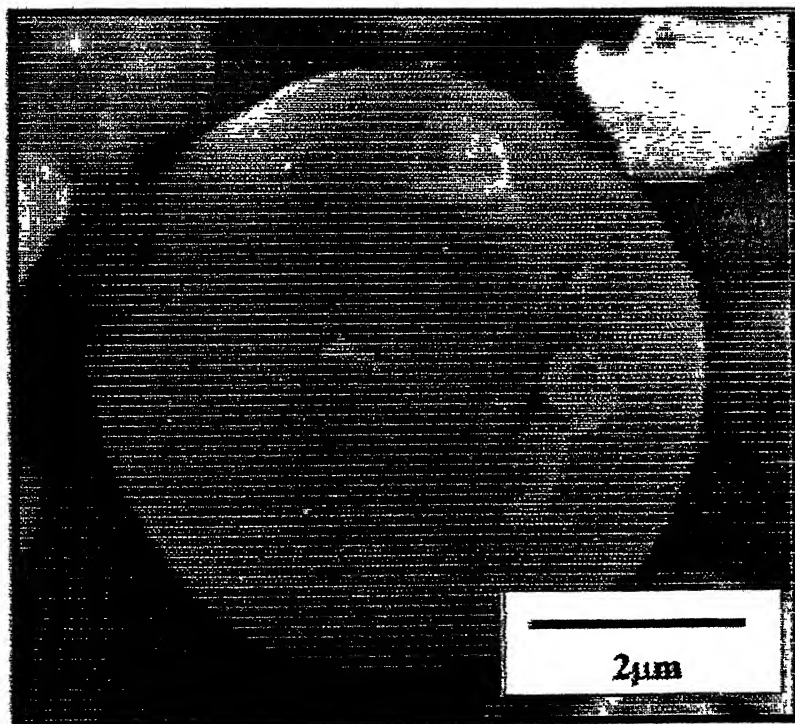


Figure 4.10 SEM micrograph of 316L powder.

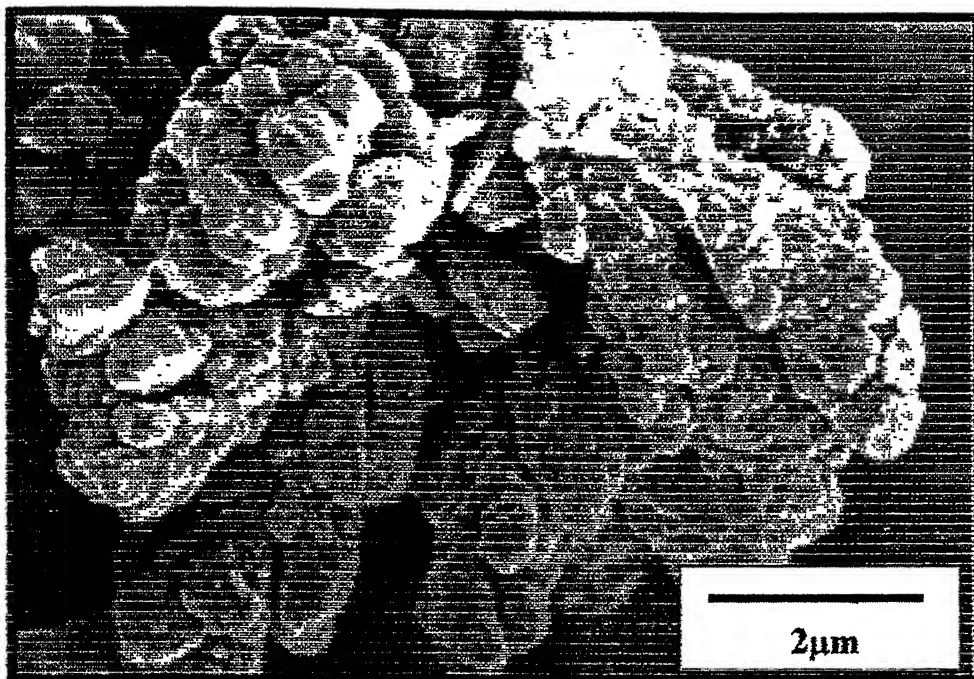


Figure 4.11 SEM micrograph of Copper powder.



Figure 4.12 SEM micrograph of FeB powder.

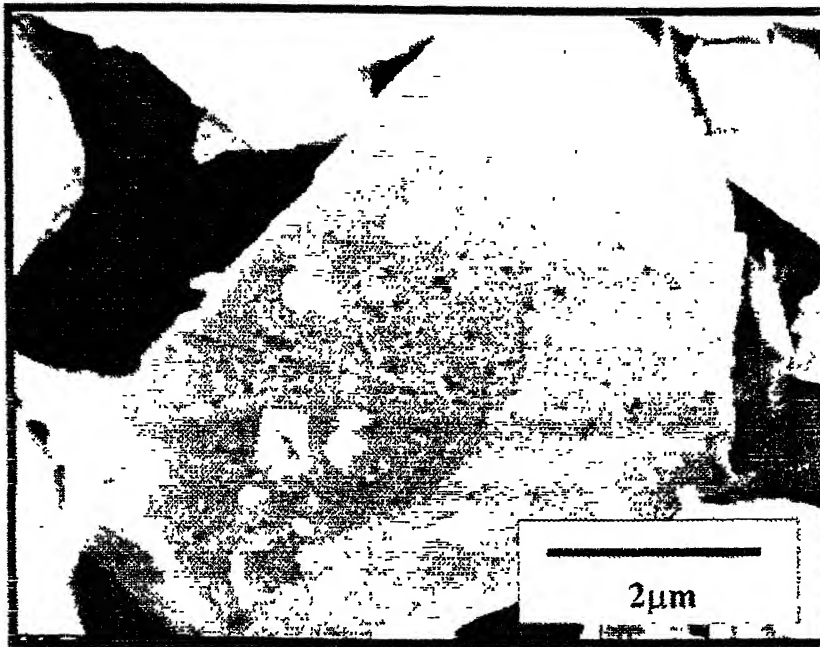


Figure 4.13 SEM micrograph of NiB powder.

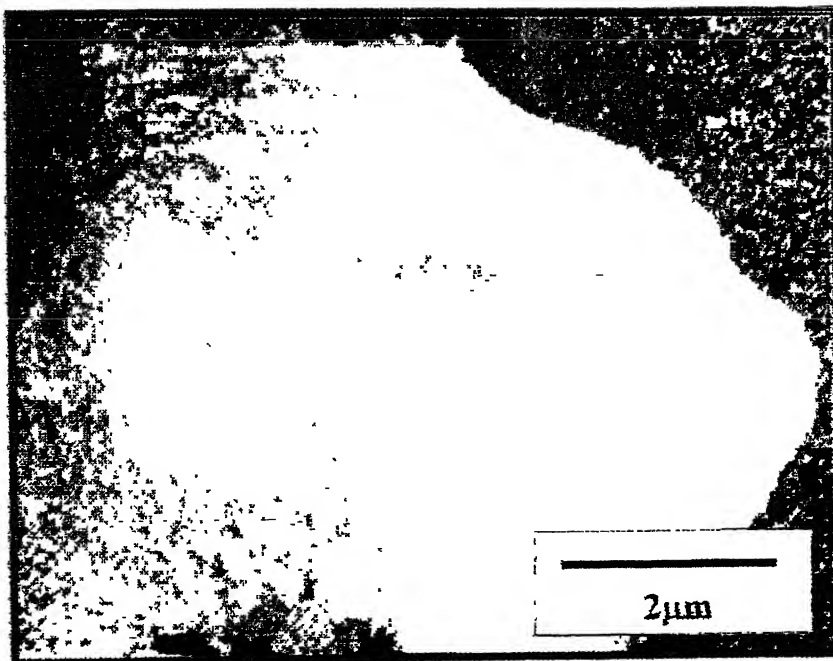


Figure 4.14 SEM micrograph of YAG powder.

Figures 4.15 and 4.16 show the different premix compositions used in the present work for 434L and 316L, respectively. Table 4.3 and 4.4 represent the corresponding theoretical density.

4.4 Compaction

Cylindrical green compacts of 8 mm diameter and approximately 4 to 6 mm height were made from premix powders using a CTM-50 (capacity 50 Ton), compression testing machine supplied by Fuel Instruments & Engineering Private Limited, Ichalkaransi, Maharashtra, India. The die made of high chromium high carbon steel was cleaned with acetone and was lubricated with zinc-stearate prior to each powder compaction. Lubrication facilitates compaction by minimizing wear between powders and die wall and subsequently removal of the compacted samples. In this study, 600 MPa optimum pressure condition was chosen for compaction [85]

4.5 Sintering

Sintering was carried out in a SiC-heated horizontal tubular furnace (rating 1.5 kVA) supplied by Bysakh & Company, Kolkata. The furnace tube was made up of doubly recrystallized alumina. The inner diameter of the tube was 38 mm and length 980 mm. Sintering was done in commercially pure hydrogen (dew point: -35°C) atmosphere, which provided reducing atmosphere for the samples and prevents the samples from oxidation. The flow rate of hydrogen was maintained at 1 liter/min. The furnace has a heating zone of approximately 105 mm in the temperature range of $1100^{\circ}\text{C} - 1500^{\circ}\text{C}$ with an accuracy of $\pm 5^{\circ}\text{C}$. Figure 4.17 shows a schematic view of the sintering furnace.

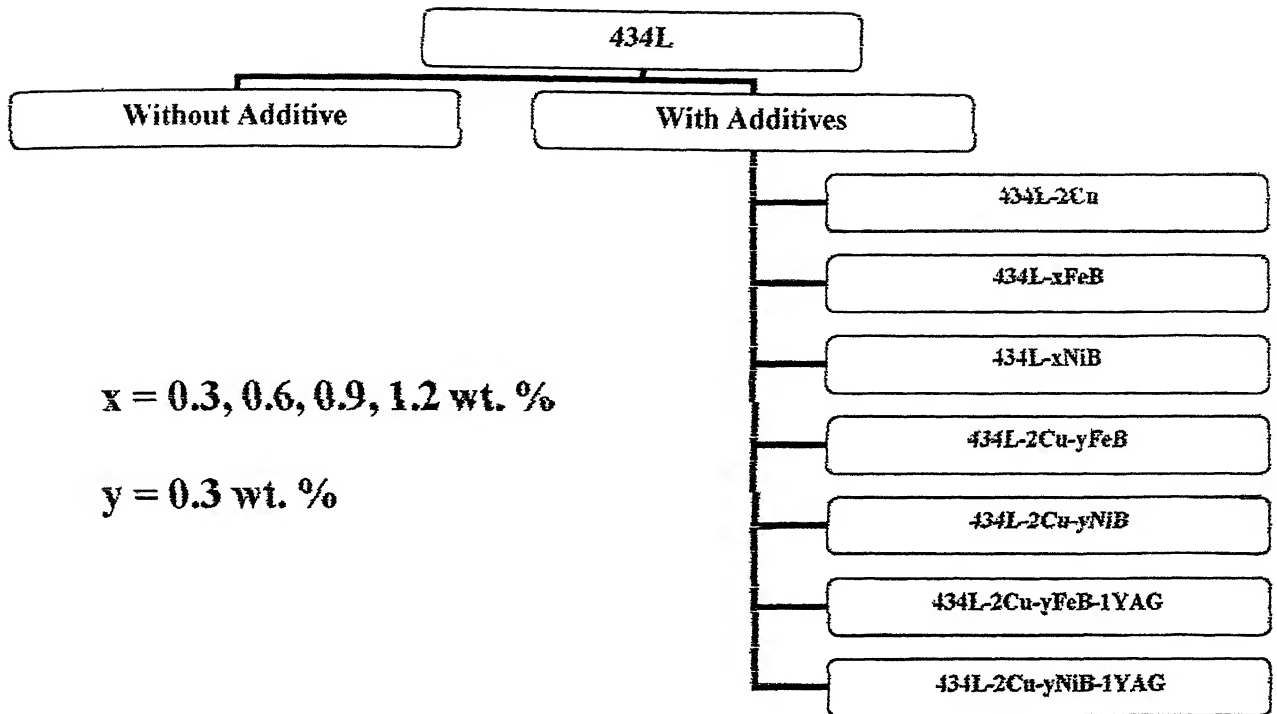


Figure 4.15 Composition of investigated materials (434L with additives).

Table 4.3 Theoretical densities of investigated materials (434L and with additives).

Composition	Theoretical Density (ρ_{th})
434L	7.86
434L-2Cu	7.88
434L-0.3FeB	7.86
434L-0.6FeB	7.86
434L-0.9FeB	7.85
434L-1.2FeB	7.85
434L-0.3NiB	7.86
434L-0.6NiB	7.85
434L-0.9NiB	7.85
434L-1.2NiB	7.85
434L-2Cu-0.3FeB	7.88
434L-2Cu-0.3NiB	7.88
434L-2Cu-0.3FeB-1YAG	7.83
434L-2Cu-0.3NiB-1YAG	7.83

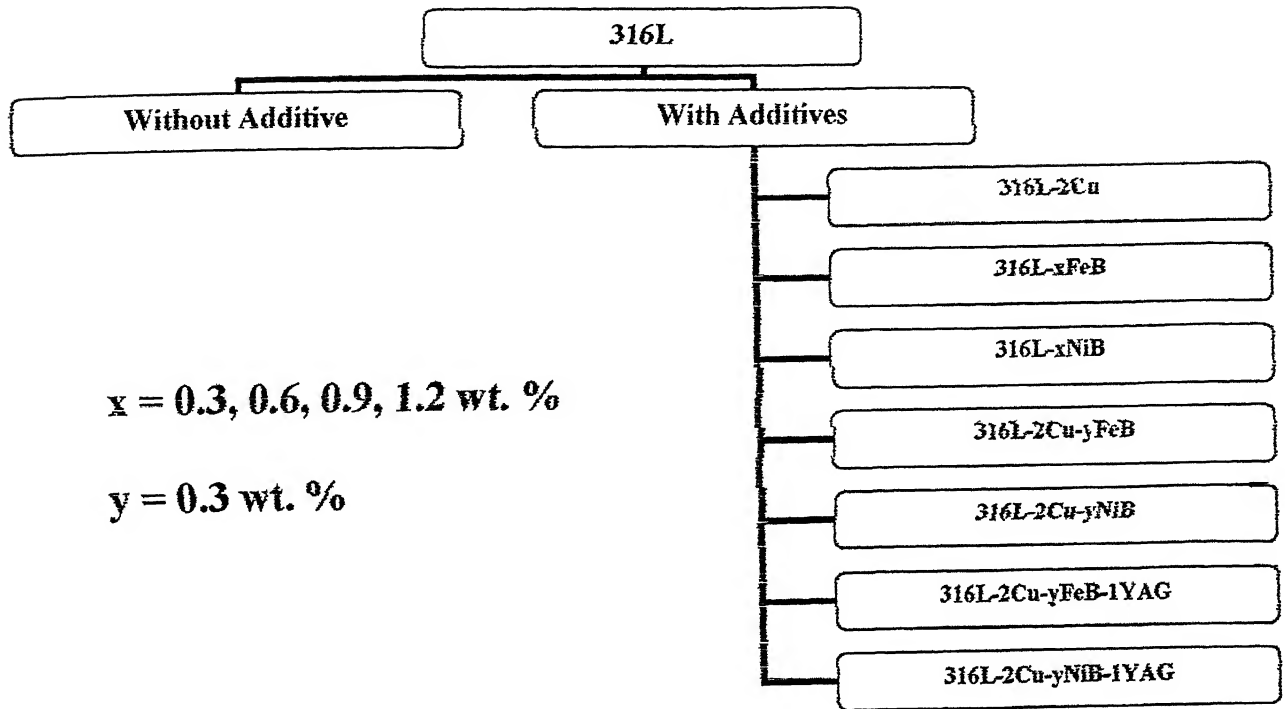


Figure 4.16 Composition of investigated materials (316L with additives).

Table 4.4 Theoretical densities of investigated materials (316L and with additives)

Composition	Theoretical Density (ρ_{th})
316L	8.06
316L-2Cu	8.08
316L-0.3FeB	8.06
316L-0.6FeB	8.05
316L-0.9FeB	8.05
316L-1.2FeB	8.05
316L-0.3NiB	8.06
316L-0.6NiB	8.05
316L-0.9NiB	8.05
316L-1.2NiB	8.05
316L-2Cu-0.3FeB	8.07
316L-2Cu-0.3NiB	8.07
316L-0.3FeB-1YAG	8.00
316L-0.3NiB-1YAG	8.00

In the present study two different temperatures were selected for sintering. The temperatures were 1250 and 1400°C. Green compacts were placed over an alumina slide and transferred in the heating zone of the tubular furnace. Alumina has got higher melting point than our maximum sintering temperature and there is no inter-diffusion of alumina with stainless steel. So, there should not be any sticking problem of the samples with the alumina slide. Both ends of tubular furnace were sealed with SILASTIC (RTV 700) sealant to prevent any leakage. Heating rates were same for all the sintering operations (5°C/min). The samples were heated to the final sintering temperature after intermittent holding at 1000°C for an hour. Holding time was 60 minutes at final sintering temperature for each case. Automatic temperature controller was used to control the temperature within $\pm 5^\circ\text{C}$. In all cases cooling was done in same hydrogen atmosphere, i.e. furnace cooling, at an average rate of $2-3^\circ\text{C}/\text{min}$.

4.6 Densification Behavior

4.6.1 Density and Densification Parameter

Densities of the green cylindrical compacts were calculated by the dimension measurement method whereas the densities of the sintered samples were calculated by both dimension measurement method and Archimedes principle. Densification parameter was also a way to determine the amount of densification occurred after sintering. Densification parameter (ψ) was expressed as follows

$$SD - GD$$

where SD is the sintered density, GD is the green density, and TD is the theoretical density. Positive value of ψ indicates densification and negative value indicates swelling or distortion taken place after sintering.

4.6.2 Axial and Radial Shrinkage

Linear and axial dimensions of the sintered samples were measured using slide calipers and screw gauge of accuracy ± 0.01 mm. Average of five measurements of each dimension is reported. The formula used for calculations are as follows,

$$\delta h = \left(1 - \frac{h_s}{h_g} \right) \times 100\% \quad (4.4)$$

$$\delta r = \left(1 - \frac{r_s}{r_g} \right) \times 100\% \quad (4.5)$$

Where,

$h_g, r_g \rightarrow$ height and radius of the green compact

$h_s, r_s \rightarrow$ height and radius of the sintered compact.

$\delta h \rightarrow$ % linear shrinkage in height

$\delta r \rightarrow$ % radial shrinkage

4.7 X-ray Diffraction Analysis

X-ray diffraction studies on the powders (both premixed and elemental), green compacts and sintered compacts were carried out on Rich Seifert & Co., Germany, ISO Debyeflex -2002 diffractometer. Powders were kept in a square holder having

very small thickness. Some methyl alcohol was added on the powders so that they would be properly adhered during the diffraction study. Sintered samples after paper grinding and wheel polishing were kept in the holder for analysis. The various parameters during the experiment are given below,

Target (Radiation) \rightarrow Cu (K_{α})

Wavelength, $\lambda \rightarrow 1.542 \times 10^{-10}$ m

Scanning Speed $\rightarrow 3^{\circ}\text{C}/\text{min}$, (in 2θ)

Counts/min $\rightarrow 50,000$

Time Constant $\rightarrow 3$ s

Amperage $\rightarrow 20$ mA

Voltage $\rightarrow 30$ kV

The X-ray machine is connected with computer. While scanning the sample, computer saved all the data (intensity and angle). From these data the intensity vs angle graphs were plotted. Indexing of X-ray diffraction patterns were carried out by matching peak coordinate value with the standard values from Joint Commission for Powder Diffraction Standard (JCPDS) cards (ed. 1996).

4.8 Microstructural Studies

4.8.1 Optical Microscopy

Sintered samples were cold mounted because the sample height was not sufficient for holding. The compacts were wet polished on the Lunn Major Unit made in Struers, Denmark make 220, 320, 500 and 1000 grit silicon carbide emery papers followed by fine wheel polishing with suspended $0.03 \mu\text{m}$ size alumina in distilled

The common etchants that are used for stainless steel are specified in Table 4.5

and 4.6. In the present work etchant-I for ferritic and etchant-II for austenitic stainless steel were used. Etching was carried out for 20-30 seconds by swabbing method. The microstructure was examined using Leitz Labor Lux 12MES Image Analyzer.

4.8.2 Scanning Electron Microscopy

The microstructures of selected samples were also observed under JEOL, JSM – 840 A, Scanning Electron Microscope. Operating voltage was 10 – 15 kV and probe current ranged from 1×10^{-10} to 5×10^{-6} A in secondary electron imaging mode. The samples were deeply etched for SEM study to reveal the finer details.

4.9 Study of Mechanical Properties

4.9.1 Hardness

4.9.1.1 Vickers Bulk-hardness

Vickers Bulk-hardness of the polished specimens was measured by Leco V-100-C1, Hardness Tester, manufactured by Akashi Corporation, Japan. The load of 2 kg and indentation time of 15 s was maintained for each sample. The diagonal lengths of the impressions were measured and the hardness was obtained directly in HV scale on the monitor.

4.9.1.2 Vickers Micro-hardness

Vickers micro-hardness had been taken at a load of 5 g on polished and etched samples in a micro-hardness tester, manufactured by Leitz, Germany. The indentation

time of 15 s was maintained. The diagonal lengths of the impressions were measured and the hardness was obtained from the standard table.

4.9.2 Study of Tensile Properties

Tensile test was carried out on samples sintered at 1400°C. Tensile test were carried out in Instron Universal Testing Machine (Model – 1195, Capacity – 10 Ton). The tensile die is made of high chromium high carbon steel. It was cleaned with acetone and lubricated with zinc-stearate prior to each compaction. Lubrication facilitates compaction by minimizing wear between powders and die wall and subsequent helps to remove the compacted samples. Here also 600 MPa pressure was given for compaction. Figure 4.18 shows a standard powder metallurgical tensile sample of 1 sq. inch cross sectional area, 90 mm long, 6 mm wide and 5 to 6 mm of thickness [14]

Table 4.5 Etchants for Ferritic Stainless Steel.

Etchant-I		Etchant-II	
CuCl ₂	5 g	HCl	: 10 ml
HCl	: 100 ml	HNO ₃	: 3 ml
C ₂ H ₅ OH	: 100 ml	C ₂ H ₅ OH	: 100 ml
Distilled Water	: 100 ml		

Table 4.6 Etchants for Austenitic Stainless Steel.

Etchant-III	
CuSO ₄ .5H ₂ O	: 12 g
HCl (conc.)	: 60 ml
Distilled Water	: 60 ml

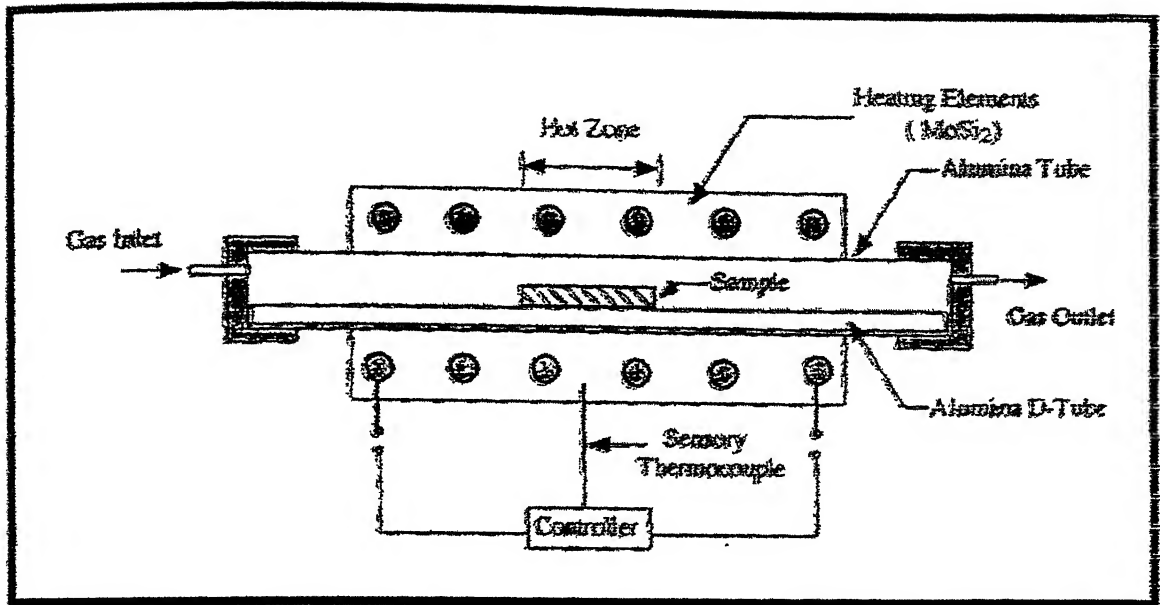


Figure 4.17 Schematic diagram of sintering furnace.

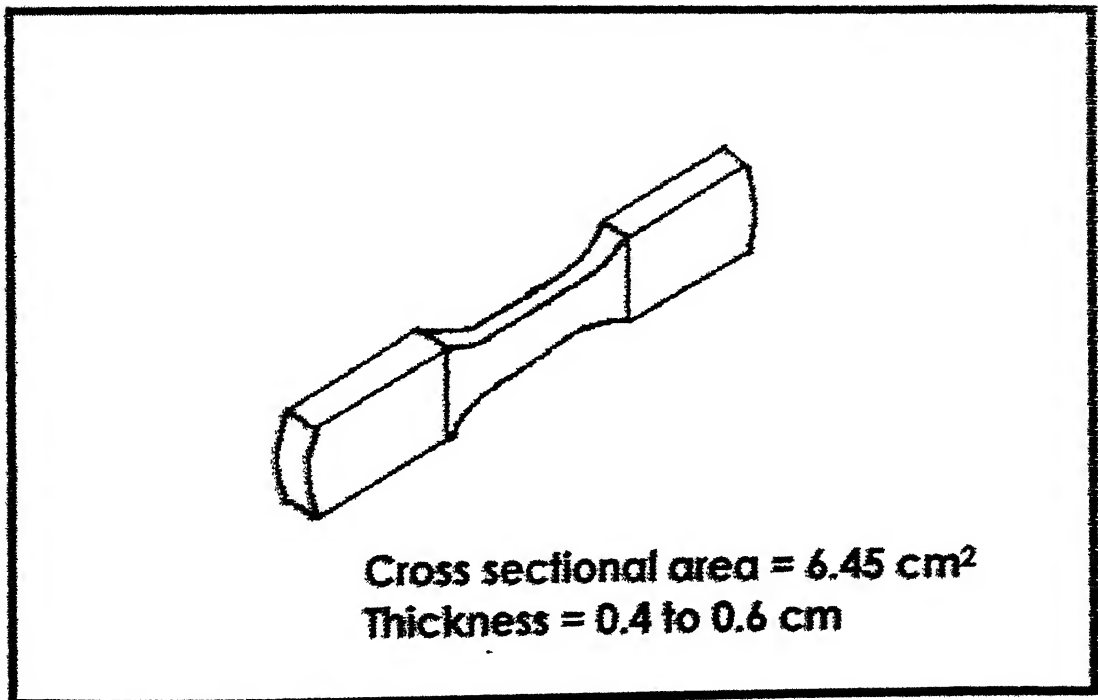


Figure 4.18 A Standard powder metallurgical tensile sample.

Chapter 5

EXPERIMENTAL RESULTS

5.1 Densification Behaviour

The densification behaviour of the P/M stainless steel samples are described using the sintered density, densification parameter, and change in axial and radial dimensions.

5.1.1 Density and Densification Parameter

Ferritic Stainless Steel (434L)

The experimental data before and after sintering for all the 434L samples with additives used in the present study are given in Appendices I and II. In this case sintered density increased with increasing sintering temperature. The variation of sintered density of selected composition was plotted in Figure 5.1. These compositions were chosen because it showed maximum densification. For the remaining samples the density was either remains constant or less than the selected composition. Figure 5.1 shows the variation of sintered density at two different temperatures, 1250° and 1400°C of 434L for different additives composition. It clearly indicates that density is not only a function of temperature, but it also depends on of additives. The sintered density increased from 85 to 91% theoretical for pure 434L with increase in sintering temperature from 1250 to 1400°C. But the remarkable increase of sintered density occurred when sintering was done at 1400°C along with copper and borides additives. For 2 wt. % Copper, 0.3 wt. % FeB and 2 wt. % Copper, 0.3 wt. % NiB the sintered density were obtained as high as 94 %theoretical. To enhance the mechanical properties 1 wt. % yttria alumina garnet (YAG) was added. It

was also helpful to increase the sintered density. In this case this value reached up to 95 %theoretical as shown in Figure 5.1

Densification parameter is also very important to understand the densification behaviour of sample because it gives a relative measurement of the densification of compacts with density being normalised with respect to the green density. The variations of densification parameter with temperature of all 434L samples with additives are given in Appendices I and II. The variation densification parameter of selected compositions for 434L samples with additives was plotted in Figure 5.2. From the plots it is clearly evident that the samples sintered at 1400°C were having better densification parameter than samples sintered at 1250°C. Here also it is not only depends on sintering temperature but also depend on additives. As shown in Figure 5.2 the densification parameter of pure 434L at 1250°C sintering temperature was 0.40, it increased to 0.62 when sintering was done at 1400°C. But the maximum value were obtained with 2 wt % copper along with 0.3 wt. % FeB or NiB additives. It was as high as 0.73. Densification parameter was also increased due to addition of 1 wt. % yttria alumina garnet (YAG), value reached up to 0.75 as shown in Figure 5.2.

Austenitic Stainless Steel (316L)

Like 434L the experimental data before and after sintering for all the 316L samples with additives used in the present study are given in Appendices III and IV. In this case also sintered density increased with increasing sintering temperature. The variation sintered density with sintering temperature for selected 316L samples and with different additives composition was plotted in Figure 5.3. From the plot it is clearly revealed that the sintered density was not so much increased when sintered at 1400°C for pure 316L sample, it was only 85 %theoretical at 1250°C to 88 %theoretical at 1400°C. But increase in sintered density was obtained at 1400°C when

0.3 wt % FeB or NbB added as additive. From the Figure 5.3 the density at 1400°C was as high as 98% theoretical and after addition of YAG the sintered density increase up to 96% theoretical.

The variation of densification parameter with temperature of 316L samples with additives are given in Appendices III and IV. Effect of composition and temperature on densification parameter for selected 316L samples with additives was plotted in Figure 5.4. From the plots it is clearly evident that the samples sintered at 1400°C having better densification parameter than samples sintered at 1250°C. For 316L samples the value of densification parameter was also increased from 0.16 to 0.38 as sintering temperature increased from 1250 to 1400°C. But remarkable increase of this value obtained when sintering was done at 1400°C with boride additive. As like 434L samples similar trend was also obtained in samples with 1 wt. % YAG, in this case 0.81 value obtained.

5.1.2 Axial and Radial Shrinkage

Appendices V to VIII represent the axial and radial shrinkage of the all the 434L and 316L samples with additives after sintering. Figures 5.5 to 5.8 are show graphical representation of the axial versus radial shrinkage for the sintered samples of selected compositions. Careful observation of the Figures reveals that all the samples have undergone shrinkage on both axial and radial directions; no swelling has taken place in any of the samples. As sintering temperature increased from 1250 to 1400°C, the amount of shrinkage also increased. In most of the samples, the shrinkages in both directions are almost uniform. The line at 45° angle represents the

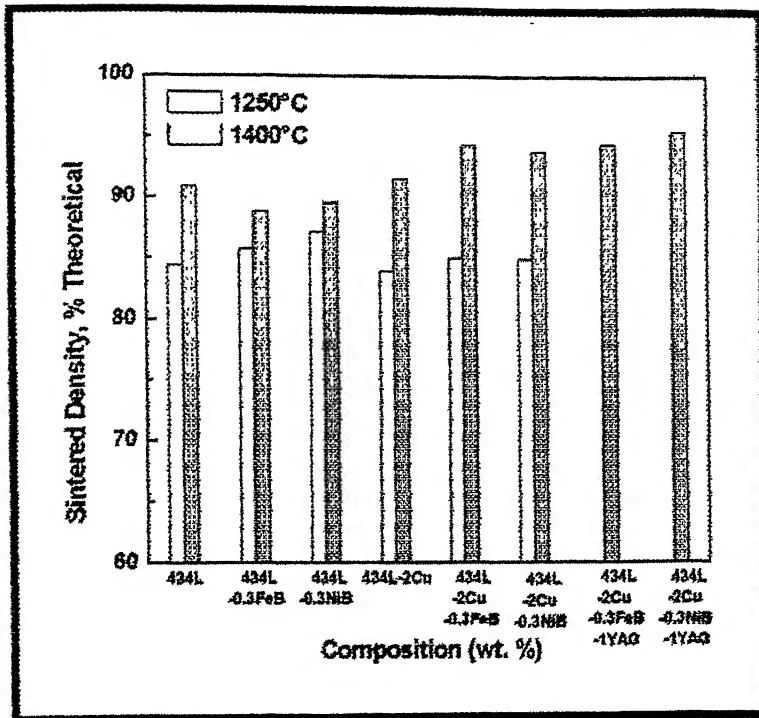


Figure 5.1 Variation of sintered density with sintering temperature for 434L samples with additives.

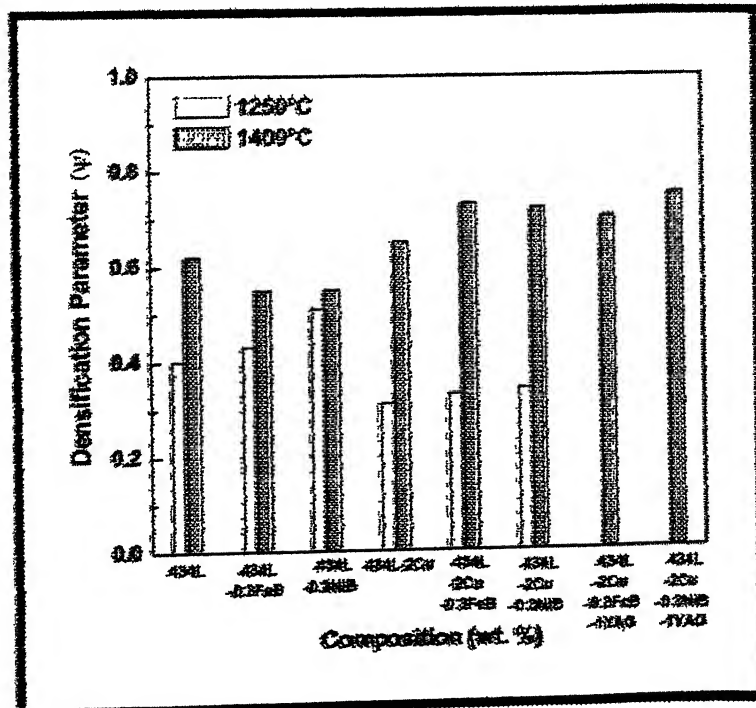


Figure 5.2 Variation of densification parameter with sintering temperature for 434L samples with additives.

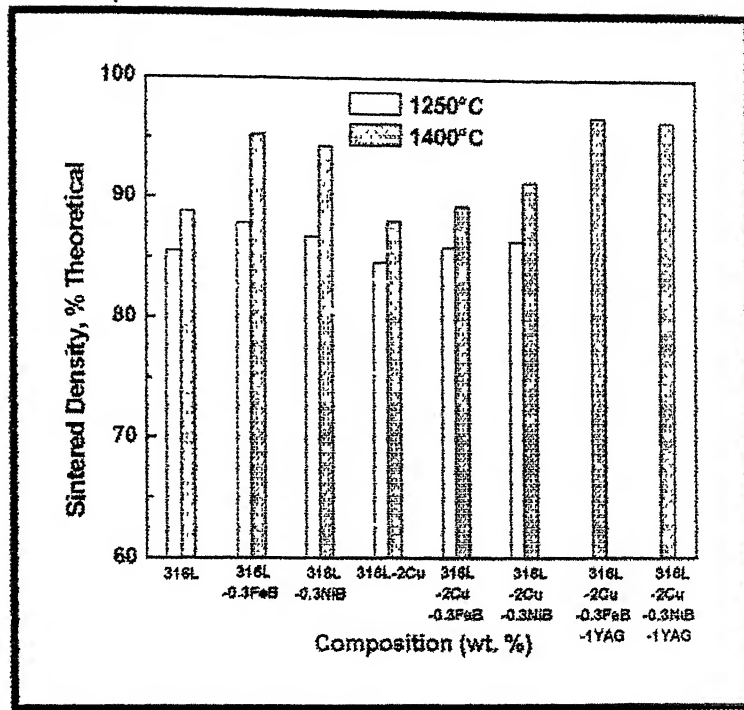


Figure 5.3 Variation of sintered density with sintering temperature for 316L samples with additives

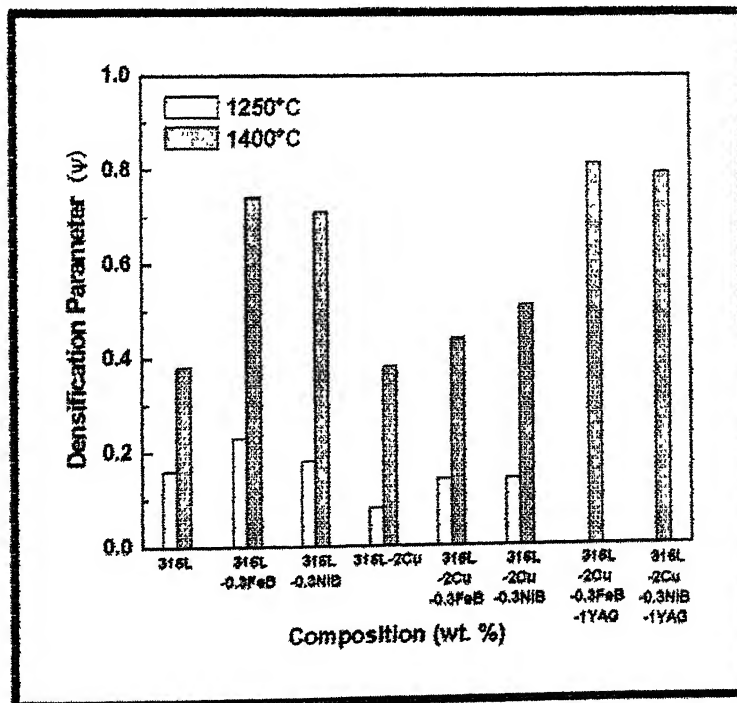


Figure 5.4 Variation of densification parameter with sintering temperature for 316L samples with additives.

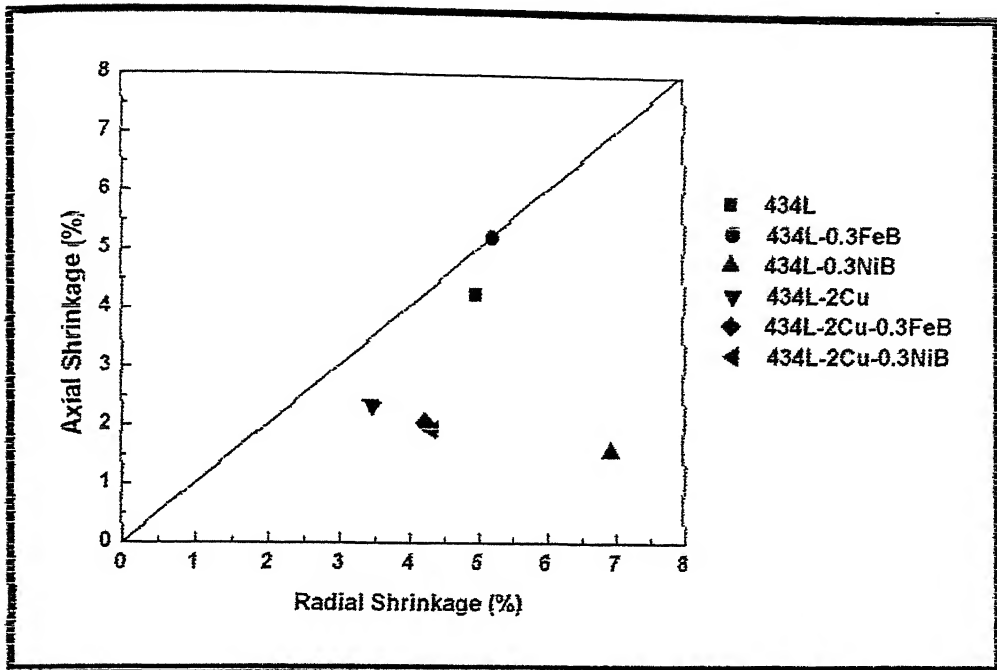


Figure 5.5 Variation of axial vs. radial shrinkage of 434L samples with additives sintered at 1250°C temperature.

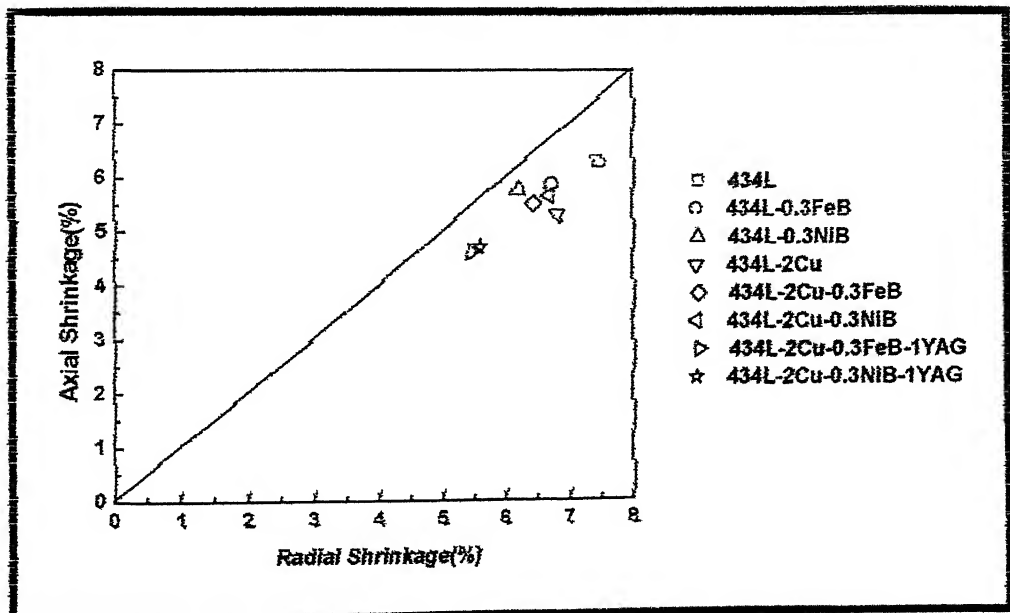


Figure 5.6 Variation of axial vs. radial shrinkage of 434L samples with additives sintered at 1400°C temperature.

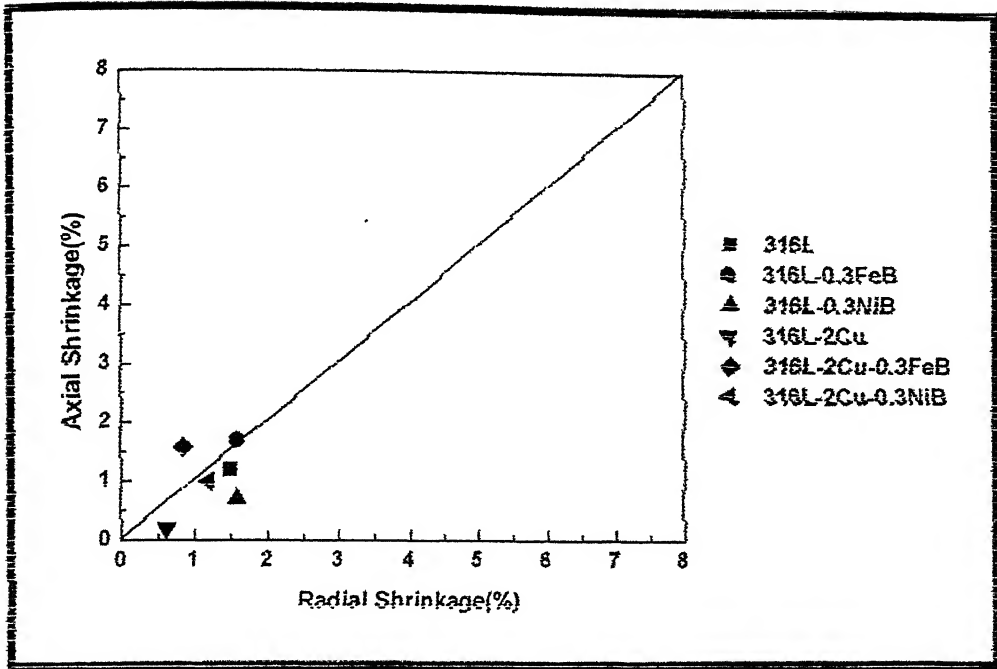


Figure 5.7 Variation of axial vs. radial shrinkage of 316L samples with additives sintered at 1250°C temperature.

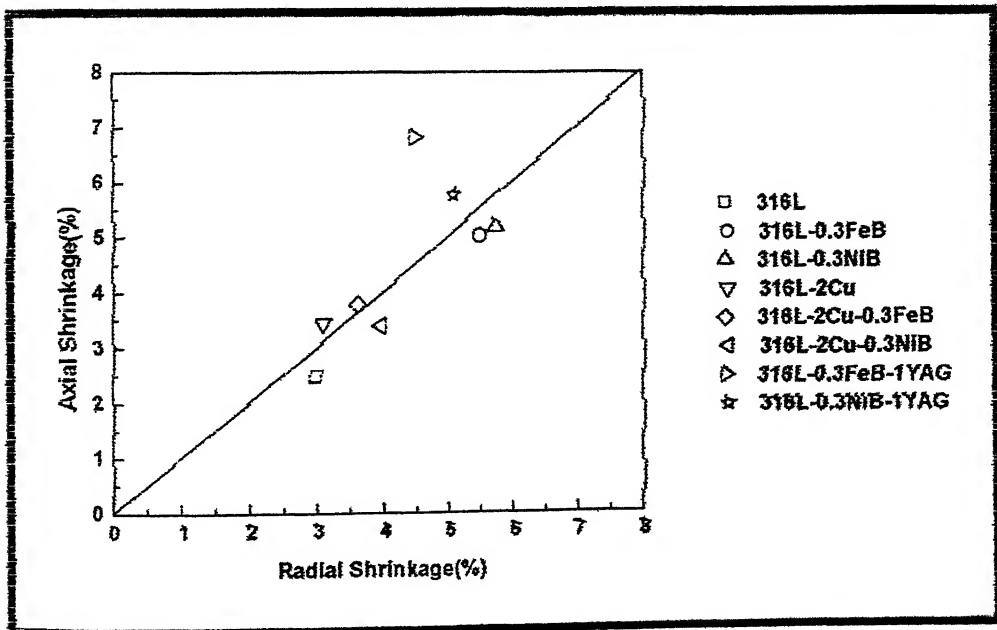


Figure 5.8 Variation of axial vs. radial shrinkage of 316L samples with additives sintered at 1400°C temperature.

ideal shrinkage with sintering temperature. In the present study discrepancy occurred due to development of density contour during uniaxial pressing.

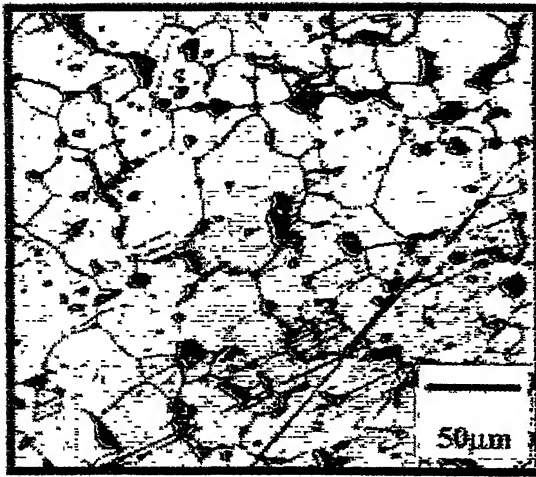
5.2 Optical Microscopy

Ferritic Stainless Steel (434L)

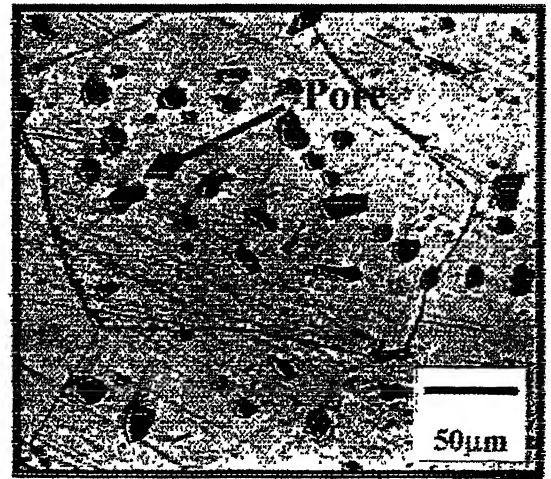
Figure 5.9 (a) and (b) show the optical micrographs of pure 434L sample sintered at 1250 and 1400°C, respectively. From the Figures it is clearly evident that at 1250°C sintering temperature the pores are mostly intergranular, whereas pores present at 1400°C are mostly intragranular and rounded. 1250°C sintering temperature is the solid state sintering temperature whereas 1400°C is the supersolidus liquid phase sintering (SLPS) temperature for both 434L and 316L stainless steel samples. To increase densification of the samples some additives were used such as copper and borides, later was added in the form of FeB and NiB. Additives were added in very small amount such as, maximum 2 wt% of copper and maximum 1.2 wt. % of borides.

Figures 5.10 and 5.11 shows the optical micrograph of 434L-2Cu samples sintered at 1250 and 1400°C, respectively. After sintering the liquid copper lefts behind a pore which is called secondary pore. This is represented by arrow mark.

FeB and NiB was added in the range of 0.3 to 1.2 wt. %. At 1250°C the volume fraction of liquid was very low, so the density was only 85 %theoretical for the sample containing 0.9 wt. % FeB. This is shown in Figure 5.12. But at 1400°C this density increased up to 91 %. Beyond that the density was almost constant. Optical micrograph of this sample is shown in Figure 5.13. For 434L stainless steel samples only boride addition was not so much effective for increasing densification.

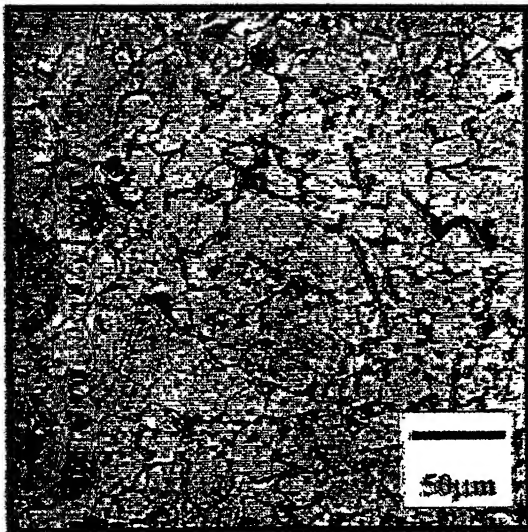


(a)

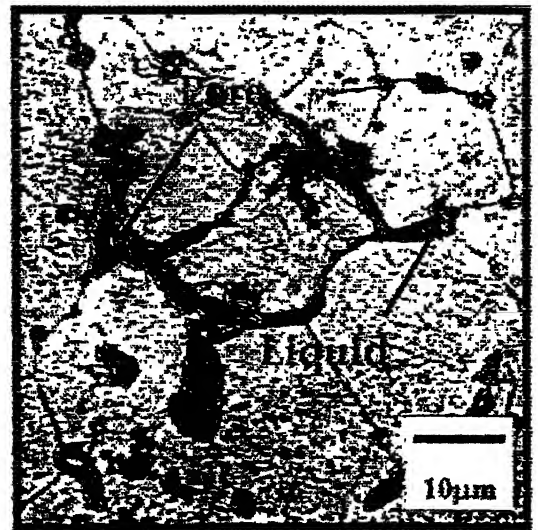


(b)

Figure 5.9 Optical micrographs of pure 434L samples sintered at (a) 1250°C and (b) 1400°C.



(a)



(b)

Figure 5.10 Optical micrographs of 434L-2Cu sample sintered at 1250°C (a) lower and (b) higher magnification.



Figure 5.11 Optical micrographs of 434L-2Cu sample sintered at 1400°C (a) lower and (b) higher magnification.

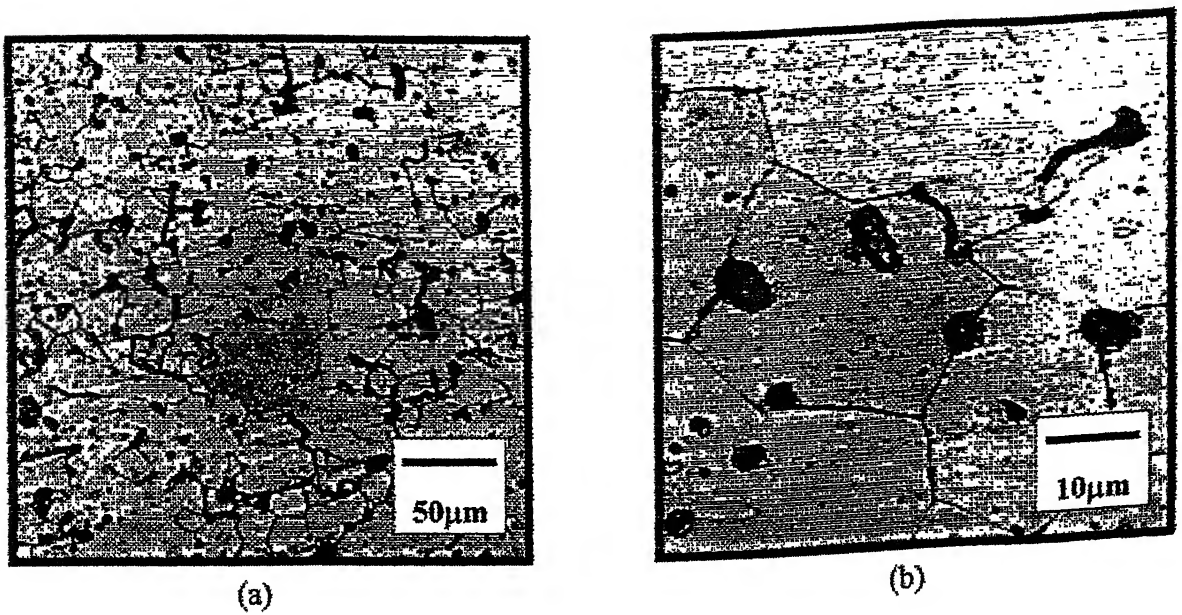
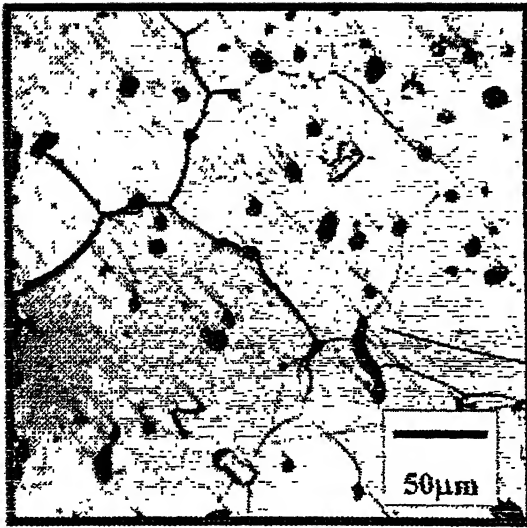
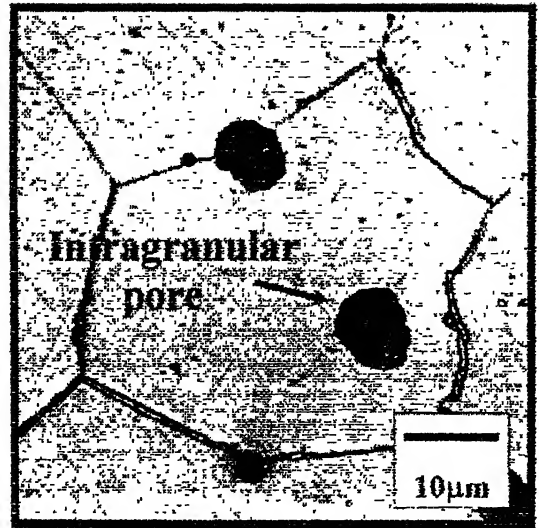


Figure 5.12 Optical micrographs of 434L-0.9FeB sample sintered at 1250°C (a) lower and (b) higher magnification.

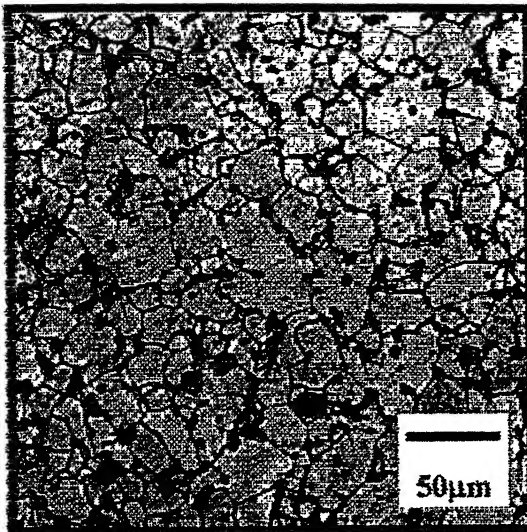


(a)

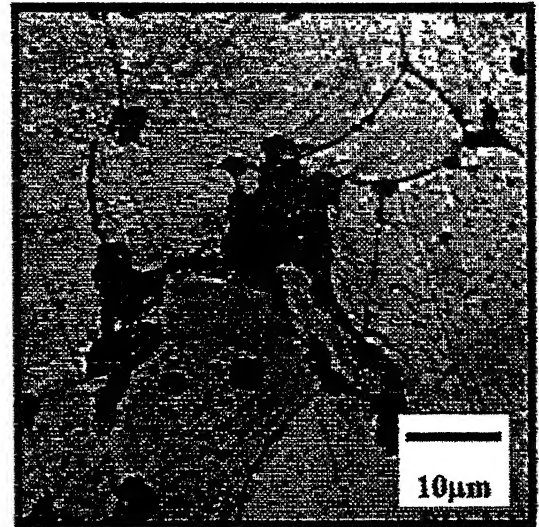


(b)

Figure 5.13 Optical micrographs of 434L-0.9FeB sample sintered at 1400°C (a) lower and (b) higher magnification.

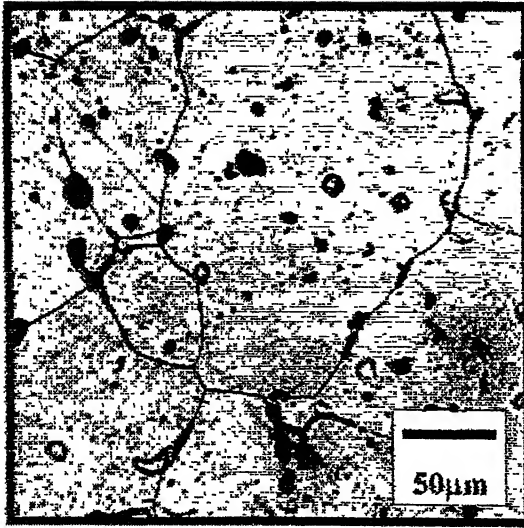


(a)

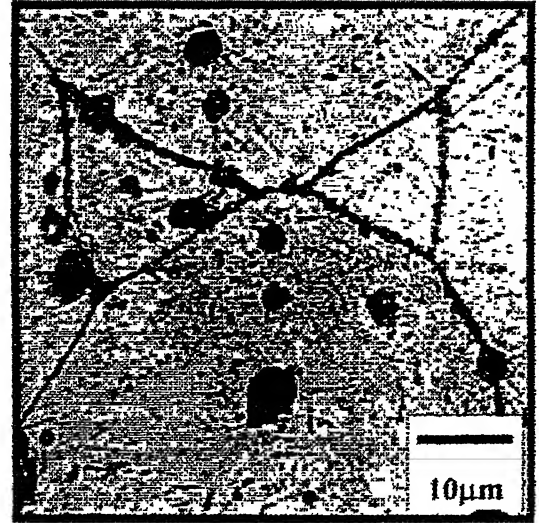


(b)

Figure 5.14 Optical micrographs of 434L-2Cu-0.3NiB sample sintered at 1250°C (a) lower and (b) higher magnification.

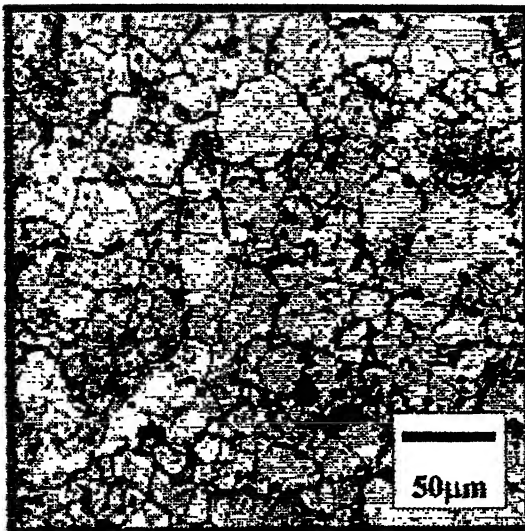


(a)

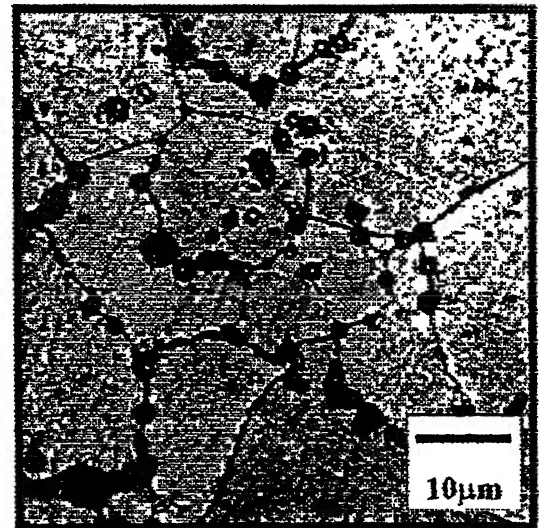


(b)

Figure 5.15 Optical micrographs of 434L-2Cu-0.3NiB sample sintered at 1400°C (a) lower and (b) higher magnification.

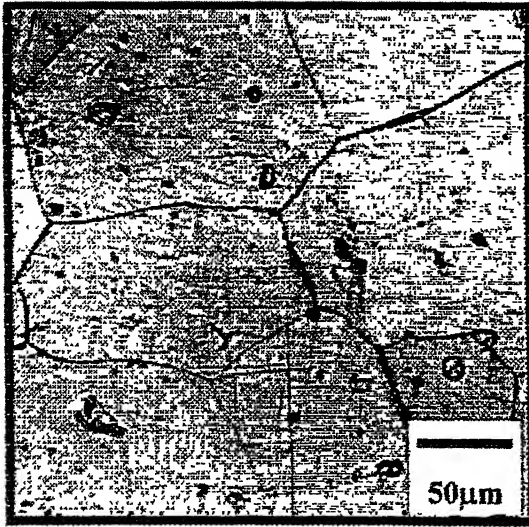


(a)

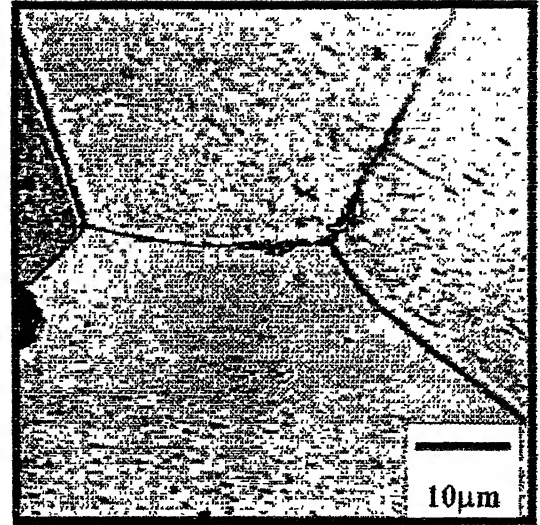


(b)

Figure 5.16 Optical micrographs of 434L-2Cu-0.3FeB sample sintered at 1250°C (a) lower and (b) higher magnification.

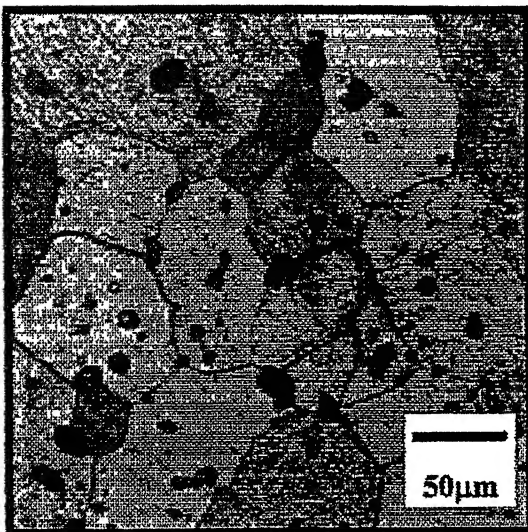


(a)

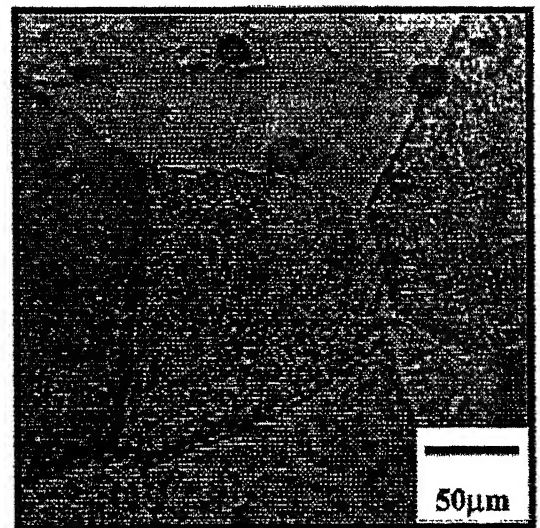


(b)

Figure 5.17 Optical micrographs of 434L-2Cu-0.3FeB sample sintered at 1400°C (a) lower and (b) higher magnification.

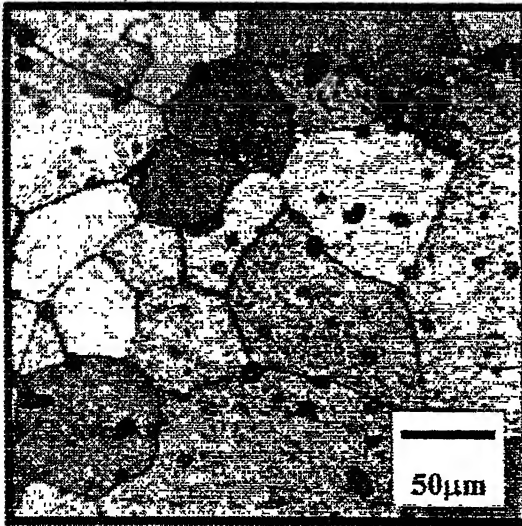


(a)

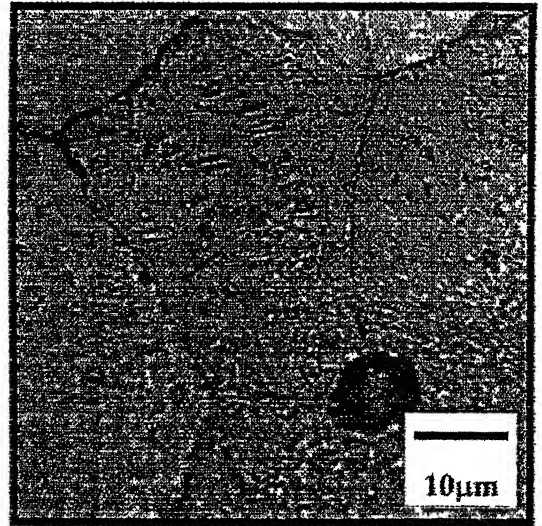


(b)

Figure 5.18 Optical micrographs of 434L-2Cu-0.3FeB-1YAG sample sintered at 1400°C (a) lower and (b) higher magnification.

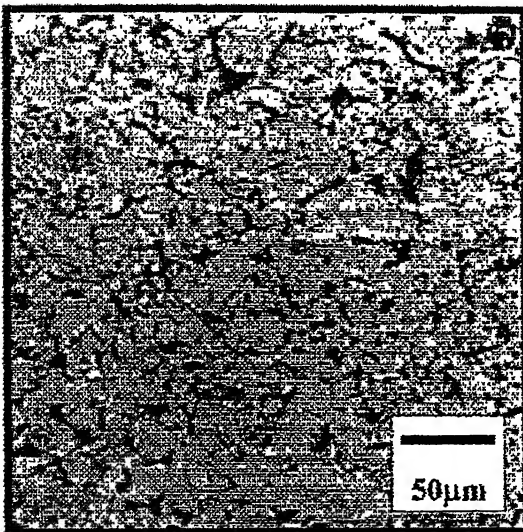


(a)

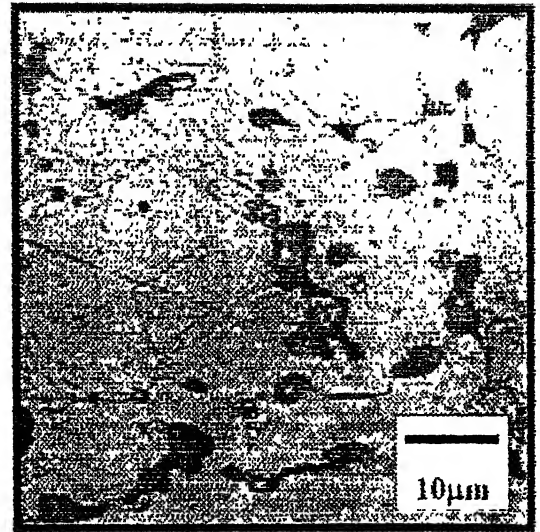


(b)

Figure 5.19 Optical micrographs of 434L-2Cu-0.3NiB-1YAG sample sintered at 1400°C (a) lower and (b) higher magnification.



(a)



(b)

Figure 5.20 Optical micrographs of pure 316L sample sintered at 1250°C (a) lower and (b) higher magnification.

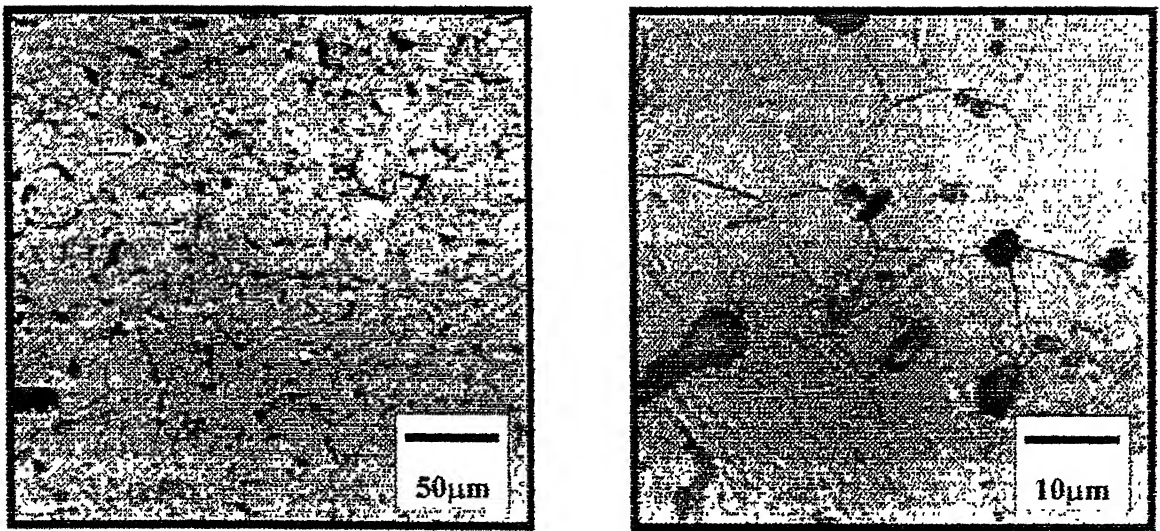


Figure 5.21 Optical micrographs of pure 316L sample sintered at 1400°C (a) lower and (b) higher magnification.

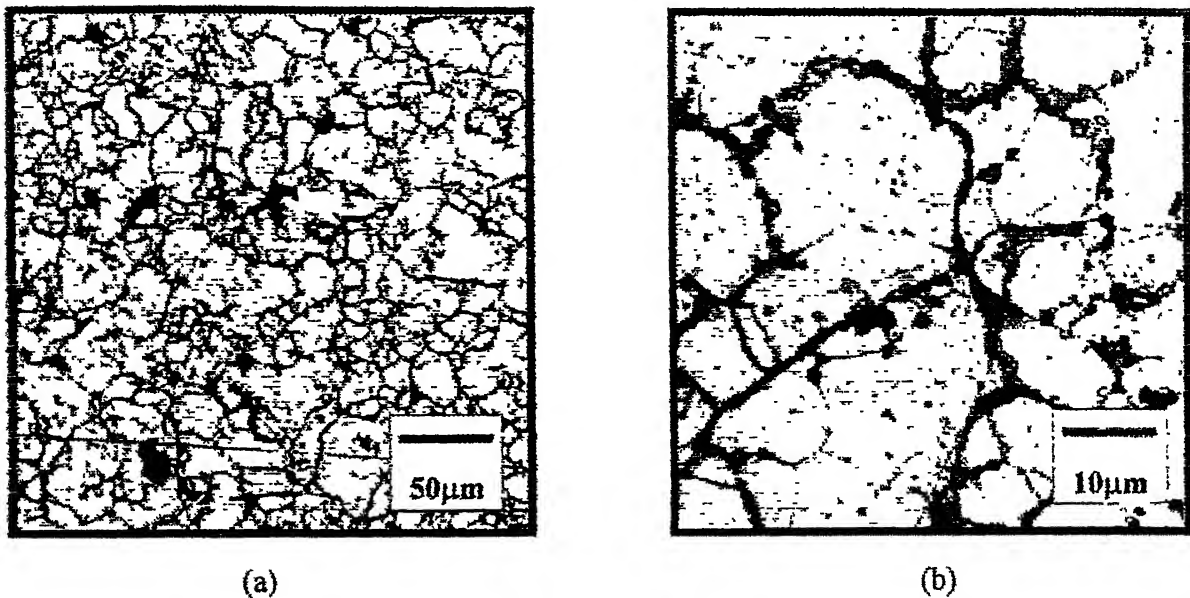


Figure 5.22 Optical micrographs of 316L-2Cu sample sintered at 1250°C (a) lower and (b) higher magnification.

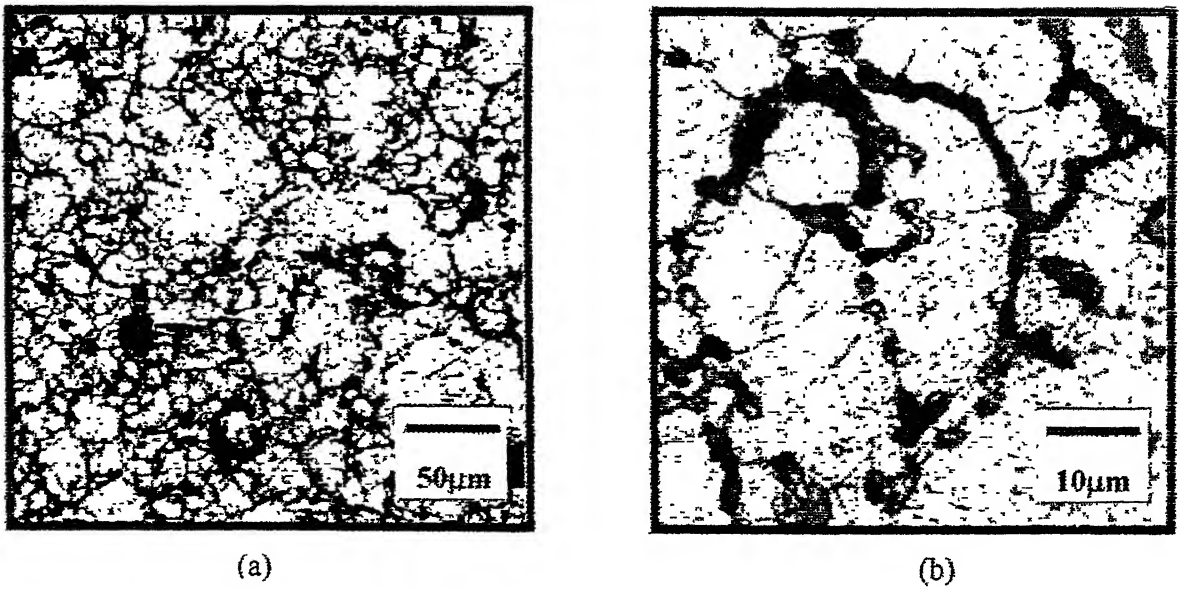


Figure 5.23 Optical micrographs of pure 316L-2Cu sample sintered at 1400°C (a) lower and (b) higher magnification.

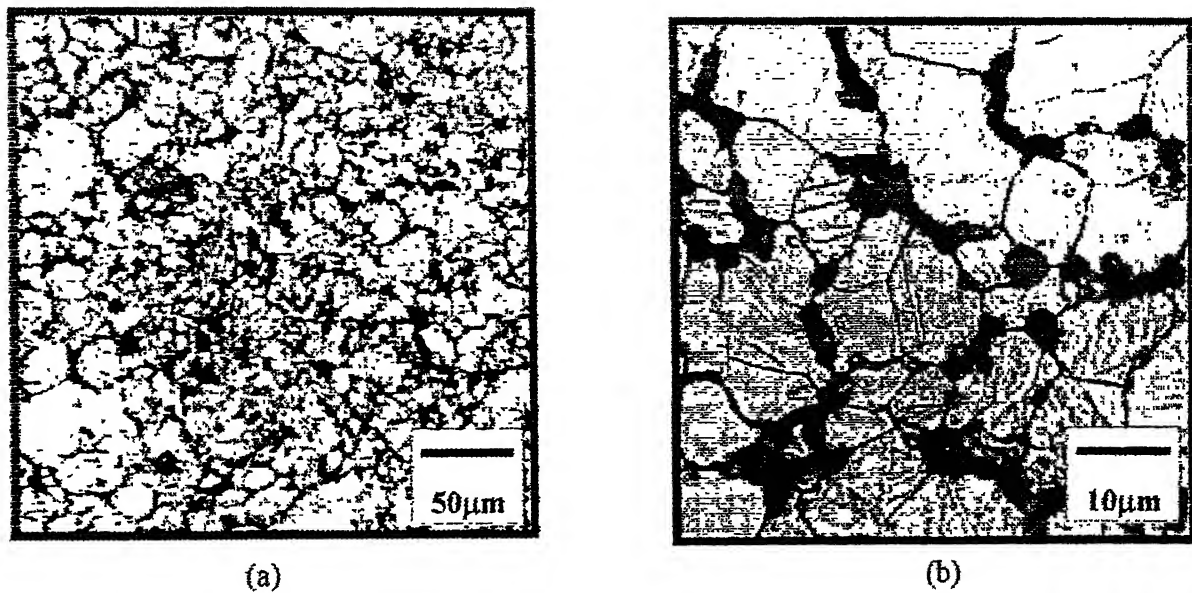
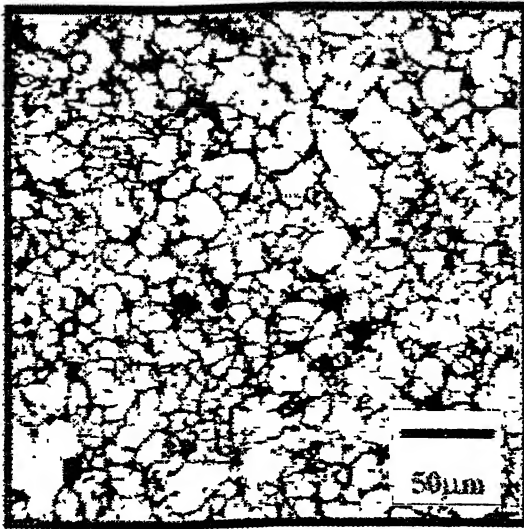
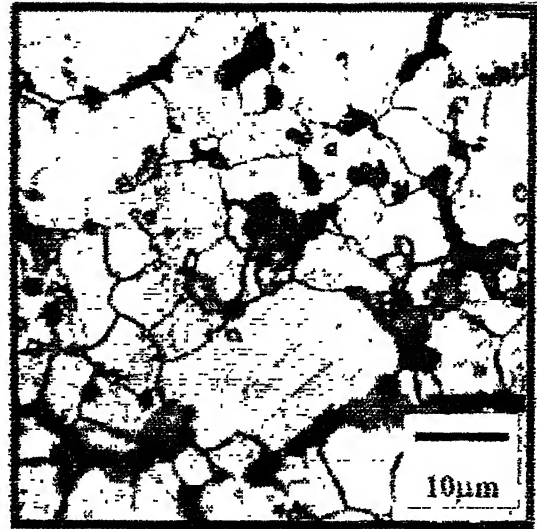


Figure 5.24 Optical micrographs of 316L-0.3FeB sample sintered at 1250°C (a) lower and (b) higher magnification.

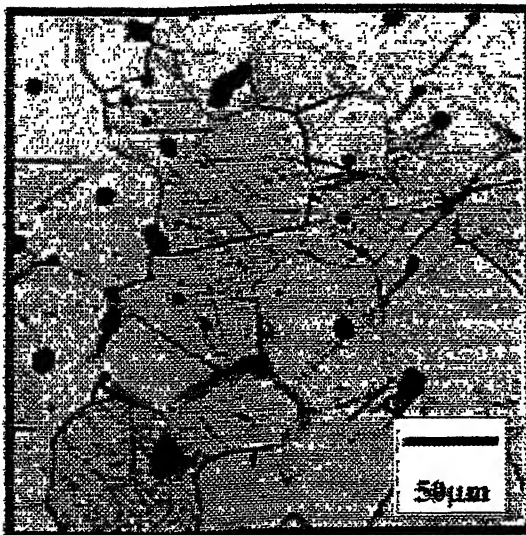


(a)

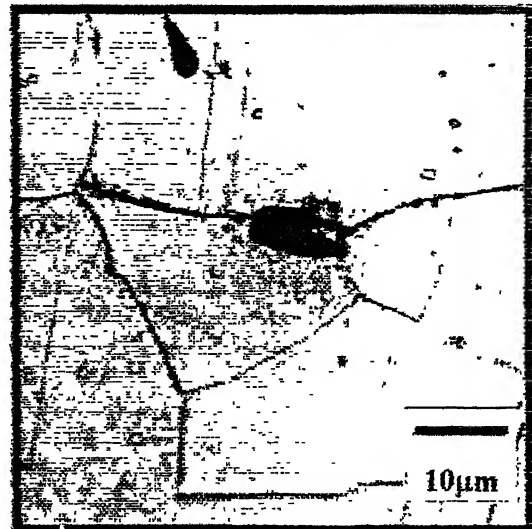


(b)

Figure 5.25 Optical micrographs of 316L-0.3NiB sample sintered at 1250°C (a) lower and (b) higher magnification.

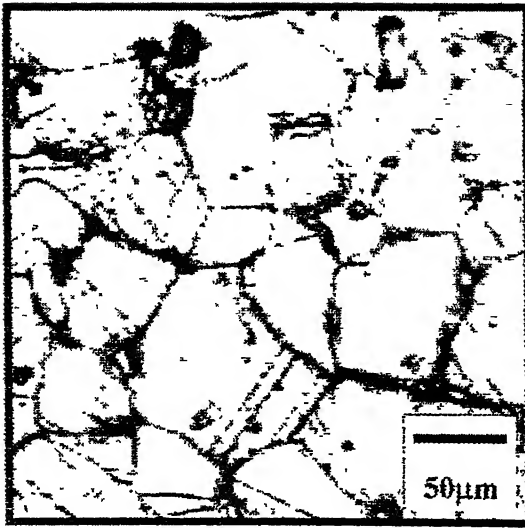


(a)

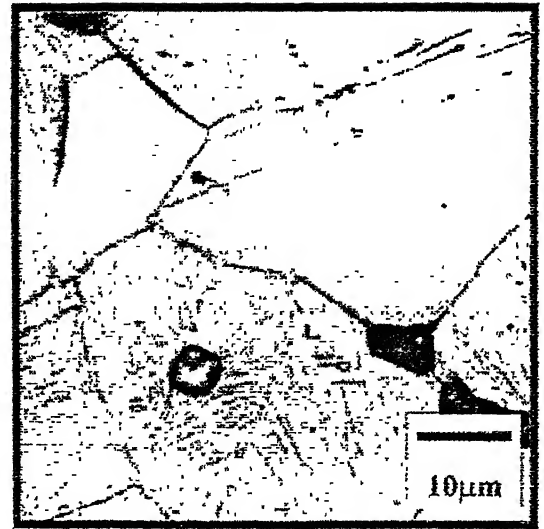


(b)

Figure 5.26 Optical micrographs of 316L-0.3FeB sample sintered at 1400°C (a) lower and (b) higher magnification.

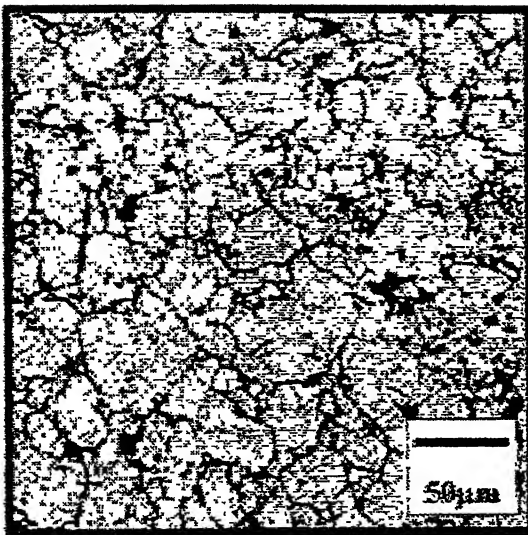


(a)

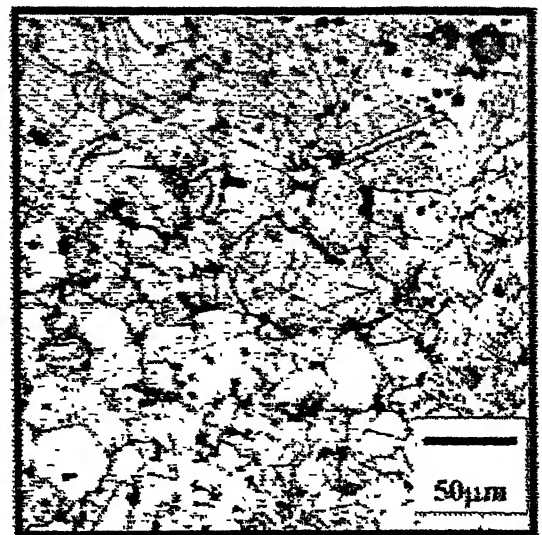


(b)

Figure 5.27 Optical micrographs of 316L-0.3NiB sample sintered at 1400°C (a) lower and (b) higher magnification.

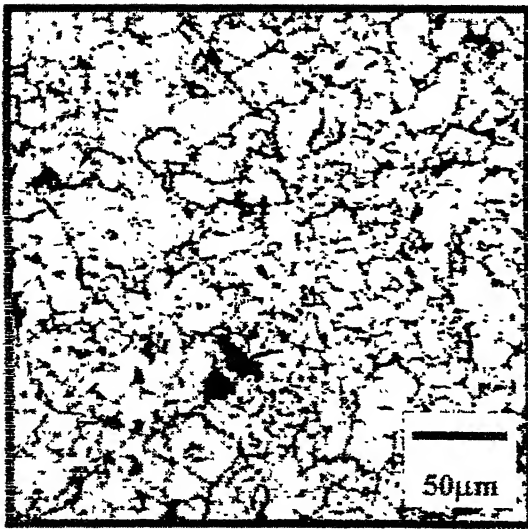


(a)

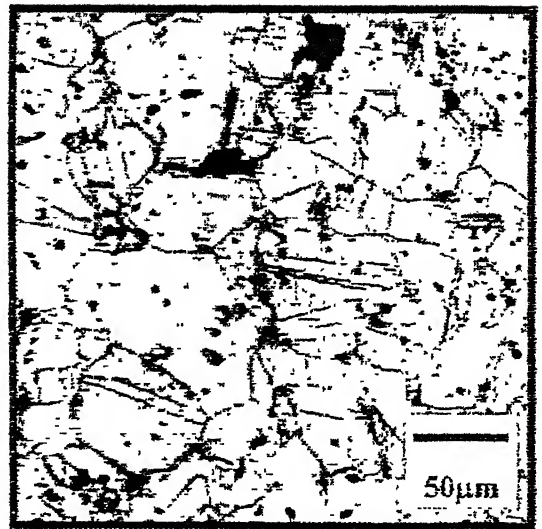


(b)

Figure 5.28 Optical micrographs of 316L-2Cu-0.3FeB samples sintered at (a) 1250°C and (b) 1400°C.

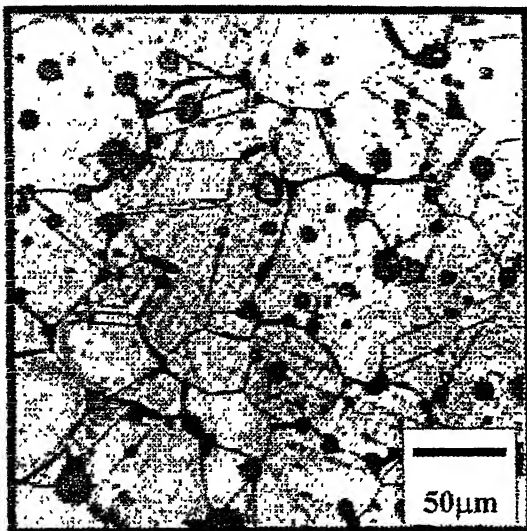


(a)

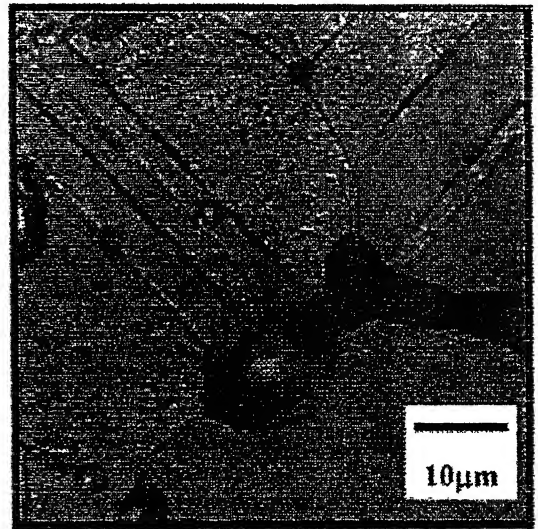


(b)

Figure 5.29 Optical micrographs of 316L-2Cu-0.3NiB samples sintered at (a) 1250°C and (b) 1400°C.

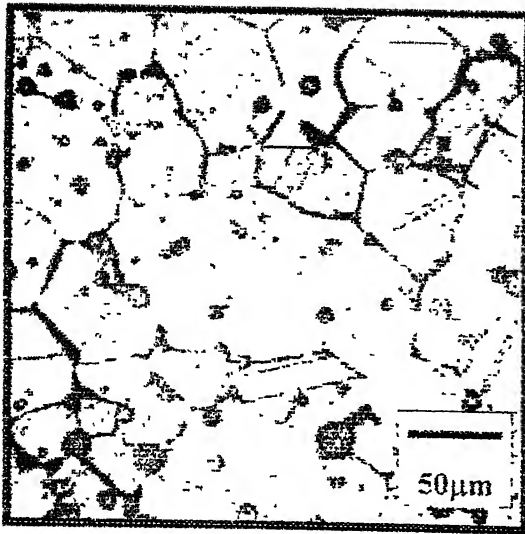


(a)

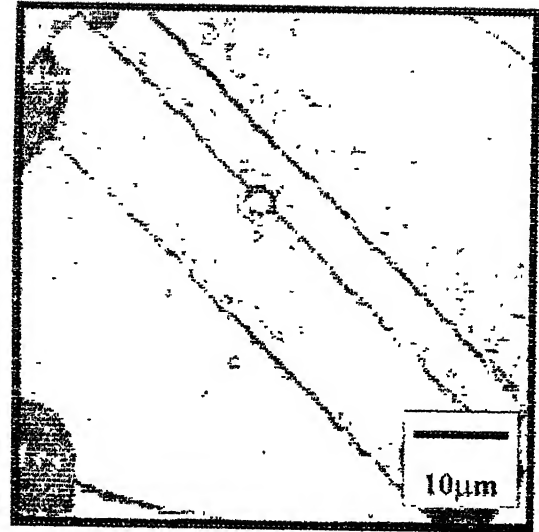


(b)

Figure 5.30 Optical micrographs of 316L-0.3FeB-1YAG sample sintered at 1400°C (a) lower and (b) higher magnification.



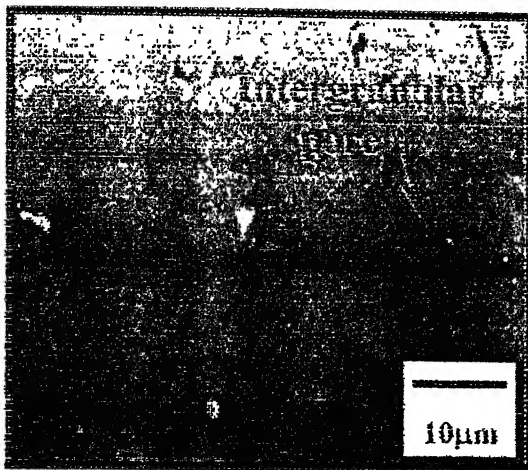
(a)



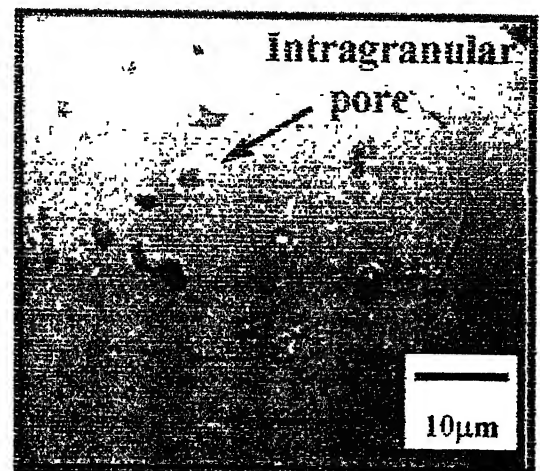
(b)

Figure 5.31 Optical micrographs of 316L-0.3NiB-1YAG sample sintered at 1400°C

(a) lower and (b) higher magnification.



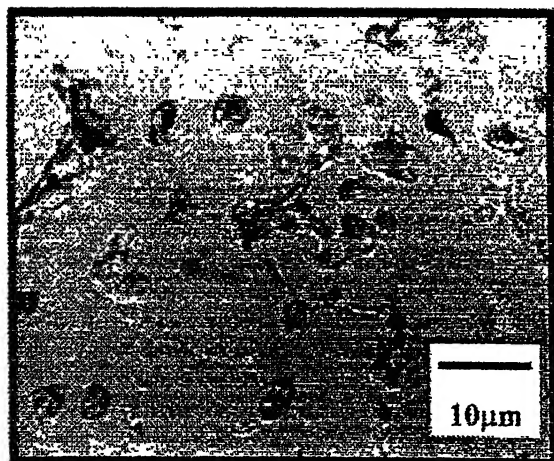
(a)



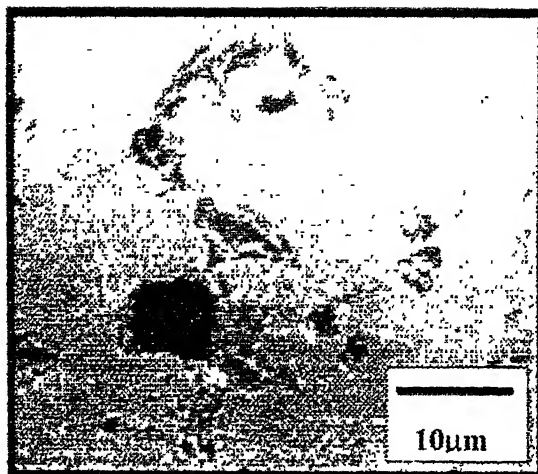
(b)

Figure 5.32 SEM micrographs of pure 434L samples sintered at (a) 1250°C and (b)

1400°C.

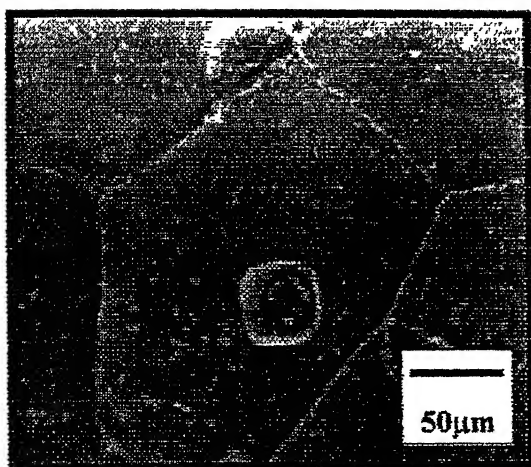


(a)

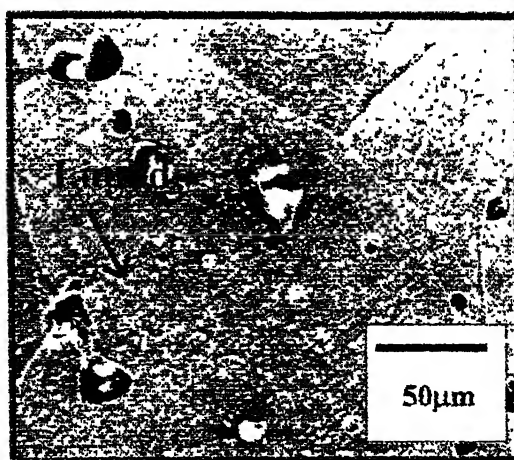


(b)

Figure 5.33 SEM micrographs of 434L-2Cu sample sintered at 1250°C (a) lower and (b) higher magnification.

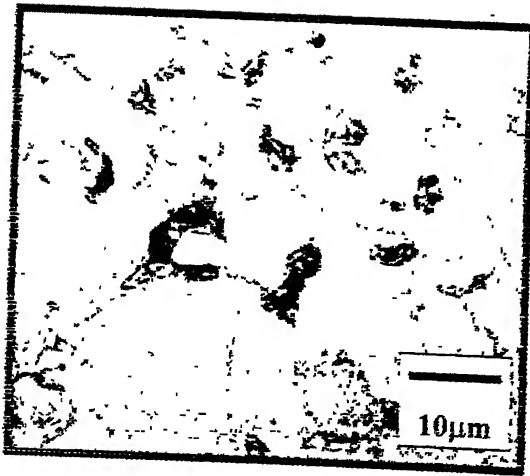


(a)

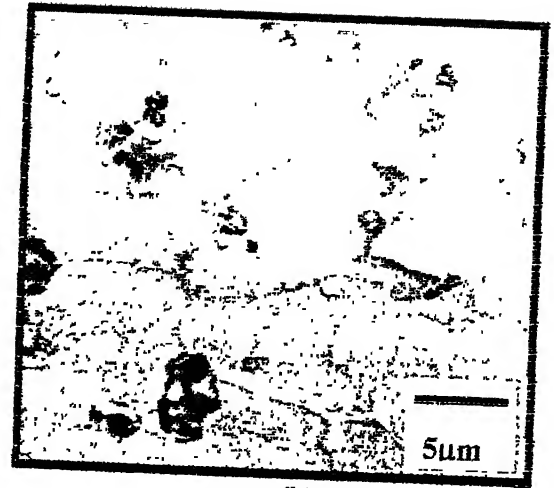


(b)

Figure 5.34. SEM micrographs of 434L-2Cu sample sintered at 1400°C (a) lower and (b) higher magnification.

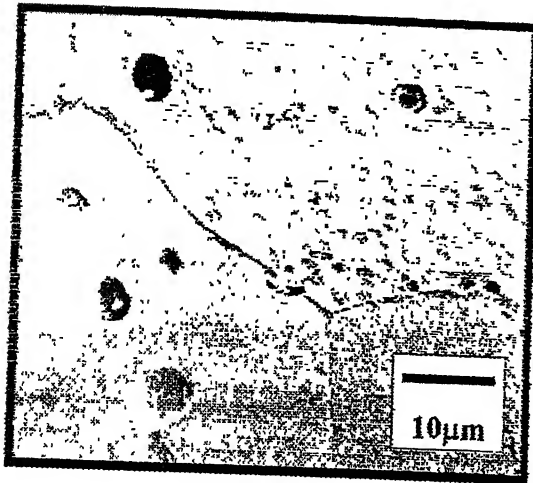


(a)

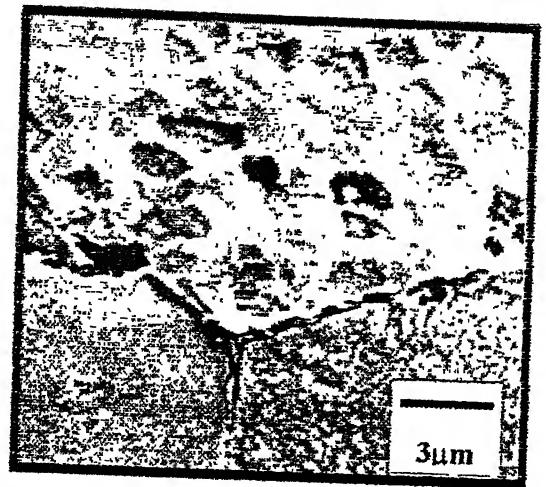


(b)

Figure 5.35 SEM micrographs of 434L-2Cu-0.3FeB sample sintered at 1250°C (a) lower and (b) higher magnification.



(a)



(b)

Figure 5.36 SEM micrographs of 434L-2Cu-0.3FeB sample sintered at 1400°C (a) lower and (b) higher magnification.

Maximum density was obtained up to 94 %theoretical in the sample containing 0.3 wt. % FeB or NiB along with 2 wt. % copper. Figures 5.14 and 5.15 show the optical micrograph of sample containing 2 wt. % Cu and 0.3 wt. % NiB sintered at 1250 and 1400°C, respectively. As shown in Figure 5.16, the necklace type of structure was obtained in the sample containing 2 wt. % Cu and 0.3 wt. % FeB sintered at 1250°C. Figure 5.17 shows the micrograph of the sample with same composition sintered at 1400°C. In this micrograph the pores are mostly present at triple point and the intragranular pores are almost rounded.

Grain growth is the main disadvantage of high temperature sintering such as at 1400°C. To suppress this some refractory material such as Yttria Alumina Garnet (YAG) was added. It prevents the grain growth and thus prevents pores to be intragranular. There are two samples sintered at 1400°C were chosen having maximum density for YAG addition. Figures 5.18 and 5.19 show the optical micrographs of samples containing 434L-2 wt. % Cu-0.3 wt. % FeB and 434L-2 wt. % Cu-0.3 wt. % NiB, respectively along with 1 wt. % YAG.

Austenitic Stainless Steel (316L)

Intergranular pore become intragranular was also occurred in 316L samples as sintering temperature increases from 1250 to 1400°C. Figures 5.20 and 5.21 represent the optical micrographs of pure 316L samples sintered at 1250 and 1400°C, respectively. To increase the densification here also copper and boride additives were added.

In 316 L-2 wt. % Cu samples the traces of liquid copper is missing because of higher solubility of copper into the austenite. This feature was captured in Figures 5.22 and 5.23, where samples are sintered at 1250 and 1400°C, respectively.

Only 0.3 wt% FeB or NiB is sufficient for enhancing the densification of 316L stainless steel samples. Large irregular pores mostly at the grain boundaries were obtained in the samples containing 0.3 wt. % FeB or NiB sintered at 1250°C. Figures 5.24 and 5.25 show the optical micrographs of these samples containing FeB and NiB, respectively. At 1400°C SLPS was occurred. At this temperature the volume fraction of liquid was also high compare to 1250°C temperature. Figures 5.26 and 5.27 represents microstructure of above samples containing FeB and NiB, respectively sintered at 1400°C. In this case maximum 96 %theoretical density was obtained. From the figures it is clearly evident that most of the pores are present at the triple points and the intragranular pores are rounded in shape.

In the 316L samples copper along with boride addition was not effective to enhance densification. Pores are mostly at grain boundaries at 1250°C and it became intragranular at 1400°C. This features were captured in Figures 5.28 and 5.29 containing 0.3wt% FeB and NiB along with 2wt% copper, respectively.

Here also grain growth was taken place when sintering was done at 1400°C. To suppress this Ytria Alumina Garnet (YAG) was added. It prevents the grain growth. Figures 5.30 and 5.31 show the micrograph of sample containing 0.3 wt. % FeB and NiB, respectively along with 1 wt. % YAG sintered at 1400°C

5.3 Scanning Electron Microscopy

Before taking the micrograph under SEM the samples were deeply etched. Figures 5.32 (a) and (b) show the SEM micrograph of pure 434L samples sintered at 1250°C and 1400°C. From the figures it is clearly evident that at 1250°C temperature the pores are presents along the grain boundaries and in irregular shape. At 1400°C sintering temperature grain growth was taken place and the pores were mostly

intragranular type. These features are marked by arrow. As shown in Figure 5.34 white spots were seen within the grain in the sample containing 434L along with 2 wt. % copper sintered at 1400°C. It was nothing but the liquid formation taken place in the defect site of the grains. Here the thickness of grain boundaries was high; it is due to the presence of liquid copper. As shown in Figure 5.33 such features were absent in the sample having the same composition sintered at 1250°C. Figures 5.35 and 5.36 show the SEM micrographs of 434L sample containing 2 wt. % Cu and 0.3 wt. % FeB sintered at 1250°C and 1400°C respectively. At 1250°C the irregular elongated pores are present along grain boundaries. When sintered at 1400°C the liquid formation occurred along grain boundaries and within the defect site of the grain, also pores were mostly within grain and rounded in nature.

5.4 Study of Mechanical Properties

5.4.1 Hardness

5.4.1.1 Bulk hardness

Bulk hardness of the all samples used in the present study are given in the Appendices IX to X. The hardness was taken using 2 Kg load applied for 15 seconds

Ferritic Stainless Steel (434L)

The variation of the hardness as a function of sintering temperature of selected composition is plotted in Figures 5.37. The hardness values increases with increasing of sintering temperature from 1250 to 1400°C. It is due to decrease of porosity. For pure 434L sample the hardness increases from VHN 116 to VHN 137 as sintering temperature increases from 1250 to 1400°C. But the remarkable of hardness was taken place in the 434L samples containing 2 wt. % Cu along with 0.3 wt. % FeB or NiB. In these cases the value increased up-to as high as VHN 165. Another additive

YAG was also added to enhance mechanical properties. For this case hardness increases as high as VHN 220

Austenitic Stainless Steel (434L)

Similar trend was also observed in 316L samples with additives. Hardness increases from VHN 126 to VHN 156 as sintering temperature increases from 1250 to 1400°C. Maximum hardness were obtained in the samples containing 0.3 wt. % FeB or NiB. The value of these samples were VHN 189 and VHN 191 for 0.3 wt. % FeB and 0.3 wt. % NiB, respectively. Figure 5.38 represents the variation of hardness value as a function of sintering temperature of selective composition. Here also due to addition of YAG hardness increased up to VHN 238.

5.4.1.2 Microhardness

Microhardness of the all samples used in the present study is given in the Appendix XI. The hardness was taken using 5 gm load applied for 15 sec

Ferritic Stainless Steel (434L)

For the 434L samples with additives the variation of the hardness as a function of sintering temperature of selected composition are plotted in Figures 5.39. As of bulk hardness microhardness value also increased with increasing of sintering temperature from 1250 to 1400°C. It is due to increase of densification. For pure 434L sample the hardness increases from VHN 85 to VHN 106 as sintering temperature increases from 1250 to 1400°C. 434L sample containing 2wt. % copper show lower hardness compare to pure 434L sample. But the remarkable increase of hardness was taken place in the 434L samples containing 2 wt. % Cu along with 0.3 wt. % FeB or NiB. In these cases the value increased up-to as high as VHN 156. Microhardness values further increased due to addition of YAG. In this case maximum VHN 196

value obtained in the sample containing 2 wt % Cu and 0.3 wt. % NiB along with 1 wt % YAG

Austenitic Stainless Steel (434L)

Similar trend was also observed in 316L samples with additives. For pure 316L sample hardness increases from VHN 85 to VHN 121 as sintering temperature increases from 1250 to 1400°C. Maximum hardness were obtained in the samples containing 0.3 wt. % FeB or NiB. The value of these samples were VHN 160 and VHN 166 for 0.3 wt. % FeB and 0.3 wt. % NiB, respectively. Like 434L samples microhardness values also increases with addition of YAG. VHN 221 value was obtained in the sample containing 0.3 wt. % FeB along with 1 wt. % YAG. Figure 5.40 represents the microhardness values of selected composition as a function of sintering temperature.

5.4.2 Tensile Properties

During sintering at 1400°C grain growth was taken place. To restrict this 1 wt. % YAG was added along with the other additives. To measure the tensile properties such compositions were chosen which possess maximum density.

Ferritic Stainless Steel (434L)

For tensile properties measurement two most dense composition were taken, these are 434L-2 wt. % Cu-0.3 wt. % FeB-1 wt. % YAG and 434L-2 wt. % Cu-0.3 wt. % NiB-1 wt. % YAG sintered at 1400°C. To compare the tensile properties of the above samples, tensile properties of pure 434L was also measured. Table 5.1 shows the tensile properties of above samples. The yield strength of pure 434L sample increased from 256 to 398 MPa when copper, FeB, and YAG was added. Similar

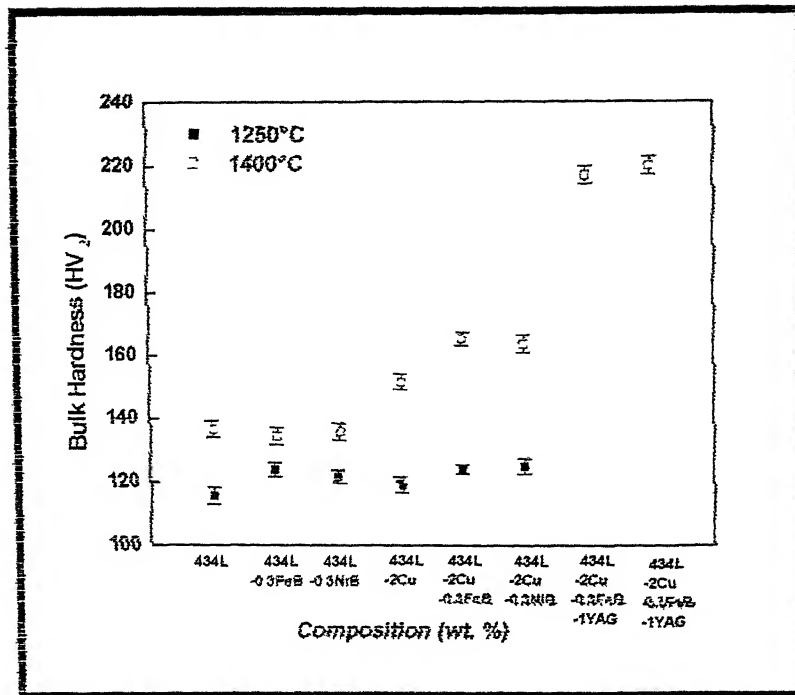


Figure 5.37 Variation of bulk hardness values as a function of sintering temperature for 434L samples with additives

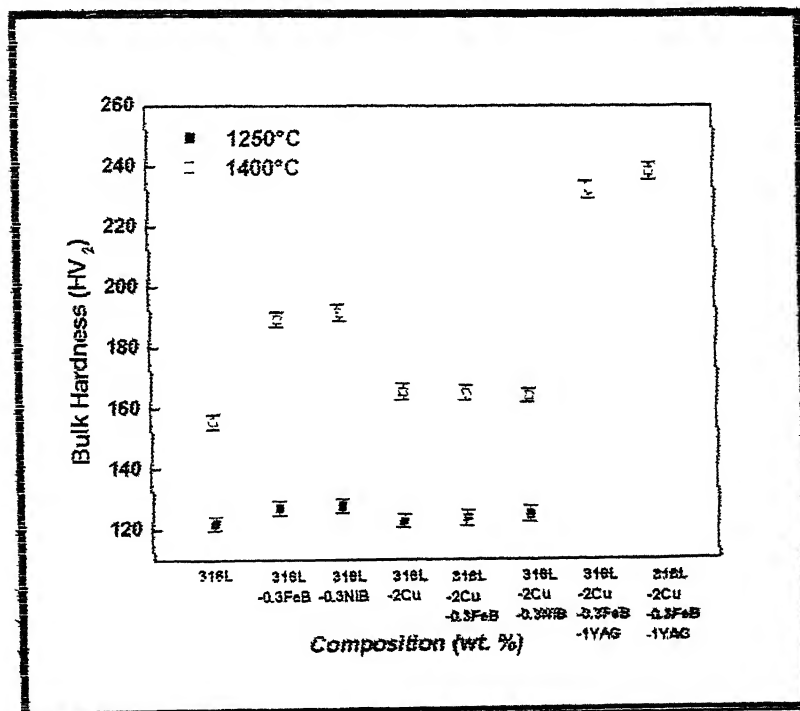


Figure 5.38 Variation of bulk hardness values as a function of sintering temperature for 316L samples with additives.

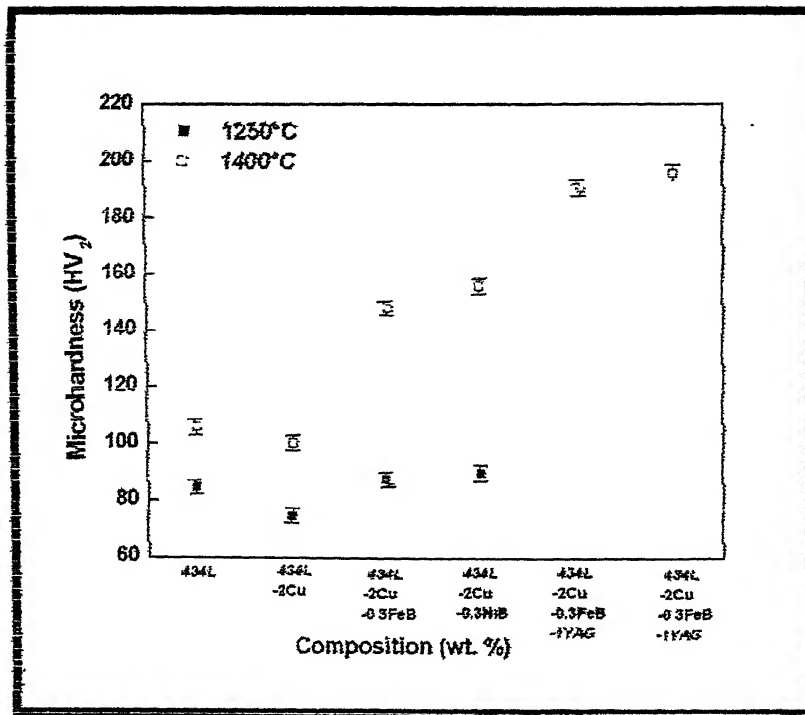


Figure 5.39 Variation of microhardness values as a function of sintering temperature for 434L samples with additives.

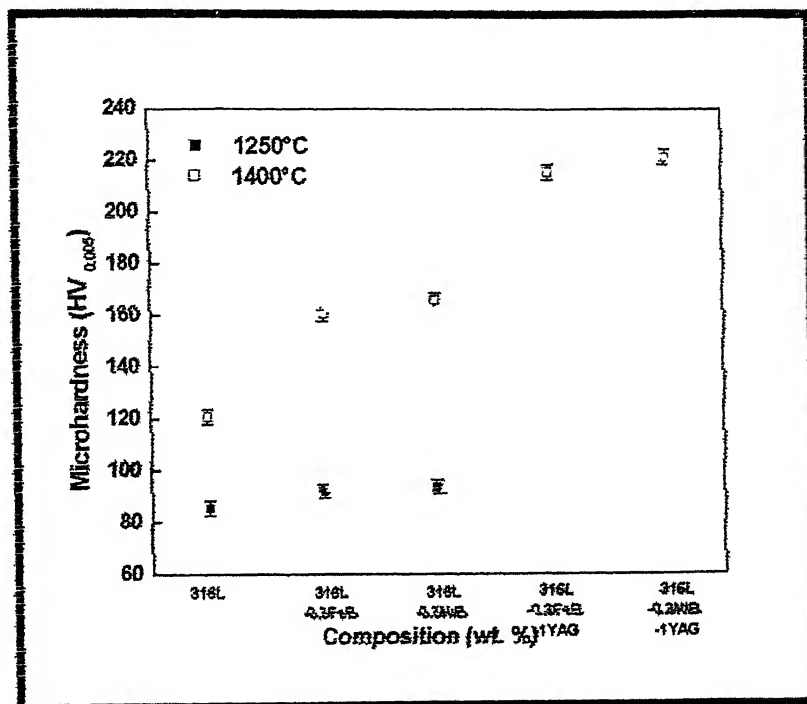


Figure 5.40 Variation of microhardness values as a function of sintering temperature for 316L samples with additives.

trend also obtained in the sample containing copper, NiB, and YAG. In this case yield strength value increased from 256 to 442 MPa. The maximum UTS 574 MPa was obtained in the sample containing Cu, NiB, and YAG. The stress-strain curve of 434L samples with additives are plotted in Figure 5.41. Micrographs of the fracture surfaces are given in Figures 5.42 to 5.44.

Austenitic Stainless Steel (434L)

The yield strength of pure 316L sample increased from 275 to 333 MPa when 0.3 wt. % FeB, and 1 wt. % YAG was added. Similar trend also obtained in the sample containing 0.3 wt. % NiB, and 1 wt. % YAG. In this case yield strength value increased from 275 to 355 MPa. The maximum UTS 654 MPa was obtained in the sample containing 0.3 wt. % NiB, and 1 wt. % YAG. Table 5.1 summarises the tensile properties of pure 316L samples with additives. The stress-strain curve of 316L samples with additives are plotted in Figure 5.45 and micrographs of fracture surfaces are given in Figure 5.46 to 5.48.

5.5. Phase Identification by XRD

X-Ray Diffraction measurements were made for identify of any new phase formation which could impact on mechanical properties. Figures 5.49 and 5.50 show the XRD patterns of 434L and 316L samples with additives, respectively sintered at 1400°C. Comparison was made between the three strong intensity values of XRD plots with standard JCPDS cards. There was no new phase found.

Table 5.1 Tensile properties of selected samples.

Composition (Wt. %)	Yield Strength (MPa)	UTS (MPa)	% Elongation
434L	256	379	30
434L-2Cu-0.3FeB-1YAG	398	512	21
434L-2Cu-0.3NiB-1YAG	442	574	16
316L	172	336	47
316L-0.3FeB-1YAG	333	632	31
316L-0.3NiB-1YAG	355	654	27

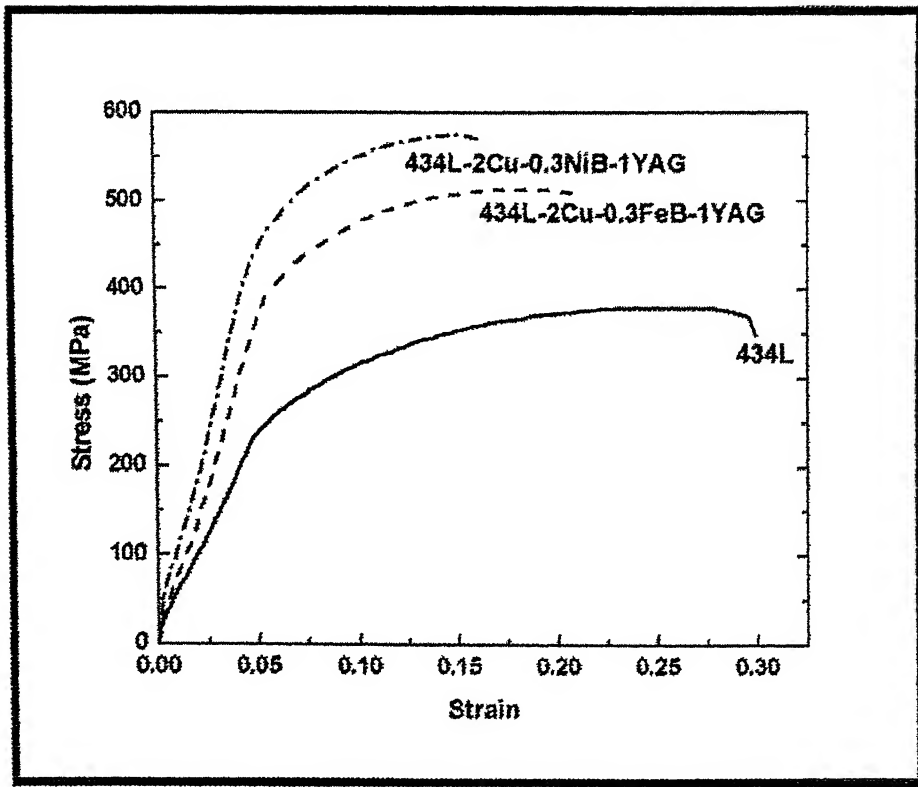


Figure 5.41 Stress-strain curve of 434L samples with additives.

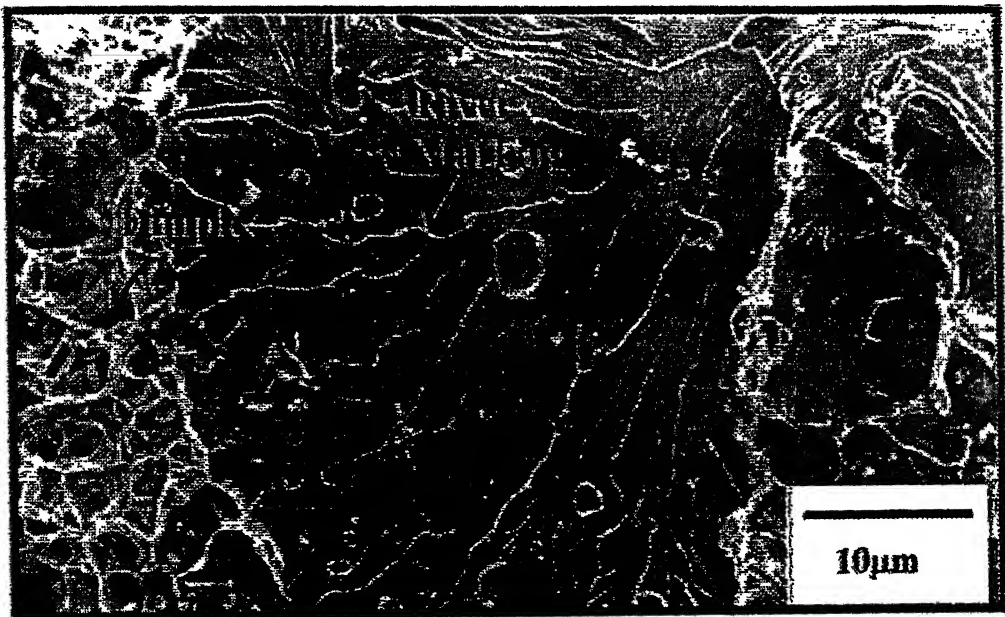


Figure 5.42 SEM micrograph of fracture surface of 434L sample sintered at 1400°C.

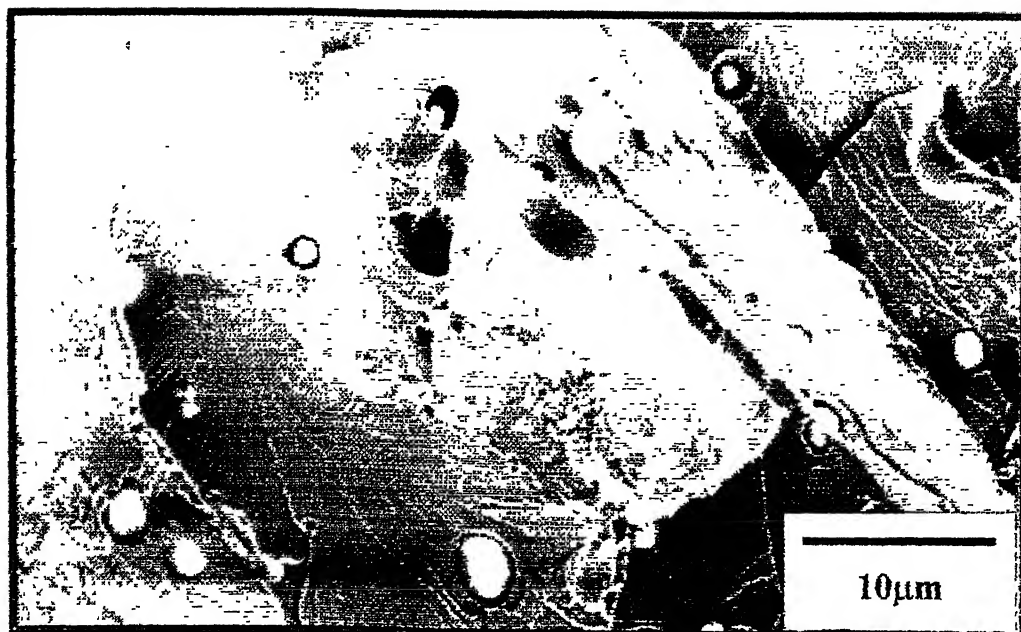


Figure 5.43 SEM micrograph of fracture surface of 434L-2Cu-0.3FeB-1YAG sample sintered at 1400°C

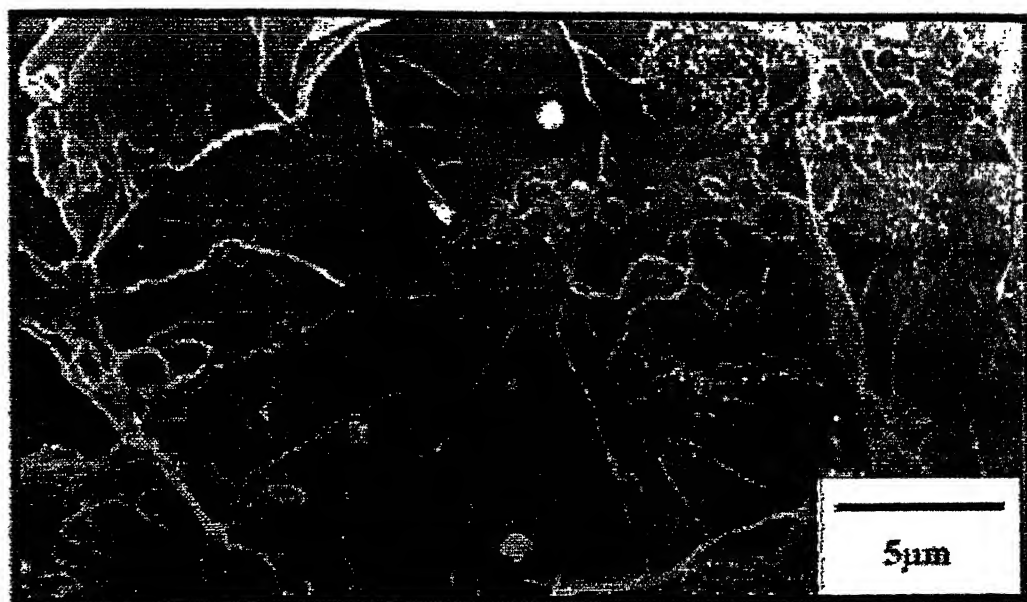


Figure 5.44 SEM micrograph of fracture surface of 434L-2Cu-0.3NiB-1YAG sample sintered at 1400°C.

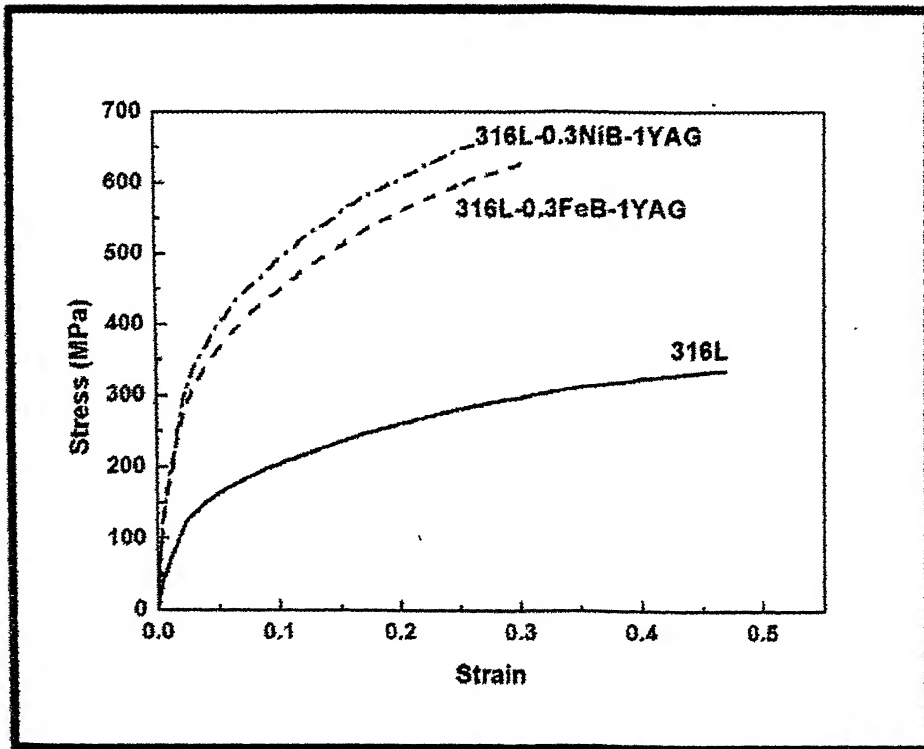


Figure 5.45 Stress-strain curve of 316L samples with additives.

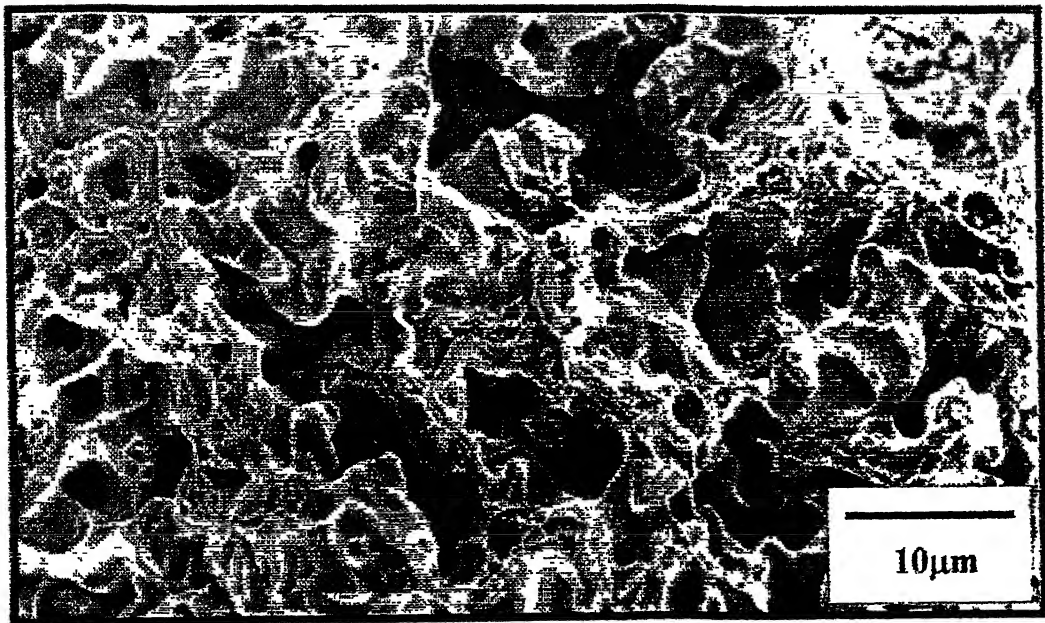


Figure 5.46 SEM micrograph of fracture surface of pure 316L sample sintered at 1400°C.

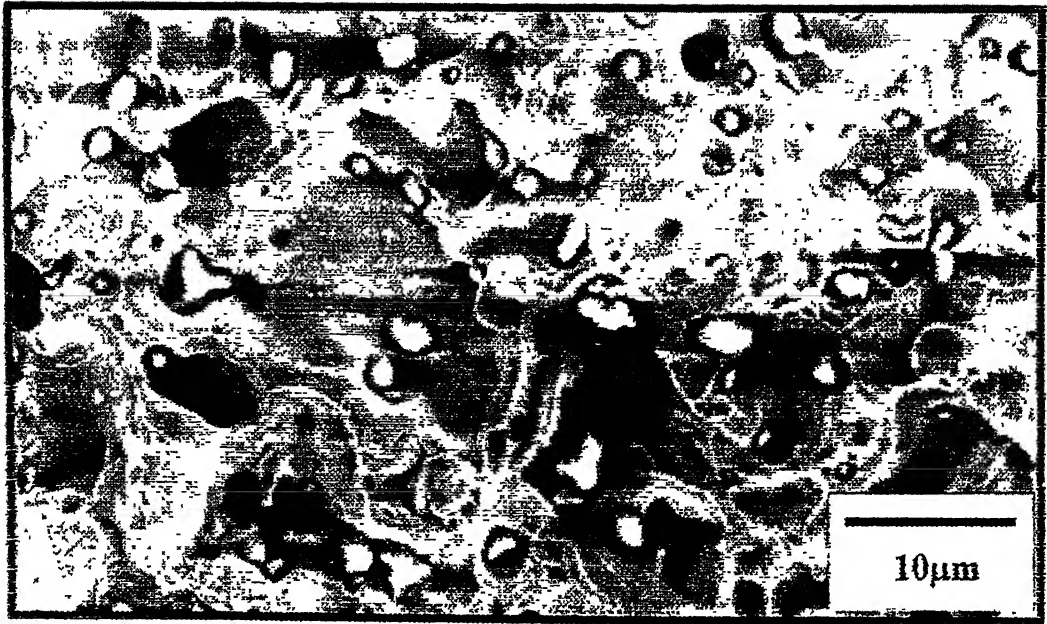


Figure 5.47 SEM micrograph of fracture surface of 316L-0.3FeB-1YAG sample sintered at 1400°C.



Figure 5.48 SEM micrograph of fracture surface of 316L-0.3NiB-1YAG sample sintered at 1400°C.

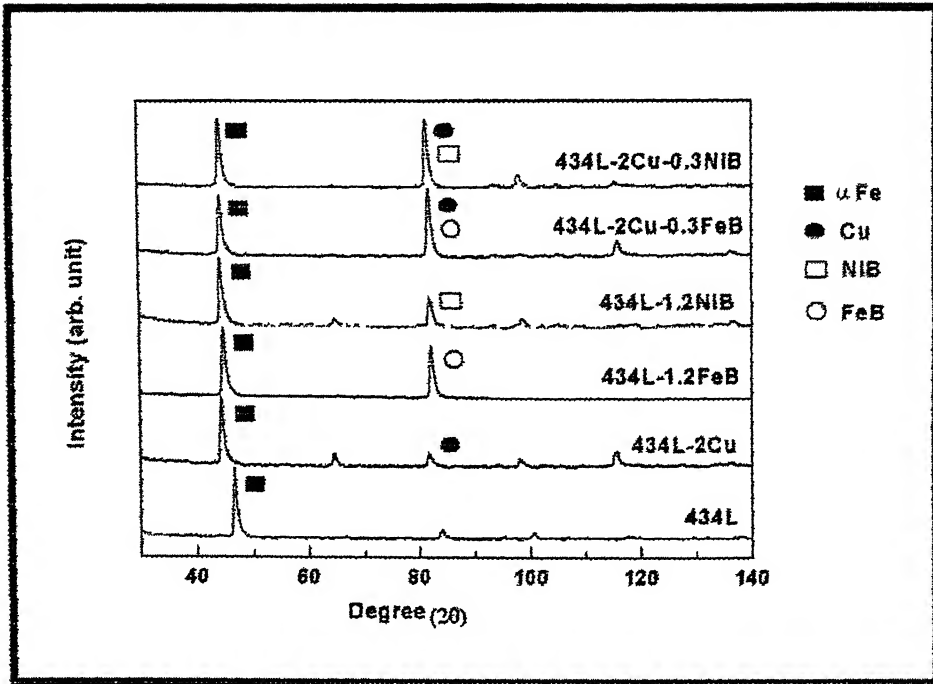


Figure 5.49 XRD plots of 434L samples with additives sintered at 1400°C

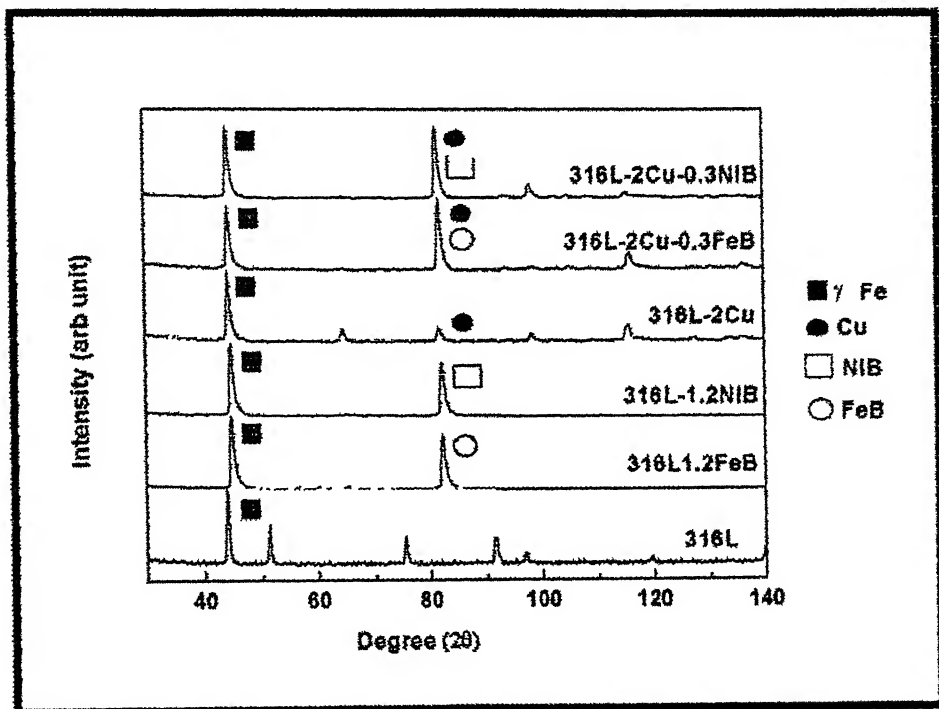


Figure 5.50 XRD plots of 316L samples with additives sintered at 1400°C.

Chapter 6

DISCUSSION

The results obtained in the present work are discussed in this chapter. It contains four sections. The first section summarizes the densification behaviour of the 434L and 316L stainless steel samples with additives, sintered at two different temperatures. It includes sintered density, densification parameter and also axial and radial shrinkage. In the second section microstructural evolution containing optical and SEM micrographs are discussed. In the last section mechanical properties of these samples are analyzed and discussed. It includes bulk hardness, microhardness and tensile properties along with fractography.

6.1 Effect Sintering Temperature and Additives on Densification

Behaviour

6.1.1 Effect of Sintering Temperature

As described earlier, two sintering temperatures 1250 and 1400°C were selected for the present work. The solid state sintering of the samples were carried out at 1250°C for both ferritic and austenitic stainless steel. But in solid state diffusion is very slow process compare to liquid state. So, to enhance the densification another approach was employed by maintaining sintering temperature in between solidus and liquidus temperature. This type of sintering is called Supersolidus Liquid Phase Sintering (SLPS).

The supersolidus liquid phase sintering of the samples was carried out at 1400°C. German *et al* [64] reported the result on supersolidus liquid phase sintering

of austenitic stainless steel with additives. There are two approaches that can be envisaged for achieving full densification in short processing time during SLPS. The first approach is based on utilizing the sintering temperature to nucleate an optimal amount of liquid. In this case particle rearrangement alone can lead to full densification. This approach is applicable to alloys with a wide liquidus-solidus separation (typically $>100\text{ }^{\circ}\text{C}$), for example, 17-4 PH stainless steel. A major drawback of this approach is poor dimensional control arising from the sudden shrinkage experienced by a compact on liquid formation. In addition, if the liquid solidified as a brittle continuous phase along grain boundaries, then mechanical properties decreases so, this approach may not be desirable. The second approach is based on sintering just above the solidus temperature to nucleate a controlled amount of liquid. The amount of liquid is not sufficient to cover all the grain boundaries, yet it is enough to provide faster diffusion path for densification. The amount of liquid is controlled either by the use of additives or by the tight control over the sintering temperature [28]. This approach was utilized in the present study.

6.1.2 Effect of Additives

Of the several sintering aids that have been used for ferrous materials, Copper, Boron, and Ytria Alumina Garnet (YAG) are the most important. Extensive research work has been carried out with copper or boride additions on mostly austenitic stainless steel [51, 52, 59-77]. The effect of Al_2O_3 , Y_2O_3 was also reported [78-84].

Role of Copper

Addition of copper forms liquid phase during sintering in the presently selected sintering temperature. Such an addition markedly increases the sinterability because of faster material transport in liquid phase. Figure 6.1 shows the optical

micrographs of the ferritic stainless steel sample containing 10 wt % Cu along with 0.3 wt. % FeB sintered at 1400°C. From this figure it is clear evident that after crossing the solubility limit excess copper present along the grain boundaries in lenticular shape and the liquid copper which present at grain is spherical in shape. The copper present at grain boundaries is effectively eliminating the pores by liquid formation at sintering temperature.

Copper not only helps for increasing densification but also enhance corrosion resistance properties. But higher amount (greater than 5 wt. %) of copper is detrimental to corrosion resistance property. It is because the dissolution of metallic copper would produce a small surface fraction of active sited from which local dissolution of passive film starts which leads to complete breakdown of passive film. From the Figure 6.1 it is clearly evident this excess copper marked by arrow decreases the corrosion resistance property. So in the present study only 2 wt. % copper was added.

Role of Boron

Here boron was added in the form of boride such as FeB or NiB. Elemental boron is generally avoided because it easily forms oxide which is volatile in nature and causes porosity in the compacts. From the phase diagram of FeB as shown in Figure 2.18 the melting point of FeB is 1650°C. So at 1400°C sintering temperature it does not form liquid. From the phase diagram, it is clearly evident that FeB exhibits a peritectic reaction at 1389°C. It is postulated that FeB aided densification by transforming via boron depletion into Fe₂B, which in turn forms a peritectic liquid at 1174°C. This liquid helps in densification [41]. From the phase diagram of Ni-B as shown in Figure 2.19, it is clearly indicated that sintering is aided by the formation of liquid at 1035°C. This liquid helps in densification enhancement.

Boron is ferrite stabilizer so, when it is added in ferritic stainless steel it helps in densification by peritectic reaction. But when boron is added in austenitic stainless steel it effectively suppress the solidus temperature by destabilizing the austenite and also forms peritectic melts. So effect of boron is more on austenitic stainless steel due to higher amount of liquid formation when the sintering is carried out in SLPS region.

Role of Yttria Alumina Garnet (YAG)

YAG is a hard and brittle refractory material having melting point around 2200°C. When sintering is carried out in SLPS region grain growth is taken place which degrades the mechanical properties. Also due to grain growth intergranular pore become intragranular so sintered density decreases. To restrict this YAG is added. It is preferentially segregated at grain boundaries and pin this. Thus it prevents grain growth. Since the density of YAG (5 g/cm³) is less stainless steel so when it is added 5 wt. % with respect to stainless steel then its volume is high. It preferentially segregates at the grain boundaries and restrict grain boundary sliding and also due to covering of grain boundaries by YAG, the liquid volume fraction at grain boundary region decreases because of solubility of iron and chromium into YAG. Thus sintered density decreases due to lower volume fraction of liquid formation.

6.1.3 Synergistic Effects of Sintering Temperature and Additives

All the stainless steel samples were compacted under 600 MPa optimum pressure [85]. From the Appendices I and II for ferritic stainless steel samples, it is clearly evident that sintered density increases as temperature of sintering increases from 1250 to 1400°C. It is not only because of increasing diffusivity at 1400°C but also at 1400°C, sintering was taking place in the supersolidus region i.e. between solidus and liquidus temperature. To increase densification copper, FeB and NiB were

added. From Figure 5.1 it is clearly evident that only borides are not so much effective for increasing densification. It is because of very lower volume fraction of liquid. By the addition of 2 wt. % copper, sintered density increases 85 % theoretical to 92 % theoretical as temperature of sintering increases from 1250 to 1400°C. It is due to liquid formation by copper and liquid at grain boundaries due to sintering at supersolidus region. Maximum densification occurs in the samples containing copper along with FeB or NiB. The reason for this is the three sources of liquid, such as liquid contributed by copper, peritectic melt formation by FeB or melt formation by NiB and liquid at grain boundary region. Similar trend was also obtained for densification parameter of these samples as shown in Figure 5.2. The axial and radial shrinkage was also higher in 1400°C sintering temperature. As shown in Figures 5.5 and 5.6 the deviation from ideal behaviour took place because of formation of density contour during single action pressure.

For austenitic stainless steel, densification increases as sintering temperature increases from 1250 to 1400°C. It occurs due to increasing diffusivity and sintering at supersolidus region. Figure 5.3 shows that only 2 wt. % copper was not effective for densification, because the solubility of copper into austenite is about 9 wt. %. So the liquid copper must here gone into solid solution because of transient liquid phase sintering at 1400°C. However, only 0.3 wt. % boride was sufficient to get near theoretical density. This is because of the presence of boride which significantly lowers the solidus temperature of austenitic stainless steel by destabilising the austenite, because boride is ferritic stabiliser. Due to this reason higher volume fraction of liquid formation occurs in supersolidus region as compare to ferritic stainless steel. In this case by addition of boride 97% theoretical density was obtained. Combined effect of copper and boride was not effective, because copper is an

austenitic stabiliser, so the effect of boride is suppressed. Similar trends were also obtained for densification parameter and in axial and radial shrinkage of the samples as shown in Figures 5.4, 5.7, 5.8.

For both the stainless steel, YAG addition was effective in increasing densification along with other additives. Because YAG is a refractory material; it remains in solid state at sintering temperatures. This solid particle helps as a short circuiting path for diffusion by maintaining bridge between two solid stainless steel particles. This is clearly shown in Figures 5.1 and 5.2 for sintered density and densification parameter respectively for ferritic stainless steel and Figure 5.3 and 5.4 for austenitic stainless steel.

6.2 Evolution of Microstructure

Figures 5.9 and 5.32 show the optical and SEM micrographs of pure 434L compacts sintered at 1250 and 1400°C. In 434L compact sintered at 1250°C, the pores were found to be mostly intergranular. In contrast, pores were mostly intragranular when sintering was done at 1400°C. At 1250°C, the 434L compacts are solid-state sintered. Consequently, the rate of diffusion is relatively slower at 1250°C as compared to sintering at 1400°C. However, rate of coarsening of 434L grains is higher than the rate of pore removal. This causes the intergranular pores to gradually become intragranular. Removal of the intragranular porosity is more difficult (as compared to intergranular pores) because it involves volume diffusion. Figure 6.2 represents how the intergranular pore becomes intragranular due to grain growth.

At 1250°C, 434L stainless steel undergoes solid-state sintering, whereas 434L-2Cu gets conventionally liquid phase sintered as shown in Figure 5.10. Note that there is no significant effect of copper at 1250°C. This is attributed to the relatively lower

amount of liquid copper melt (1.8 volume percent), which is insufficient to cause densification by capillary-induced grain rearrangement. In addition to good wettability the Fe-Cu system also has low dihedral angle ($<5^\circ$). At sintering temperature copper melt penetrate the grain boundary of stainless steel skeleton. Thus in the sintered microstructure some irregular large pores (called secondary pores) are observed that can be attributed to the particle location prior to melting. These features are captured in the optical micrograph and SEM in Figures 5.11 and 5.34 by arrow mark. In the intergranular region at 1250°C only traces of copper melt are seen. However, at 1400°C (SLPS), the intergranular region consists of Cu-melt and partially melted 434L stainless steel. It is difficult to distinguish completely the melt in intergranular region which contain both stainless steel and copper. The intragranular melt is solely being contributed by part of 434L stainless steel liquid nucleating at defect region within the grain. It is captured in SEM micrograph as shown in Figure 5.34(b) as white spots within grain marked by arrow.

The addition of boron as FeB leads to the formation of continuous network of precipitates along the grain boundaries. From phase diagram of Fe-B as shown in Figure 2.18, it is evident that FeB exhibits a peritectic reaction at 1389°C . FeB aided densification by transforming into boron depleted phase Fe_2B , which in turn forms a peritectic liquid at 1174°C . This liquid helps for densification. In ferritic stainless steel maximum density (91 % of theoretical) was obtained at 1400°C with 0.9%FeB, beyond that the density remains constant, because mostly intragranular pores present. Figures 5.12 and 5.13 show the effect of 0.9wt% FeB addition on 434L stainless sintered at 1250 and 1400°C . For increasing densification, diffusion through grain required, which was a slow process.

By NiB addition maximum density (90 % of theoretical) was obtained. From phase diagram of Ni-B as shown in Figure 2.19, it is clearly indicated that sintering is aided by the formation of transient liquid via a peritectic reaction at 1035°C. This liquid helps in densification enhancement.

Maximum densification occurs when both copper and boride additives used together due to their synergistic effect. In this case 93% of theoretical density was achieved in the sample containing 2 wt. % copper and 0.3 wt. % NiB sintered at 1400°C. Figures 5.14 and 5.15 show the optical micrographs of the samples sintered at 1250 and 1400°C, respectively. The sample containing copper along with FeB shows maximum of 94% theoretical density. As compared to NiB, FeB is much more effective for densification because of formation of peritectic melt. The optical micrographs of the samples containing 2 wt. % copper and 0.3 wt. % FeB sintered at 1250 and 1400°C as shown in Figures 5.16 and 5.17 respectively. Figures 5.35 and 5.36 show the SEM micrographs of the same samples sintered at 1250 and 1400°C, respectively. From XRD pattern analysis of 434L samples with additives no new phase was found.

Similar grain growth trend also occurs in the austenitic stainless steel samples as sintering temperature increases from 1250 to 1400°C. So intergranular pores become intragranular due to the slower rate of pore removal compared to the grain growth. Figures 5.20 and 5.21 show the optical micrographs of the pure 316L samples sintered at 1250 and 1400°C respectively.

Only 2 wt. % copper is not sufficient to enhance densification. Because this much amount of copper will easily go into solid solution. So pores were present along the grain boundaries even at 1400°C temperature also. At this sintering temperature copper forms transient liquid phase because of higher (9 wt. %) solubility of copper

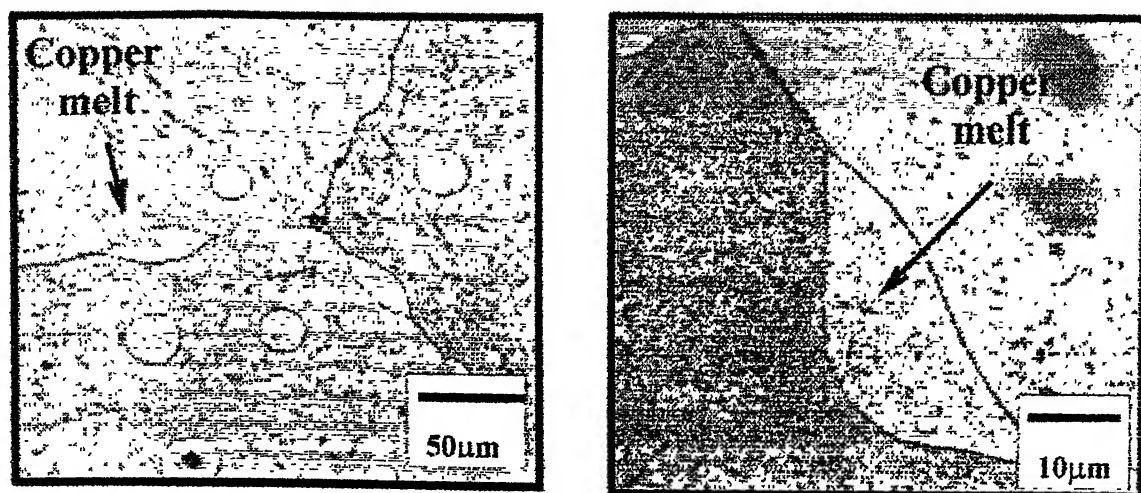


Figure 6.1 Optical micrographs of 434L-10Cu-0.3FeB sample sintered at 1400°C (a) lower (b) higher magnification.

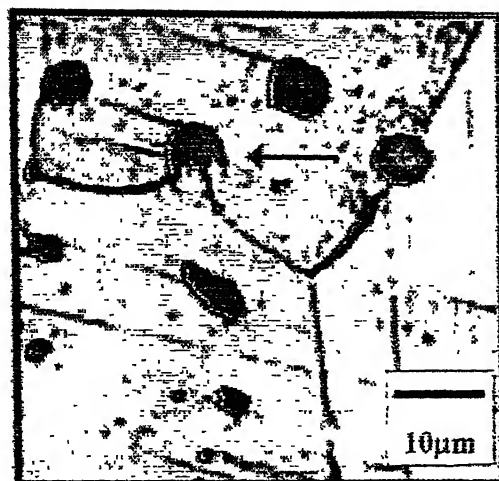


Figure 6.2 Optical micrograph showing the transformation of intergranular pores to intragranular type.

into austenite. These features are captured in Figures 5.22 and 5.23 sintered at 1250 and 1400°C respectively.

Borides are not effective when sintering was done at 1250°C because it was a conventional solid state sintering. So pores were mostly intergranular. This feature has been captured in Figures 5.24 and 5.25 of the samples containing 0.3 wt. % FeB and NiB, respectively. However, near theoretical density was obtained when sintering was done at 1400°C. In this temperature FeB forms peritectic liquid and NiB forms liquid by melting. Another most attractive result is boride effectively suppresses the solidus temperature, so higher volume fraction liquid was obtained at 1400°C. This liquid mostly forms along grain boundaries and in grain with defects. Figures 5.26 and 5.27 show the optical micrographs of the samples containing 0.3 wt. % FeB and NiB respectively.

Combined addition of copper along with boride was not effective in enhancing densification. It is because copper is austenite stabilizer so it suppresses the effect of boride i.e. it prevents the suppression of solidus line. Figures 5.28 and 5.29 show optical micrographs of the samples containing 0.3 wt. % FeB and NiB along with 2 wt. % copper, respectively.

Main disadvantage of SLPS is grain growth. To suppress this some refractory material such as Yttria Alumina Garnet (YAG) was added. It prevents the grain growth by pinning the grain boundaries and thus prevents pores to be intragranular. Figures 5.18 and 5.19 show the optical micrographs of the 434L-2Cu samples containing 1 wt. % YAG along with 0.3 wt. % FeB and NiB, respectively. From these micrographs it is clearly evident that only 1 wt. % YAG was sufficient to restrict grain growth. As shown in Figures 5.30 and 5.31 similar trend was also obtained in 316L samples containing 1 wt. % YAG along with 0.3 wt. % FeB and NiB respectively.

6.3 Evolution of Mechanical Properties

6.3.1 Bulk hardness

434L stainless steel samples with additives bulk hardness increases as sintering temperature increases from 1250 to 1400°C. It is because of increasing densification. The contribution of boride in increasing hardness is less as compared to synergistic effect of copper and borides. It is due to very lower amount of melt formation that occurs in the boride samples. Hardness of these samples is shown in Figure 5.37 as a function of sintering temperature.

Figure 5.38 shows the bulk hardness of the 316L samples with additives. In this case also a similar trend was also obtained in the sense that hardness increases as sintering temperature increases from 1250 to 1400°C. In 316L stainless steel samples maximum hardness were obtained in the samples containing 0.3 wt % boride. It is because boride helps to suppress the solidus temperature and thus higher volume fraction of liquid is obtained at supersolidus region sintering temperature which helps in densification. The samples of 316L stainless steel with copper additives show higher hardness as compared to pure 316L. It is because copper forms solid solution in austenite, increasing the hardness.

Maximum hardness was obtained in the samples containing YAG. It is because YAG is a hard and brittle refractory material, so it shows higher hardness. The 316L samples with additives show higher hardness due to the higher sintered density compared to 434L samples with additives.

6.3.2 Microhardness

In 434L-2Cu samples hardness varies in different regions, because copper rich region shows lower hardness as compared to pure 434L region. But by the addition of

boride, hardness increases at grain boundary region as compared to grain. Figure 5.39 represents the microhardness values of 434L samples with additives. When FeB or NiB added it forms a continuous network of precipitate along grain boundaries. Figure 5.40 shows the above results. Due to addition of YAG values of microhardness increases for both the stainless steel samples. It is because of presence of hard and brittle YAG phase.

6.3.3 Tensile Properties

The main drawback of SLPS is grain growth. So when sintering was done at 1400 °C grain growth occurred. Due to the grain growth mechanical properties such as tensile strength decreases drastically. To restrict this some Yttria Alumina Garnet (YAG) was added which pin the grain boundaries and restrict the grain growth. The amount of YAG was restricted to 1 wt. % because the YAG molecules would preferentially segregate at grain boundaries and make it brittle, so the ductility decreases drastically.

Table 5.1 represents the tensile properties of some samples of selected compositions. These compositions were chosen because these possess maximum sintered density as compared to other compositions. Figure 5.41 compares the engineering stress-strain curves of pure 434L sample and 434L samples with additives. Copper and borides were added to increase the densification and YAG was added to restrict grain growth. Strength increases because of increase of sintered density of the samples and also due to smaller grain size. Figure 5.42 shows the fractograph of pure 434L samples. It was a mixed mode of fracture having ductility 30%. In ductile mode *dimpled rupture* was characterized by cup like depression. Microvoids were initiated at second phase or pores, the voids grew, and the ligaments

between microvoids fractured. In brittle mode *river marking* were obtained. The river marking are caused by the crack moving through the crystal along a number of parallel planes which form a series of plateaus and connecting ledges. These are indications of the absorption of energy by local deformation. The direction of river pattern represents the direction of crack propagation [86]. Figure 5.43 shows the fractograph of 434L samples containing 2 wt. % copper, 0.3 wt. % FeB and 1 wt. % YAG. In this case pores are the root of the crack formation. Similar trend was also obtained in 434L samples containing 2 wt. % copper, 0.3 wt. % NiB and 1wt% YAG. In these cases ductility decreases up to 16%. So the fracture surface show the mostly river pattern as shown in Figure 5.44.

Figure 5.45 compares the engineering stress-strain curves of pure 316L sample and 316L samples with additives. Only 0.3 wt. % boride was sufficient to increase the strength along with 1 wt. % YAG. It is because of suppression of solidus line by boride and smaller grain size due to presence of YAG particles. The Fractographs of 316L samples with additives show mostly ductile mode of fracture which is characterized by *dimpled rupture* as shown in Figures 5.46 to 5.48. Even though there has been grain coarsening taken place because of high sintering temperature and residual porosity, as compared to solid state sintering SLPS results higher ductility in 316L samples with additives. This is reflected predominantly dimpled morphology of fracture surface. The presence of residual pores does not detrimentally affect the ductility because these pores are primarily intragranular type.

Chapter 7

CONCLUSIONS

From the present study it can be concluded that

- (i) Higher density in P/M stainless can be obtained by supersolidus liquid phase sintering due to homogeneous melt formation in both ferritic and austenitic stainless steel.
- (ii) Further densification enhancement can be achieved through alloying additions. Addition of 2 wt. % Cu enhances the densification of ferritic stainless steel at 1400°C. The densification is attributed to the Cu melt penetration which causes better grain rearrangement
- (iii) Only 2 wt. % Cu addition is not sufficient for enhancing densification because of higher solubility of Cu into austenite.
- (iv) Boron addition as NiB and FeB was found to be effective for densification of ferritic stainless steel provided it is added along with copper. It occurs due to the synergistic action of the alloying elements.
- (v) Only 0.3 wt% FeB or NiB is sufficient for achieving near theoretical density in austenitic stainless steel. Because boride effectively suppresses the solidus temperature, higher volume fraction liquid is obtained at 1400°C sintering temperature.
- (vi) Hardness increases as sintering temperature increases from 1250 to 1400°C for both ferritic and austenitic stainless steels.
- (vii) For both ferritic and austenitic stainless steels, tensile strength increases due to the synergistic effect of increasing densification by addition of additives and reduction of grain size by addition of yttria alumina garnet.

REFERENCES

- 1 E Klar and P.K. Samal, "Powder Metallurgy of Stainless Steels," ASM Handbook, v 7, pp. 174-185
2. G S Upadhyaya, Sintered Metallic and Ceramic Materials Preparation, Properties and Applications, John Wiley Publishing, NY, USA, 1999.
3. R Tandon and R.M. German, "Sintered and mechanical properties of boron doped austenitic stainless steel," *International Journal of Powder Metallurgy*, 1998, v 34, n. 1, pp. 40- 49.
- 4 D A Jones, Principles and Prevention of Corrosion, Maxwell Macmillan International Editions, NY, USA, 1992.
5. T. B. Massalski, and C.S. Barrett., Binary Alloy Phase Diagrams, 2nd edition, ASM International, Materials Park, OH, 1990.
6. W. F. Smith, "Stainless Steel," Structure and Properties of Engineering Alloys, McGraw Hill Inc., NY, USA, pp. 289-334.
- 7 www.cyberbuzz.gatech.edu
8. J. R. Davis, "Introduction to Stainless Steels," ASM Specialty Handbook: Stainless Steel, Davis & Associates (eds.), pp. 4-38.
9. www.spiusa.com
10. www.materialsengineering.com
11. www.pwlnetcom.com
12. www.mpif.org
13. F. Thumler and R. Oberacker, An Introduction to Powder Metallurgy, The Institute of Materials, New York, USA, 1993.
14. R.M. German, Powder Metallurgy of Iron and Steel, John Wiley Publishing, NY, USA, 1998.

15. J. S. Hirschhorn, Introduction to Powder Metallurgy, American Powder Metallurgy Institute, Princeton, NJ, USA, 1990
16. R. M. German, Sintering Theory and Practice, John Wiley and Sons, Inc., New York, USA, 1996.
17. R.M. German, Powder Metallurgy Science, Metal Powder Industrial Federation, Princeton, NJ, USA, 1994
18. S. Ghosh, "Processing of Premix and Prealloyed Bronze through Transient and Supersolidus Liquid Phase Sintering," M Tech Thesis, IIT Kanpur, 2001.
19. R M German, "Some Sources of Activation Energy Errors in Sintering Experiments," *Powder Metallurgy*, 1979, v 22, pp.29-30.
20. R.M. German, Liquid Phase Sintering, Plenum Press, NY,USA, 1985.
21. J W. Huppmann, H. Riegger, W.A. Kaysser, V. Smolej, and S. Pejovnik, "Elementary Mechanisms of Liquid Phase Sintering," *Zeitschrift fur Metallkunde*, 1979, v. 70, n 11, pp 707-713
22. W. Kehl and H.F. Fischmeister, "Liquid Phase Sintering of Al-Cu Compacts," *Powder Metallurgy*, 1980, v 23, pp 113-119.
23. D.J. Lee and R.M. German, "Sintering Behaviour of Iron Aluminium Powder Mixes," *International Journal of Powder Metallurgy*, 1985, v. 21, pp 9-21.
24. R.M. German, "Phase Diagrams in Liquid Phase Sintering Treatments," *Journal of Metals*, 1986, v. 38, n 8, pp 26-29
25. Y. Zhou, W.F. Gale, and T.H. North, "Modelling of Transient Liquid Phase Bonding," *International Materials Reviews*, 1995, v. 40, n. 5, pp. 181-195.
26. www.tlptechnologies.com
27. S.F. Corbin and P. Lucier, "Thermal Analysis of Isothermal Solidification Kinetics during Transient Liquid-Phase Sintering," *Metallurgical and Materials*

- Transactions*, 2001, v. 32A, n. 4, pp. 971-978.
- 28 R. Tandon, "Densification Mechanisms and Microstructural Evolution Leading to High Density Processing of Prealloyed Powders in Supersolidus Liquid Phase Sintering," PhD Thesis, The Pennsylvania State University, USA, 1995
29. R.M. German, "Supersolidus Liquid Phase Sintering, Part I: Process Review," *International Journal of Powder Metallurgy*, 1990, v. 26, pp. 23-33.
30. R.M. German, "Quantitative Theory for Supersolidus Liquid Phase Sintering," *Powder Metallurgy*, 1991, v. 34, pp. 101-107.
31. E.J. Westerman, "Sintering of Ni-based Superalloys," *Transaction AMIE*, 1962, v. 224, pp.159-164.
32. J.A. Lund and S.R. Bala, "Supersolidus Sintering," Modern Developments in Powder Metallurgy, H.H. Hausner and W.E. Smith (eds.), Metal Powder Industries Federation, Princeton, NJ, 1974, v. 6, pp. 409-421.
33. R. Tandon and R.M. German, "Supersolidus-Transient Liquid Phase Sintering Using Superalloy Powders," *International Journal of Powder Metallurgy*, 1994, v. 30, pp.435-443
34. A. Lal, "Mechanisms and Mechanics of Shape Loss During Supersolidus Liquid Phase Sintering," PhD Thesis, The Pennsylvania State University, USA, 1999.
35. A. Lal, R. Iacocca and R.M. German, "Densification during Supersolidus Liquid Phase Sintering of Nickel-base Prealloyed Powder Mixtures," *Materials and Metallurgical Transactions*, 1999, v. 30, n. 8, pp. 2201-2208.
36. R.M. German, "Advances in High Alloy Sintering Using Supersolidus Liquids," Advances in Powder Metallurgy and Particulate Materials, 1997, v. 2, pp. 143-148.
37. Y. Liu, R. Tandon, and R.M. German, "Modeling of Supersolidus Liquid Phase

- Sintering I Capillary Force," *Metallurgical and Materials Transactions*, 1995, v. 26, n. 9, pp. 2415-2422
38. Y. Liu, R. Tandon, and R.M. German, "Modeling of Supersolidus Liquid Phase Sintering II Densification," *Metallurgical and Materials Transactions*, 1995, v. 26, n. 9, pp. 2423-2430.
39. R. M. German, "Supersolidus Liquid Phase Sintering Part-2; Densification Theory," *International Journal of Powder Metallurgy*, 1990, v. 26, pp. 35-40
40. R. Tandon, Y. Liu, and R.M. German, "Application of Supersolidus Liquid Phase Sintering to High Density Processing of Prealloyed Powder," Advances in Powder Metallurgy and Particulate Material, 1995, v. 25, n.3, pp. 135-140.
41. R. Tandon. and R.M. German, "Sintered and Mechanical Properties of a Boron Doped Austenitic Steel," *International Journal of Powder Metallurgy*, 1998, v. 34, n. 1, pp. 40-49.
42. A.K. Mashkov and V.V. Chernienko, "Eutectic containing iron boride materials," *Poroshkovaya Metallurgiya*, 1973, n. 8, pp. 59-62.
43. S.K. Banerji and J.E. Moral, "Boron in Steel," TMS-AIME Proceeding, Warrendale, 1980, pp. 106-110.
44. J. Klien, "A Preliminary Investigation of Liquid Phase Sintering in Ferrous Base Ststem," Report LBL-3549, Lawrence Berkeley Laboratory, University of California, Berkeley, CA, 1975.
45. D.S Madan and R.M. German, "Enhanced Sintering for Ferrous Components," *Metal Powder Industries Federation*, 1984, v. 15, pp. 441-454.
46. R.M German and K.A. D' Angelo, "Enhanced Sintering Treatment for Ferrous Powders," *International Metals Review*, 1984, v. 29, n. 4, pp. 3939-3944.
47. E. Dudrova, M. Selecka, R. Bures, and M. Kabatova, "Effect of Boron Addition

- on the Microstructure and Properties of Sintered Fe-1.5Mo Powder materials," *ISIJ*, 1997, v. 37, n. 1, pp 59-64.
- 48 M. Coubiere, P. Faure, F. Jean, and L. Ackerman, "Activated Sintering of Steel Through the Presence of Liquid Phases," Advances in Powder Metallurgy and Particulate Material, 1992, v. 3, pp 57-71.
49. L. Xiu, B. Uhrenius, A. Salwen, and L. Hultman, "Effect of Fe-B and Fe-C Master Alloy Powder on the Liquid Phase Sintering of Fe-Mo-B-C Steel," NTIS Report, 1995.
- 50 P. Villars, A. Prince, and H. Okamoto, Handbook of Ternary Alloy Phase Diagrams, ASM International, Material Park, OH, USA, 1995.
51. E.R. Lumpkins, "A Theoretical Review of the Copper Infiltration of P/M Components," *Powder Metallurgy International*, 1985, v 17, n.3, pp 120-128.
52. H. Danninger, "Pore Formation during Sintering of Fe-Cu and its Effects on Mechanical Properties," *Powder Metallurgy International*, 1987, v 19, n.1, pp. 19-23.
53. R. Tandon, Y. Liu, and R.M. German, "High Density Processing of Ferrous Alloys via Supersolidus Liquid Phase Sintering," Advances in Powder Metallurgy and Particulate Materials, 1995, v. 5, pp. 5 23-5.36.
54. N.E. Solovev, V.S. Makarov, L.N. Meshchaninova, and Y.A. Ugai, "Interaction of Oxides of Transition Elements with Boron," *Journal of Alloys and Compounds*, 1992, v. 17, pp. 131-138.
- 55 H.S. Canon and F.V. Lenel, "Some Observations on The Mechanism of Liquid Phase Sintering," Plansee Proceedings, F. Benesovsky (eds.) Plansee Metalwerk, Reutte, Austria, 1953, pp. 106-112.

56. M. Rosso, J. K. Baczevska, and T. Pieczonka, "Properties of High Molybdenum Iron Alloys Modified with Boron," Advances in Powder Metallurgy and Particulate Materials, 1999, v. 7, pp. 7.23-7.34.
57. D.S. Madan and R.M. German, "Structure Property Relationship in Iron Compacts Alloyed with Boron," Advances in Powder Metallurgy and Particulate Materials, 1989, v. 1, pp. 147-161.
58. A. Molinari, J. Kazior, G. Straffelini, and T. Pieczonka, "Persistent Liquid Phase Sintering of 316L Stainless steel," *International Journal of Powder Metallurgy*, 1998, v. 34, n. 2, pp. 21-28.
59. A. Tiziani, A. Molinari, L. Fedrizzi, A. Tomasi, and P.L. Bonora, "Liquid Phase Sintering of AISI 316L Stainless Steel," *Powder Metallurgy*, 1989, v. 32, n. 2, pp. 118-122.
60. W.F. Wang and Y.L. Su, "Liquid Phase Sintering of Austenitic Stainless Steel Powders with Silicon Additives," *Powder Metallurgy*, 1986, v. 29, n.4, pp. 269-275.
61. R.M. German, "The Production of Stainless Steels by Injection Moulding Water Atomised Prealloy Powders," *Journal Injection Moulding Technique*, 1997, v. 1, n.3, pp. 171-179.
62. A. Sharon, N. Melman, and D. Itzhak, "Corrosion Resistance of Sintered Stainless Steel Containing Nickel Based Additives," *Powder Metallurgy*, 1994, v.37, n.4, pp.67-71.
63. R. Tandon and R.M. German, "Sintered and Mechanical Properties of a Boron Doped Austenitic Steel," *International Journal of Powder Metallurgy*, 1998, v. 34, n. 1, pp. 40-49.
64. R. Tandon and R.M. German, "Particle Fragmentation during Supersolidus

- Sintering," *International Journal of Powder Metallurgy*, 1997, v. 33, n. 1, pp. 54-60.
65. K.D. Christian and R.M. German, "Relation between Pore Structure and Fatigue Behavior of Sintered Iron Copper Carbon," *International Journal of Powder Metallurgy*, 1995, v. 31, n. 1, pp. 51-60.
66. H.I. Bakan, D. Heaney, and R.M. German, "Effect of Nickel Boride and Boron Additives on Sintering Characteristics of Injection Moulded 316L Powder Using Water Soluble Binder System," *Powder Metallurgy*, 2001, v. 44, n. 3, pp. 235-242.
67. F. Velasco, J.M. Torralba, J.M.R. Roman, L.E.G. Cambronero, and J.M.R. Prieto, "Effect of Infiltration on the Mechanical Properties and Corrosion Resistance of Austenitic Stainless Steel," *International Journal of Powder Metallurgy*, 1995, v. 31, n. 4, pp. 309-315.
68. T.M. Puszcz, A. Molinari, J. Kzior, T. Pieczonka, and M. Nykiel, "Sintering Transformation in Mixture of Austenitic and Ferritic Stainless Steel Powder," *Powder Metallurgy*, 2001, v. 44, n. 1, pp. 48-52.
69. J. Liu, R.M. German, and A. Cardamone, "Estimation of Capillary Pressure in Liquid Phase Sintering," *Powder Metallurgy*, 2001, v. 44, n. 4, pp. 317-324.
70. R.M. Anklekar, D.K. Agrawal, and R. Roy, "Microwave Sintering and Mechanical Properties of P/M Copper Steel," *Powder Metallurgy*, 2001, v. 44, n. 4, pp. 355-362.
71. J.K. Baczewska and M. Rosso, "Effect of Boron on Microstructure and Mechanical Properties of Powder Metallurgical Sintered and Nitrided Steel," *Powder Metallurgy*, 2001, v. 44, n. 3, pp. 221-227.
72. T.M. Puszcz, A. Molinari, J. Kzior, T. Pieczonka, and M. Nykiel, "Density and Microstructure of Duplex Stainless Steel Produced by Mixture of Austenitic and

- Ferritic Powders," Proceeding of 2000 Powder Metallurgy World Congress, EPMA, Shoewsbury, UK, 2000, Part-2, pp 980-983.
73. M. Rosso, M.A. Grande, and D. Ornato, "Sintering of Duplex Stainless Steel and their Properties," *Powder Metallurgy Progress*, 2002, v. 2, n. 1, pp. 10-17
74. J. Liu, R.M. German, A. Cardamone, T. Potter, and T.J. Semel, "Boron Enhanced Sintering of Iron Molybdenum Steels, *International Journal of Powder Metallurgy*, 2001, v. 37, n. 5, pp. 39-46.
75. J. Liu, R.M. German, A. Cardamone, T. Potter, and T.J. Semel, "Liquid Phase Sintering of Iron Carbon Alloy with Boron Addition," *Powder Metallurgy*, 2000, v. 43, n. 1, pp. 57-62.
76. H. Kuroki, G. Han, and K. Shinozaki, "Solution Reprecipitation Mechanism in Fe-Cu-C during Liquid Phase Sintering," *International Journal of Powder Metallurgy*, 1999, v. 35, n. 2, pp. 57-62.
77. F. Marchetti, A. Molinari, J. Kazior, R. Canteri, I. Cristofolini, and A. Tiziani, "Sintering Mechanism of Boron Alloyed AISI 316L Stainless Steel," *Powder Metallurgy*, 1994, v. 37, n. 2, pp. 115-120.
78. S. Lal, "Sintering of 316L Austenitic Stainless Steel- Y_2O_3 Particulate Composites," PhD Thesis, Indian Institute of Technology, Kanpur, 1988.
79. S. Lal and G.S. Upadhyaya, "Sintering of Stainless Steel and Their Based Composites," *Review on Powder Metallurgy and Physical Ceramics*, 1986, v. 3, n. 2, pp. 165-203.
80. S. Lal and G.S. Upadhyaya, "Effect of Y_2O_3 Addition and Sintering Period on the Properties of P/M 316L Austenitic Stainless Steel," *Journal of Materials Science Letters*, 1987, v. 6, pp. 761-764.
81. S.K. Mukherjee, "Sintering of 434L Ferritic Stainless Steel- Al_2O_3 Particulate

- Composites," PhD Thesis, Indian Institute of Technology, Kanpur, 1984.
82. S K. Mukherjee and G S. Upadhyaya, "Sintering of 434L Ferritic Stainless Steel Containing Al_2O_3 Particles," *International Journal of Powder Metallurgy and Powder Technology*, 1983, v 19, pp.289.
83. S.K. Mukherjee and G.S. Upadhyaya, "Sintering of Ferritic Stainless Steel- Al_2O_3 Particulate Composites," *Journal of Powder and Bulk Solid technology*, 1983, v 7, pp. 27.
84. S.K. Mukherjee and G.S. Upadhyaya, "Sintered 434L Ferritic Stainless Steel- Al_2O_3 Particulate Composites Containing Phosphorous," *High Temperature Technology*, 1983, v. 1, pp. 223.
85. J. Shankar, "Sintering and Electrochemical Characterization of Ytria Dispersed Austenitic and Ferritic Stainless Steels," M.Tech Thesis, IIT Kanpur, 2001.
86. G. E. Dieter, Mechanical Metallurgy, McGraw-Hill Book Company, London, UK, 1988.

Appendix-I

Experimental data for green samples of 434L and with additives before sintering at 1250°C

Composition (wt%)	Height (cm)	Weight (gm)	Diameter (cm)	Density (g/cm ³)	Density (% Theoretical)
434L	0.708	2 1067	0 806	5 83	73 30
434L-0.3FeB	0 804	2 3862	0 806	5.81	73.17
434L-0.6FeB	0 796	2 4232	0 806	5 97	75 06
434L-0.9FeB	0.546	1 6412	0 806	5 89	74 13
434L-1.2FeB	0.75	2 249	0.806	5.88	73 96
434L-0.3NiB	0 703	2 3862	0 806	5.81	73.17
434L-0.6NiB	0.648	1.9690	0 806	5.96	74 92
434L-0.9NiB	0.678	2.0278	0 806	5 86	73.76
434L-1.2NiB	0.566	1 7465	0 806	6.05	76 11
434L-2Cu	0 685	2 1098	0 806	6.04	76 65
434L-2Cu-0.3FeB	0.537	1 6751	0 806	6 11	77 54
434L-2Cu-0.3NiB	0.673	2.0924	0.806	6.09	77.28

Experimental data for the samples of 434L and with additives after sintering at 1250°C

Composition (wt%)	Height (cm)	Weight (cm)	Diameter (gm)	Density (g/cm ³)	Density (% Theoretical)	Weight Loss (%)	Densification Parameter
434L	0.678	2.0784	0.766	6.65	84.60	1.34	0.40
434L-0.3FeB	0.762	2.3553	0.764	6.72	85.75	1.29	0.43
434L-0.6FeB	0.770	2.3932	0.768	6.71	85.37	1.24	0.37
434L-0.9FeB	0.524	1.6175	0.766	6.70	85.33	1.44	0.39
434L-1.2FeB	0.710	2.2161	0.760	6.88	87.64	1.46	0.48
434L-0.3NiB	0.692	2.0937	0.750	6.85	87.15	1.63	0.51
434L-0.6NiB	0.618	1.9405	0.764	6.85	87.23	1.45	0.47
434L-0.9NiB	0.646	2.0022	0.766	6.73	85.72	1.26	0.41
434L-1.2NiB	0.550	1.7248	0.768	6.77	86.24	1.24	0.38
434L-2Cu	0.669	2.0821	0.774	6.61	83.89	1.32	0.31
434L-2Cu- 0.3FeB	0.526	1.6493	0.772	6.70	85.03	1.54	0.33
434L-2Cu- 0.3NiB	0.660	2.0612	0.771	6.69	84.89	1.49	0.34

Appendix-II

Experimental data for green samples of 434L and with additives before sintering at 1400°C

Composition (wt%)	Height (cm)	Weight (gm)	Diameter (cm)	Density (g/cm ³)	Density (% Theoretical)
434L	0.858	2.5485	0.806	5.82	73.17
434L-0.3FeB	0.956	2.8313	0.806	5.81	73.01
434L-0.6FeB	0.558	1.658	0.806	5.83	73.20
434L-0.9FeB	0.548	1.6522	0.806	5.91	74.33
434L-1.2FeB	0.560	1.6597	0.806	5.81	73.07
434L-0.3NiB	0.834	2.5099	0.806	5.90	74.19
434L-0.6NiB	0.496	1.4898	0.806	5.89	73.82
434L-0.9NiB	0.492	1.4841	0.806	5.92	74.15
434L-1.2NiB	0.506	1.5225	0.806	5.91	74.11
434L-2Cu	0.471	1.4386	0.806	5.99	76.02
434L-2Cu-0.3FeB	0.580	1.8359	0.806	6.20	78.68
434L-2Cu-0.3NiB	0.602	1.8792	0.806	6.12	77.66
434L-2Cu-0.3FeB- 1YAG	0.716	2.3318	0.806	6.38	81.48
434L-2Cu-0.3NiB- 1YAG	0.553	1.8104	0.806	6.42	81.99

Experimental data for the samples of 434L and with additives after sintering at 1400°C

Composition (wt%)	Height (cm)	Weight (gm)	Diameter (cm)	Density (g/cm ³)	Density (% Theoretical)	Weight Loss (%)	Densification Parameter
434L	0.804	2 5087	0.746	7 14	90 84	1 56	0 62
434L-0.3FeB	0.900	2 7900	0.752	6.98	88 79	1 46	0.55
434L-0.6FeB	0.526	1 6477	0 750	7 09	90 21	0 62	0.59
434L-0 9FeB	0.514	1.6394	0 754	7 15	91 06	0 77	0.60
434L-1.2FeB	0.530	1.6447	0 756	6 88	88 15	0.90	0 51
434L-0.3NiB	0.786	2.4815	0 756	7 04	89 56	1 13	0 55
434L-0.6NiB	0.466	1.4695	0.754	7.07	90 03	1 36	0 57
434L-0.9NiB	0 470	1 4644	0 752	7 02	89 41	1 33	0 54
434L-1.2NiB	0 484	1.5025	0 754	6 96	88 66	1 51	0 51
434L-2Cu	0.446	1.4247	0 751	7 21	91.50	0 97	0 65
434L-2Cu- 0.3FeB	0 548	1 8186	0 754	7 43	94 29	0 94	0 73
434L-2Cu- 0 3NiB	0 568	1.8642	0 752	7 39	93 78	0 80	0 72
434L-2Cu- 0.3FeB-1YAG	0 683	2.3011	0 762	7 39	94 38	1 32	0 70
434L-2Cu- 0 3FeB-1YAG	0.527	1 7897	0.761	7 47	95 40	1 14	0.75

Appendix-III

Experimental data for green samples of 316L and with additives before sintering at 1250°C

Composition (wt%)	Height (cm)	Weight (gm)	Diameter (cm)	Density (g/cm ³)	Density (% Theoretical)
316L	0.588	1.9994	0.806	6.66	82.63
316L-0.3FeB	0.532	1.8394	0.806	6.78	84.12
316L-0.6FeB	0.510	1.7635	0.806	6.78	84.12
316L-0.9FeB	0.528	1.7394	0.806	6.46	80.25
316L-1.2FeB	0.520	1.7059	0.806	6.43	79.88
316L-0.3NiB	0.577	1.9908	0.806	6.76	83.87
316L-0.6NiB	0.520	1.7429	0.806	6.57	81.61
316L-0.9NiB	0.543	1.7976	0.806	6.49	80.62
316L-1.2NiB	0.649	2.1511	0.806	6.50	80.75
316L-2Cu	0.528	1.8116	0.806	6.72	83.17
316L-2Cu-0.3FeB	0.508	1.7471	0.806	6.74	83.52
316L-2Cu-0.3NiB	0.501	1.7359	0.806	6.79	84.14

Experimental data for the samples of 316L and with additives after sintering at 1250°C

Composition (wt%)	Height (cm)	Weight (gm)	Diameter (cm)	Density (g/cm ³)	Density (% Theoretical)	Weight Loss (%)	Densification Parameter
316L	0.581	1.9817	0.794	6.89	85.48	0.61	0.16
316L-0.3FeB	0.523	1.8287	0.793	7.08	87.84	0.58	0.23
316L-0.6FeB	0.503	1.7544	0.793	7.06	87.70	0.52	0.22
316L-0.9FeB	0.521	1.7019	0.791	6.65	82.60	0.55	0.12
316L-1.2FeB	0.511	1.6673	0.789	6.67	82.86	0.59	0.15
316L-0.3NiB	0.573	1.9792	0.793	6.99	86.72	0.58	0.18
316L-0.6NiB	0.510	1.7072	0.792	6.79	84.35	0.54	0.15
316L-0.9NiB	0.530	1.7801	0.789	6.87	85.34	0.55	0.24
316L-1.2NiB	0.636	2.1221	0.789	6.82	84.72	0.57	0.21
316L-2Cu	0.533	1.8066	0.801	6.83	84.53	0.58	0.08
316L-2Cu- 0.3FeB	0.500	1.7383	0.799	6.93	85.87	0.50	0.14
316L-2Cu- 0.3NiB	0.495	1.7263	0.798	6.97	86.37	0.55	0.14

Appendix-IV

Experimental data for green samples of 316L and with additives before sintering at 1400°C

Composition (wt%)	Height (cm)	Weight (gm)	Diameter (cm)	Density (g/cm ³)	Density (% Theoretical)
316L	0.768	2.5861	0.806	6.60	81.89
316L-0.3FeB	0.539	1.8136	0.806	6.59	81.76
316L-0.6FeB	0.631	2.1326	0.806	6.62	82.24
316L-0.9FeB	0.612	2.002	0.806	6.41	79.63
316L-1.2FeB	0.700	2.3029	0.806	6.45	80.12
316L-0.3NiB	0.465	1.5377	0.806	6.48	80.40
316L-0.6NiB	0.581	1.9296	0.806	6.51	80.87
316L-0.9NiB	0.626	2.0618	0.806	6.46	80.25
316L-1.2NiB	0.550	1.8304	0.806	6.52	80.99
316L-2Cu	0.786	2.613	0.806	6.52	80.69
316L-2Cu-0.3FeB	0.609	2.0284	0.806	6.53	80.92
316L-2Cu-0.3NiB	0.559	1.8966	0.806	6.65	82.40
316L-0.3FeB- 1YAG	0.587	1.9937	0.806	6.66	83.25
316L-0.3NiB- 1YAG	0.747	2.5158	0.806	6.60	82.5

Experimental data for the samples of 316L and with additives after sintering at 1400°C

Composition (wt%)	Height (cm)	Weight (gm)	Diameter (cm)	Density (g/cm ³)	Density (% Theoretical)	Weight. Loss (%)	Densification Parameter
316L	0.746	2.5637	0.782	0.716	88.83	0.87	0.38
316L-0.3FeB	0.512	1.7923	0.762	0.768	95.23	1.17	0.74
316L-0.6FeB	0.598	2.1083	0.764	0.769	95.53	1.14	0.75
316L-0.9FeB	0.590	1.9779	0.755	0.749	93.02	1.20	0.66
316L-1.2FeB	0.678	2.2724	0.781	0.749	93.00	1.32	0.65
316L-0.3NiB	0.441	1.5205	0.760	0.760	94.29	1.18	0.71
316L-0.6NiB	0.555	1.9105	0.765	0.749	93.04	0.99	0.64
316L-0.9NiB	0.598	2.0398	0.773	0.742	92.19	1.07	0.60
316L-1.2NiB	0.539	1.811	0.760	0.741	92.01	1.06	0.58
316L-2Cu	0.759	2.5866	0.781	0.711	88.00	1.01	0.38
316L-2Cu- 0.3FeB	0.586	2.0025	0.777	0.721	89.34	1.28	0.44
316L-2Cu- 0.3NiB	0.540	1.872	0.774	0.737	91.33	1.30	0.51
316L-0.3FeB- 1YAG	0.547	1.9730	0.770	7.74	96.75	1.04	0.81
316L-0.3NiB- 1YAG	0.704	2.4966	0.765	7.71	96.38	0.76	0.79

Appendix-V

Axial and radial dimensions of the 434L samples with additives sintered at 1250°C

Composition	Before Sintering		After Sintering		Axial	Radial
	Height (cm)	Diameter (cm)	Height (cm)	Diameter (cm)	Shrinkage %	Shrinkage %
434L	0.708	0.806	0.678	0.766	4.24	4.96
434L-0.3FeB	0.804	0.806	0.762	0.764	5.22	5.21
434L-0.6FeB	0.796	0.806	0.770	0.768	3.27	4.71
434L-0.9FeB	0.546	0.806	0.524	0.766	4.03	4.96
434L-1.2FeB	0.75	0.806	0.710	0.760	5.33	5.70
434L-0.3NiB	0.703	0.806	0.692	0.750	1.56	6.95
434L-0.6NiB	0.648	0.806	0.618	0.764	4.63	3.21
434L-0.9NiB	0.678	0.806	0.646	0.766	4.72	4.96
434L-1.2NiB	0.566	0.806	0.550	0.768	2.83	4.71
434L-2Cu	0.685	0.806	0.669	0.774	2.34	3.47
434L-2Cu-0.3FeB	0.537	0.806	0.526	0.772	2.05	4.22
434L-2Cu-0.3NiB	0.673	0.806	0.660	0.771	1.93	4.34

Appendix-VI

Axial and radial dimensions of the 434L samples with additives sintered at 1400°C

Composition	Before Sintering		After Sintering		Axial	Radial
	Height (cm)	Diameter (cm)	Height (cm)	Diameter (cm)	Shrinkage %	Shrinkage %
434L	0.858	0.806	0.804	0.746	6.29	7.44
434L-0.3FeB	0.956	0.806	0.900	0.752	5.86	6.70
434L-0.6FeB	0.558	0.806	0.526	0.750	5.73	6.95
434L-0.9FeB	0.548	0.806	0.514	0.754	6.20	6.45
434L-1.2FeB	0.560	0.806	0.530	0.756	5.36	6.20
434L-0.3NiB	0.834	0.806	0.786	0.756	5.76	6.20
434L-0.6NiB	0.496	0.806	0.466	0.754	6.05	6.45
434L-0.9NiB	0.492	0.806	0.470	0.752	4.47	6.70
434L-1.2NiB	0.506	0.806	0.484	0.754	4.35	6.45
434L-2Cu	0.471	0.806	0.446	0.751	5.31	6.82
434L-2Cu-0.3FeB	0.580	0.806	0.548	0.754	5.51	6.45
434L-2Cu-0.3NiB	0.602	0.806	0.568	0.752	5.65	6.70
434L-2Cu-0.3FeB- 1YAG	0.716	0.806	0.683	0.762	4.61	5.46
434L-2Cu-0.3NiB- 1YAG	0.553	0.806	0.527	0.761	4.70	5.58

Appendix-VII

Axial and radial dimensions of the 316L samples with additives sintered at 1250°C

Composition	Before Sintering		After Sintering		Axial	Radial
	Height (cm)	Diameter (cm)	Height (cm)	Diameter (cm)	Shrinkage %	Shrinkage %
316L	0.588	0.806	0.581	0.794	1.19	1.49
316L-0.3FeB	0.532	0.806	0.523	0.793	1.69	1.61
316L-0.6FeB	0.510	0.806	0.503	0.793	1.37	1.61
316L-0.9FeB	0.528	0.806	0.521	0.791	1.33	1.86
316L-1.2FeB	0.520	0.806	0.511	0.789	1.73	2.11
316L-0.3NiB	0.577	0.806	0.573	0.793	0.69	1.61
316L-0.6NiB	0.520	0.806	0.510	0.792	1.92	1.74
316L-0.9NiB	0.543	0.806	0.530	0.789	2.39	2.11
316L-1.2NiB	0.649	0.806	0.636	0.789	2.00	2.11
316L-2Cu	0.528	0.806	0.527	0.801	0.19	0.62
316L-2Cu-0.3FeB	0.508	0.806	0.500	0.799	1.57	0.87
316L-2Cu-0.3NiB	0.501	0.806	0.495	0.798	1.20	0.99

Appendix-VIII

Axial and radial dimensions of the 316L samples with additives sintered at 1400°C

Composition	Before Sintering		After Sintering		Axial	Radial
	Height (cm)	Diameter (cm)	Height (cm)	Diameter (cm)	Shrinkage %	Shrinkage %
316L	0.768	0.806	0.746	0.782	2.48	2.98
316L-0.3FeB	0.539	0.806	0.512	0.762	5.01	5.46
316L-0.6FeB	0.631	0.806	0.598	0.764	5.23	5.21
316L-0.9FeB	0.612	0.806	0.590	0.755	3.59	6.33
316L-1.2FeB	0.700	0.806	0.678	0.781	3.14	3.10
316L-0.3NiB	0.465	0.806	0.441	0.760	5.16	5.71
316L-0.6NiB	0.581	0.806	0.555	0.765	4.48	5.09
316L-0.9NiB	0.626	0.806	0.598	0.773	4.47	4.94
316L-1.2NiB	0.550	0.806	0.539	0.760	2.00	5.71
316L-2Cu	0.786	0.806	0.759	0.781	3.44	3.10
316L-2Cu-0.3FeB	0.609	0.806	0.586	0.777	3.78	3.60
316L-2Cu-0.3NiB	0.559	0.806	0.540	0.774	3.39	3.97
316L-0.3FeB-1YAG	0.587	0.806	0.547	0.770	6.81	4.47
316L-0.3NiB-1YAG	0.747	0.806	0.704	0.765	5.76	5.09

Appendix-IX

Bulk hardness (HV₂) values of the 434L samples with additives

Composition	Sintering Temperature			
	@1250°C		1400°C	
	Average Value	Standard Deviation	Average Value	Standard Deviation
434L	115.6	2.70	136.6	2.61
434L-0.3FeB	123.8	2.17	134.4	2.70
434L-0.6FeB	124.0	1.87	132.6	2.70
434L-0.9FeB	122.0	2.55	135.2	2.28
434L-1.2FeB	117.4	2.96	134.9	2.45
434L-0.3NiB	121.4	2.07	135.8	2.61
434L-0.6NiB	119.0	2.30	133.5	2.54
434L-0.9NiB	115.6	2.58	134.9	2.34
434L-1.2NiB	118.4	2.15	138.7	2.64
434L-2Cu	119.2	2.45	151.6	2.41
434L-2Cu-0.3FeB	124.0	2.36	165.2	2.17
434L-2Cu-0.3NiB	125.0	2.45	163.6	2.70
434L-2Cu-0.3FeB- 1YAG	-	-	217	2.70
434L-2Cu-0.3NiB- 1YAG	-	-	220	2.85

Appendix-X

Bulk hardness (HV₂) values of the 316L samples with additives

Composition	Sintering Temperature			
	@1250°C		@1400°C	
	Average Value HV ₂	Standard Deviation	Average Value HV ₂	Standard Deviation
316L	121.8	2.25	155.5	2.45
316L-0.3FeB	126.9	2.45	189.2	2.34
316L-0.6FeB	125.6	2.21	190.7	2.23
316L-0.9FeB	122.6	2.34	185.1	2.70
316L-1.2FeB	124.2	2.48	187.6	2.65
316L-0.3NiB	127.6	2.38	191.3	2.64
316L-0.6NiB	126.3	2.44	192.8	2.55
316L-0.9NiB	122.2	2.37	184.5	2.18
316L-1.2NiB	126.3	2.24	183.4	2.35
316L-2Cu	122.6	2.31	165.3	2.75
316L-2Cu-0.3FeB	123.5	2.70	164.9	2.65
316L-2Cu-0.3NiB	124.7	2.65	163.9	2.35
316L-0.3FeB-1YAG	-	-	232	2.77
316L-0.3NiB-1YAG	-	-	238	2.82

Appendix-XI

Microhardness ($HV_{0.005}$) values of the 434L and 316L samples with additives

Composition	Sintering Temperature			
	@1250°C		@1400°C	
	Average Value HV ₂	Standard Deviation	Average Value HV ₂	Standard Deviation
434L	84.5	2.45	105.5	2.75
434L-2Cu	75.5	2.65	100.2	2.54
434L-2Cu-0.3FeB	87.3	2.51	147.8	2.43
434L-2Cu-0.3NiB	89.8	2.64	155.8	2.70
434L-2Cu-0.3FeB- 1YAG	-	-	190.5	2.80
434L-2Cu-0.3NiB- 1YAG	-	-	195.6	2.91
316L	85.2	2.68	120.6	2.85
316L-0.3FeB	91.8	2.58	160.3	2.84
316L-0.3NiB	93.3	2.64	165.8	2.75
316L-0.3FeB-1YAG	-	-	215.3	2.93
316L-0.3NiB-1YAG	-	-	221.2	2.97

A 145000



A145000
